THE UNIVERSITY *of* EDINBURGH

High-Pressure Studies of Energetic Co-Crystals

A thesis for the degree of Doctor of Philosophy in Chemistry

Karl Stewart Hope

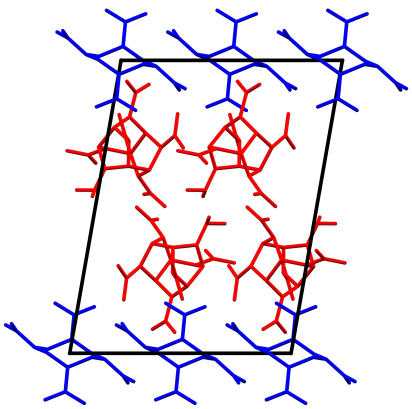

School of Chemistry

The University of Edinburgh

2015-2019

Abstract

Co-crystals have been widely explored in the field of energetic materials for more than a decade. Their ability to tune the physical, chemical and energetic properties of a material without the need to synthesise new molecules from scratch; along with their ability to count as new intellectual property; has made them attractive candidates for both civil and military applications.

However, until now, no-one in published literature has explored the behaviour of these materials under high-pressure conditions – the very conditions that are generated during an initiation event. This thesis tackles that question of how the structures of these novel materials change with increasing pressure. Specifically, this work focuses on co-crystal systems of two energetic materials – hexaaza-hexanitro-isowurtzitane (CL-20) and nitroguanidine (NQ) – with an array of co-formers, both energetic and non-energetic. All systems have been studied using Paris-Edinburgh pressure cells and neutron powder diffraction at the ISIS Neutron Source in Harwell, Oxfordshire. Each co-crystal has had a Birch-Murnaghan equation of state fitted to its structural data over the respective pressure range.

The CL-20 systems used 1,3,5,7-tetranitro-1,3,5,7-tetrazocine (HMX), trinitrotoluene (TNT), and hydrogen peroxide (HP) as co-formers. 2(CL-20):HMX was studied up to 3.5 GPa, and found to compress in an unusually isotropic manner, with no phase separations or polymorphic transitions occurring over this pressure range. The bulk modulus (B_0) was determined to be 14.1(8) GPa, with pressure derivative $B' = 9.1(9)$. 2(CL-20):HP was studied up to 5.7 GPa, and also found to compress isotropically with no chemical changes or unusual structural behaviour over that pressure range. B_0 and B' were 13.4(2) GPa and 11.2(3) respectively. In CL-20:TNT, the system was studied up to 3.5 GPa, initially with a similar lack of unusual behaviour. However, an initiation event is believed to have occurred after reaching the next pressure point (4.1 GPa). B_0 and B' up to 3.5 GPa are 10.1(5) GPa, and 11.6(7).

The NQ systems used two nitropyridone molecules as co-formers – 2-hydroxy-3,5-dinitropyridone (DNP), and 2-hydroxy-5-nitropyridone (NP). NQ:DNP underwent a phase transition at 0.86 GPa (B_0 and B' of the ambient-pressure phase being 14.4(2) GPa and 4.0), whereas the NQ:NP system showed no phase transitions or separations up to 3.5 GPa, in contrast to earlier X-ray diffraction data of the same material. B_0 for NQ:NP was 8.7(9) GPa, with $B' = 9.7(9)$.

A mechanochemical process used to prepare some of the aforementioned materials, Resonant Acoustic Mixing (RAM), was also studied *in situ* using neutron powder diffraction – the first time this RAM process has ever been monitored using neutron-based methods. Two non-energetic systems, urea:oxalic acid and glycine:oxalic acid, were used in this proof-of-concept study and their co-crystallisation processes were successfully followed by neutron diffraction over a time range of one hour in collection blocks of five minutes. This proves neutron diffraction can be used to successfully follow mechanochemical reactions *in situ* over shorter timescales than initially thought possible using this technique.

Lay Summary

Explosives, propellants and pyrotechnics (energetic materials) have been used in a variety of human industries for many years. However, a key problem with these materials is their sensitivity - how easily they are set off or initiated by either a physical action, mishandling, or the environment around them. In several cases, although the materials may have good levels of power for their intended purpose, their sensitivity makes them unsuitable to handle, and unpleasant to work with.

However, this is not a problem which is easily overcome. Making inherently insensitive materials from scratch is not an easy process, requiring years of synthesis attempts and trial and error. Not helping this is the fact that it is not currently easy to predict a material's sensitivity simply from looking at its chemical structure. Co-crystallisation is one method that has been investigated for mitigating these sensitivity issues, using existing and known energetic materials. It can be thought of as 'mixing' materials on the molecular level, giving a new co-crystal material which blends the properties of its components (or co-formers).

The chemical behaviour of these co-crystals in an initiation environment (i.e. in the process of being set off or ignited) has never been investigated before. Putting the material under high-pressure conditions (usually up to several thousand times normal atmospheric pressure) is one technique that has been used with other energetic materials in the past as a way of seeing how they might behave and how their structures might change 'in action'. Some materials can also change into new forms, or polymorphs, under these conditions. Such new forms might have different properties to the normal state of the material, and if the new form can still persist at ambient pressure, this is also of interest.

As these techniques have never been performed with co-crystal explosives or propellants, the work contained in this thesis aims to explore this new area.

Own work declaration

I hereby declare that all material contained within this thesis is the product of my own work and composition, except where indicated or acknowledged in the text; and that this work has not been submitted for any other degree or qualification, except as specified.

Signed:

Date: 26/03/2020

Contents

Chapter 1

Introduction to background concepts

1.1 General aims

High-pressure conditions can have a variety of effects on materials and crystal structures. This work explores how energetic co-crystals - multi-component materials composed of explosives, propellants or pyrotechnics - respond to changes in pressure conditions. Specifically, whether any polymorphic transitions, phase separations, or other reactive behaviour, occur in this environment.

This chapter gives an introduction to the world of energetic materials, co-crystals, and high-pressure conditions. Chapter 2 then details the concepts behind experimental and analytical techniques used in this research. Chapter 3 focuses on co-crystals of a powerful but volatile explosive, hexaaza-hexanitro-isowurtzitane (CL-20). Chapter 4 deals with co-crystals of a relatively-insensitive propellant, nitroguanidine (NQ). Chapter 5 launches into a further exploration of Resonant Acoustic Mixing (RAM) technology, used in the preparation of compounds for Chapters 3 and 4. General conclusions and avenues for future research then follow in Chapter 6.

1.2 Energetic materials

Overview of energetic materials

"Energetic material" is a term used to refer to a material designed to release a large amount of stored chemical energy in a short space of time for some intended use [1]. These materials are usually subdivided by their intended use and the rate at which they release their energy, rather than by any distinct chemical template. The main classifications are explosives, propellants and pyrotechnics. These subdivisions encompass a wide variety of material types and compositions.

Pyrotechnics are materials designed to release significant amounts of heat, light and/or sound primarily for visual or audio effect [2]. Unsurprisingly, fireworks feature strongly in this category (Figure 1.1). Pyrotechnics are also employed heavily in the media industry for the generation of special effects.

Figure 1.1: Example of a pyrotechnic display - fireworks above Edinburgh castle. Picture by Steve Collis, reproduced under the Creative Commons Attribution 2.0 Generic licence [3].

Pyrotechnics are primarily composition-based, relying on a physical mixture of fuel, oxidiser and effects materials. For example, copper salts are used to produce blue-coloured displays. For more general effects, materials include flash powders composed of aluminium or magnesium, designed to produce simulated explosions in film or for military training purposes [4].

Propellants are designed to combust or deflagrate to produce a large amount of gas (i.e. thrust) very quickly [5]. They have obvious applications in the rocketry and aerospace industries, but also have uses in weaponry, and even in car airbags where large volumes of gas must be generated very rapidly.

A variety of chemical classes are employed in propellants - the types used tend to depend on the amount of thrust (or general application) required.

Large rocketry and aerospace applications rely on distinct fuel/oxidiser mixes, the most well-known being the combination of liquid oxygen and liquid hydrogen, used to power the Saturn V rockets that launched the Apollo space missions (Figure 1.2).

Figure 1.2: A large-scale example of propellants in action - the launching of the Saturn V rocket carrying the Apollo 11 lunar and command modules [6].

Smaller applications such as car airbags (Figure 1.3) - where the need to conserve space or preserve safety outweighs the need for large amounts of heat and thrust - use less volatile mixtures, or even single-component propellants that combine the fuel and the oxidiser in one material. Recently these propellants have become increasingly organic in nature, employing materials such as nitrocellulose or nitroguanidine rather than inorganic azides.

Figure 1.3: A small-scale example of propellants or gas generators in action - the activation of a car airbag in an accident [6].

Explosives are designed to release such a large amount of energy in such a short space of time that they produce a supersonic shockwave. This occurs upon the application of some stimulus, such as an electrical impulse, heat, or an intentional shock or impact [7]. They are further classified based on their sensitivity to these stimuli, into primary and secondary explosives.

Primary explosives are the most sensitive of these materials. They tend to have the greatest overall detonation performance, but at the expense of very high sensitivity. Primary explosives have been historically defined as any explosive displaying a greater sensitivity to impact than pentaerythritol tetranitrate (PETN, Figure 1.4) [1]. More systematically, modern tests such as the BAM fallhammer test (Figure 1.5) define a primary explosive as any material that requires less than 5 J of impact energy to initiate [8, 9].

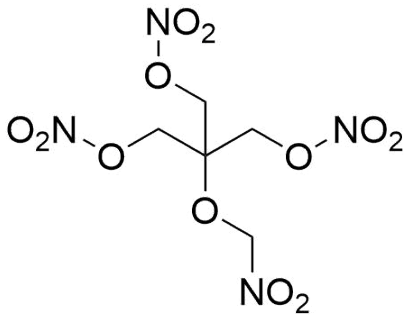

Figure 1.4: The structure of pentaerythritol tetranitrate (PETN).

Figure 1.5: A BAM fall-hammer standardised testing apparatus, used to determine the impact sensitivities of energetic materials. Image source: http://www.ozm.cz

These materials tend to be inorganic salts with extremely reactive ligands. Two common examples are lead azide and mercury fulminate - $Pb(N_3)_2$ and $Hg(CNO)_2$.

Secondary explosives are the more insensitive category of explosives. They tend to possess lower detonation performance than their primary counterparts, but with the benefit of greatly-reduced sensitivity to stimuli. In fact, their sensitivity to stimuli is often so reduced that the most reliable way to initiate them is by detonating a small amount of primary explosive in close proximity, i.e. using the explosive shockwave of the primary explosive as a stimulus. Secondary explosives are mainly molecular organic species with nitro groups. These are designed to release chemical energy through the thermodynamically-favourable formation of N_2 and CO_2 during decomposition.

A good example of a secondary explosive is hexahydro-1,3,5-trinitro-1,3,5-triazinane, better known as RDX or Hexogen (Figure 1.6). This explosive was first synthesised at the start of the 1900s, *via* the nitration of hexamine. As the 20th century progressed, RDX became one of the most commonly-employed explosives,

seeing action throughout the Second World War on both sides of the conflict [1].

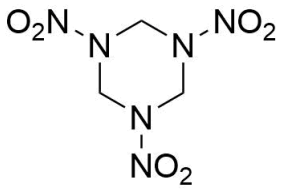

Figure 1.6: The structure of RDX - $C_3H_6N_6O_6$.

As can be seen from the structure, RDX contains a high nitrogen content and an oxygen balance of $\sim$ -22 %. These factors contribute to its explosive properties.

Oxygen balance is a measure of how much oxygen in the structure is converted to byproducts associated with complete combustion (CO_2, water, and metal oxides), calculated through the formula shown in Equation 1.

$$OB_{\%} = \frac{-1600}{M_R} * (2N_C + \frac{N_H}{2} + N_M - N_O) \tag{1}$$

The equation for oxygen balance. Where $OB_{\%}$ = oxygen balance in percent, M_R = molecular weight (g/mol), N_C = the number of carbon atoms, N_H = the number of hydrogen atoms, N_M = the number of metal atoms, and N_H = the number of hydrogen atoms.

Generally secondary explosives with oxygen balances closer to 0 are sought. Negative oxygen balances result in the production byproducts of incomplete combustion, such as CO.[1]

However, oxygen balance alone is not a reliable measure of energetic performance.[1] The performance of secondary explosives is also routinely tuned by combining different materials together in compositions and mixtures; and by controlling physical properties such as packing, particle size, and binding [10]. Despite its negative oxygen balance, tuning of these other factors has allowed RDX to form the core of many compositions and mixtures throughout the 20th century. It still remains a key explosive component into the present day.

Issues with energetic materials

Unfortunately energetic materials are not perfect. There are some issues which hinder or hamper their use in various applications. Some materials are rather toxic to handle; or produce toxic byproducts either through decomposition or through their detonation. For example, picric acid produces harmful vapours and reacts with copper to give copper picrates [11]; mercury salts pose a large environmental hazard [12]; and trinitrotoluene (TNT) can leach into groundwater systems and contaminate water supplies [13]. Even the aforementioned RDX is not ideal, as extended exposure, inhalation or ingestion can result in organ damage

Figure 1.7: An example of a polymer-bound explosive - Composition 4, or C-4 - widely used by modern militaries. Image by Magnus Manske, reproduced under the Creative Commons Attribute Share-Alike 3.0 Licence [18].

and neurological problems [14].

More commonly, however, the biggest issue with many explosives is sensitivity. Even many secondary explosives can be more sensitive than desirable, especially to accidental initiation. Energetic materials can be vulnerable to an accidental heavy impact (for example, being dropped from a height); or a chain reaction in a 'sympathetic detonation' if nearby material initiates. They can also chemically react, initiate, or otherwise decompose under abnormal temperature conditions.

Various attempts have been made throughout the 20th and 21st centuries to mitigate the issue of sensitivity in energetic materials without compromising on energetic performance. An obvious solution is to synthesise new energetic materials from scratch that have inherently reduced sensitivity. However, the mechanisms behind sensitivity in materials are not yet fully understood, and it is difficult to predict which molecular structures will possess this intrinsic insensitivity. Moreover, there are substantial difficulties in devising new synthetic routes to a novel chemical species, as well as scaling these routes up to industrially-appropriate levels [15]. Hence, other solutions have been pursued that make use of existing materials. Perhaps the most common technique is to reduce the sensitivity by compositing or mixing sensitive explosives with a less sensitive material, or even a non-energetic component [10].

This can be taken even further with the concept of *polymer-bonded explosives*, or PBXs. In these materials, the explosive is encased in a polymer matrix to physically 'spread out' its grains and therefore reduce its sensitivity by preventing friction between particles and reducing the attenuation of any shock. The polymer matrix also gives other added advantages in terms of easy portability and moldability [16]. PBXs have gained significant media attention through their use in various movies and television shows, with Composition-4 (better known as C4, Figure 1.7) becoming a particularly well-known example. This PBX is composed of $\sim$ 90 % RDX, with the remaining percentage being made up of a plasticiser, binder and oil [17].

Another more recent potential solution to the issue of sensitivity in energetic materials is *co-crystallisation*. This extends the concept of compositions to the molecular level, by crystallising materials together to produce a new substance with altered physical and chemical properties. The next section will discuss this

concept in more detail.

1.3 Co-crystallisation

A **co-crystal** is a crystalline material formed by combining two or more neutral, non-volatile, components together using intermolecular forces such as hydrogen bonding or π-stacking. These are usually considered distinct entities from salts, solvates and hydrates [19].

The technique of co-crystallisation was first investigated for its potential applications in the pharmaceutical industry. Here, co-crystallisation was studied for its potential to adjust the physical, chemical and pharmacological properties of active pharmaceutical ingredients (APIs), without having to synthesise completely new molecules [20]. The ultimate aim was to alter drug properties such as solubility, bioavailability, and blood-brain barrier permeability. Co-crystals also have the added advantage of using known materials, with known side effects and known pharmaco-dynamics, while still counting as new intellectual property [19].

Over the past decade this same principle has been investigated by the energetics field, and co-crystals of a number of energetic materials are now known. Co-crystals of CL-20 have been produced by Bolton [21, 22] - the high-pressure behaviour of these will be discussed later in this thesis. Further co-crystals and solvates of CL-20 have been prepared by Millar [16]. Other energetic compounds have also been explored for their co-crystallisation properties - a series of co-crystals of TNT, and of HMX, have been investigated by Landenberger [23, 24].

The logic in pursuing this field is that co-crystallisation can not only alter the physical and chemical properties of energetic materials in the same manner as APIs, but that the process can tune energetic properties too. Applied successfully this could result in a material with not only a different detonation performance, but also a modified sensitivity to stimuli.

The most routine method of forming a co-crystal is through evaporative crystallisation. The compounds are dissolved in a compatible solvent; and the co-crystal is allowed to precipitate out. This can be aided by choosing solvents where the two components are only soluble at increased temperature; thereby driving the formation of a precipitate when the solution is cooled [25]. This is shown diagrammatically in Figure 1.8.

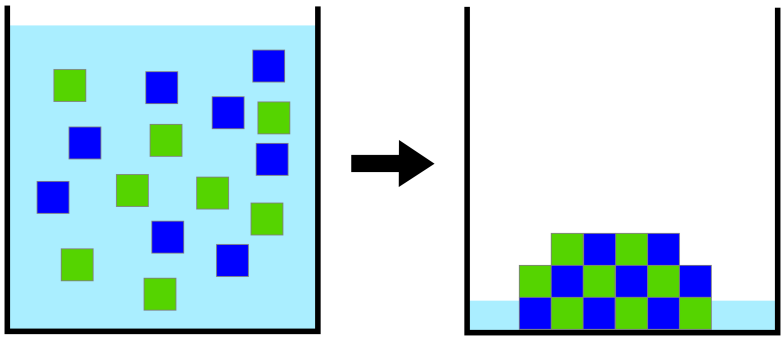

Figure 1.8: Diagrammatic representation of co-crystallisation. A solution of two different molecular species (left) is evaporated to produce an ordered co-crystal of the two materials (right).

Another method of forming co-crystals is to melt the two components together [26]. However, owing to the high temperatures required for this process and the proclivity of many energetic materials to decompose rather than melt upon heating, this technique is not routinely employed for energetic co-crystals.

One way to alter energetic properties through co-crystallisation is to co-crystallise a sensitive energetic material with a less-sensitive material. This aims to reduce the sensitivity of the first material without necessarily compromising its detonation performance.

However, research has also gone in the other direction - co-crystallising two comparably sensitive energetic materials in the hope that the increased intermolecular interactions provide increased stability, while detonation performance is overall enhanced. This is considered a "holy grail" of energetics research - a material with both low sensitivity and high performance.

1.4 High-pressure studies

Various studies have been published to date covering the effects of pressure on various energetic materials. For example, RDX [27], CL-20 [28], and dinitroanisole (DNAN) [29], have been shown to undergo changes in crystal structure (polymorphism) when subjected to extremes of temperature and/or pressure. For example, the temperature- and pressure-induced polymorphism of RDX is exemplified by its phase diagram in Figure 1.9 below.

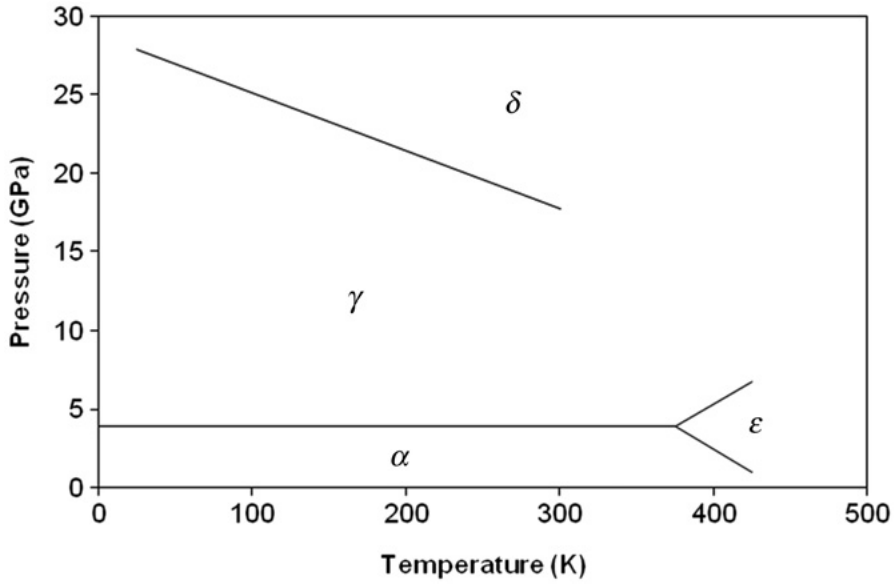

Figure 1.9: The phase diagram of RDX, showing the regions of stability of four polymorphs as a function of temperature and pressure. Image sourced from [30].

There are two main motivations behind the study of energetic materials under pressure. The first is scientific in nature. Every explosive possesses a value known as a "detonation pressure". This is the pressure induced by the shockwave produced during detonation of this material, and commonly extends into the gigapascal (GPa) range. The detonation pressure of TNT, for instance, is 25.9 GPa [31]. Coupled with this is a value known as "detonation velocity" - the speed at which the shockwave travels through an explosive material. As mentioned previously, explosives are characterised by their supersonic shockwaves - therefore have detonation velocities greater than the speed of sound. A shock front moving at these speeds can naturally result in a high detonation pressure being generated.

Research into the effects of extreme pressure has shown that pressures on this scale can have extraordinary effects on materials. For example, polymorphic transitions; phase separations of components; or chemical reactions [32]. All of these factors have the potential to impact upon the performance of an energetic material during detonation. Observation of the behaviour of an energetic material under static pressure provides some insight into shock-induced behaviour and whether any of these processes could occur during or immediately prior to detonation.

The second reason is practical in nature. If new polymorphs can be produced under extremes of pressure, it is possible that these polymorphs may be recoverable back to ambient conditions, and display an increased density relative to their original polymorph. The performance of an energetic material tends to be intrinsically linked to its density, therefore the production of new potentially-higher-density polymorphs (with improved detonation properties) is of interest to the energetics industry. The recoverable high-pressure

epsilon polymorph of RDX is a significant example here [30].

Importantly, no studies have been published of energetic co-crystals under such conditions, hence the main focus of this thesis is on studying such materials under extremes of pressure.

1.5 References

[1] J. Akhavan, *The Chemistry of Explosives*, 3rd edn., RSC Publishing, UK, 2011.

[2] H. Ellern, *Military and Civilian Pyrotechnics*, Chemical Publishing Company Inc., USA, 1968.

[3] https://creativecommons.org/licenses/by/2.0/.

[4] U. Krone and H. Treumann, *Propellants, Explosives & Pyrotechnics*, 1990, **15(3)**, 115–120.

[5] T. Yoshida, Y. Wada and N. Foster, *Safety of Reactive Chemicals and Pyrotechnics*, Elsevier Publishing, 1995.

[6] Public domain image.

[7] J. P. Agrawal, *High Energy Materials*, Wiley Publishing, 2010.

[8] T. Keicher, S. Lobbecke, S. Brase and K. Banert, *Lab-scale synthesis of azido compounds: safety measures and analysis*, Wiley Publishing, 2010.

[9] *Discussions and training with OZM Research (BAM Fall-hammer manufacturers)*, 2015.

[10] A. Sikder and N. Sikder, *Journal of Hazardous Materials*, 2004, **112(1–2)**, 1 – 15.

[11] J. F. Wyman, M. P. Serve, D. W. Hobson, L. H. Lee and D. E. Uddin, *Journal of Toxicology and Environmental Health*, 1992, **37**, 313–327.

[12] A. Renzoni, F. Zino and E. Franchi, *Environmental Research*, 1998, **77**, 68–72.

[13] D. Kalderis, S. B. Hawthorne, A. A. Clifford and E. Gidarakos, *Journal of Hazardous Materials*, 2008, **159**, 329–334.

[14] A. S. Kaplan, C. F. Berghout and A. Peczenik, *Archives of Environmental Health*, 1965, **10(5)**, 877–883.

[15] P. F. Pagoria, G. S. Lee, A. R. Mitchell and R. D. Schmidt, *Thermochimica Acta*, 2002, **384(1–2)**, 187 – 204.

[16] D. I. Millar, H. E. Maynard-Casely, D. R. Allan, A. S. Cumming, A. J. Mackay, I. D. Oswald, C. C. Tang and C. R. Pulham, *CrystEngComm*, 2010, **14**, 3742–3749.

[17] B. E. Homan, M. M. Biss and K. L. McNesby, *US Army Research Lab Technical Report*, 2013, **ADA592061**.

[18] https://creativecommons.org/licenses/by-sa/3.0/.

[19] A. D. Bond, *CrystEngComm*, 2007, **9(9)**, 833–834.

[20] P. Vishweshwar, J. A. McMahon, J. A. Bis and M. J. Zaworotko, *Journal of Pharmaceutical Sciences*, 2006, **95(3)**, 499–516.

[21] O. Bolton, L. R. Simke, P. F. Pagoria and A. J. Matzger, *Crystal Growth & Design*, 2012, **12(9)**, 4311–4314.

[22] O. Bolton and A. J. Matzger, *Angewandte Chemie International Edition*, 2011, **50(38)**, 8960–8963.

[23] K. B. Landenberger and A. J. Matzger, *Crystal Growth & Design*, 2010, **10(12)**, 5341–5347.

[24] K. B. Landenberger and A. J. Matzger, *Crystal Growth & Design*, 2012, **12(7)**, 3603–3609.

[25] S. J. Nehm, B. Rodriguez-Spong and N. Rodriguez-Hornedo, *Crystal Growth & Design*, 2006, **6(2)**, 592–600.

[26] N. Blagden, D. J. Berry, A. Parkin, H. Javed, A. Ibrahim, P. T. Gavan, L. L. De Matos and C. C. Seaton, *New Journal of Chemistry*, 2008, **32(10)**, 1659–1672.

[27] A. J. Davidson, I. D. Oswald, D. J. Francis, A. R. Lennie, W. G. Marshall, D. I. Millar, C. R. Pulham, J. E. Warren and A. S. Cumming, *CrystEngComm*, 2008, **10(2)**, 162–165.

[28] D. I. Millar, H. E. Maynard-Casely, A. K. Kleppe, W. G. Marshall, C. R. Pulham and A. S. Cumming, *CrystEngComm*, 2010, **12(9)**, 2524–2527.

[29] D. W. Ward, P. L. Coster, K. S. Hope and C. R. Pulham, *Proceedings of the 18th NTREM Seminar*, 2015, 230–235.

[30] D. I. Millar, W. G. Marshall, I. D. Oswald and C. R. Pulham, *Crystallography Reviews*, 2010, **16**, 115–132.

[31] R. L. Jameson and A. Hawkins, 1966.

[32] F. P. Fabbiani and C. R. Pulham, *Chemistry Society Reviews*, 2006, **35**, 932–942.

Chapter 2

Introduction to techniques used

2.1 Principles of diffraction

The structural analysis carried out in this thesis primarily uses the technique of neutron powder diffraction. This field evolved from the techniques of X-ray diffraction, so to best understand the principles involved, it is necessary to consider the principles of X-ray crystallography.

X-ray crystallography

X-ray crystallography first began as a discipline in the early 20th century, when Max von Laue, Walter Friedrich and Paul Knipping experimentally proved that a diffraction pattern of spots resulted from firing a beam of X-rays at a crystal. While attempting to derive an accurate set of equations to explain how crystal lattices can scatter waves like this, von Laue had difficulty relating these experimentally-observed spots to the actual atomic structure of the crystal. This was due to some incorrect assumptions with regard to how the individual atoms scatter X-rays in a crystal structure [1].

The breakthrough in this respect came with William Lawrence Bragg in 1913. Bragg made the hypothesis that X-ray diffraction occurred not from all distinct individual atoms, but rather from planes of atoms in the crystal. Moreover, Bragg claimed that spots from this diffraction would only be visible at points where the relations between beam angle, incident wavelength, and inter-planar spacing were such that the diffracted waves would experience constructive interference (as seen in Figure 2.1).

This led to the development of what is now known as **Bragg's Law** (Equation 2) - underpinning the science of crystallography as we know it today [1, 2].

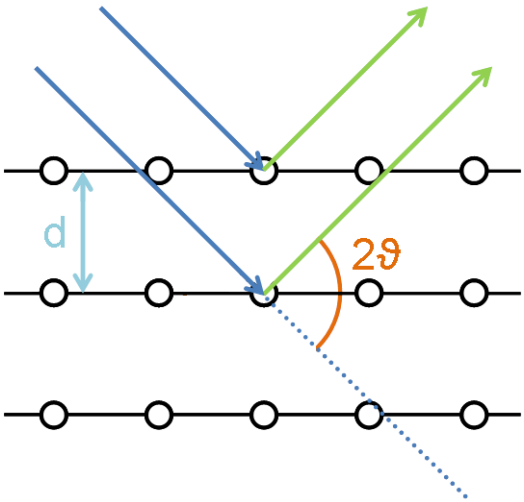

Figure 2.1: Diagrammatic representation of Bragg's Law, showing diffraction of incident X-rays from two planes within a crystal.

$$n\lambda = 2d_{hkl}\sin\theta \tag{2}$$

Bragg's Law. Where n = the order of reflection, λ = the wavelength, d_{hkl} = the spacing between lattice planes (d-spacing), and θ = the scattering angle.

Differences between X-ray and neutron diffraction

While there are many common aspects between X-ray and neutron crystallography, there are differences when it comes to the scattering of the two by crystals, such that neutrons bring their own distinct nuances to the field.

For the purposes of this document, only the *elastic scattering* of neutrons, where there is no exchange of energy between the neutron and the sample, will be discussed. This is the form of scattering which is desired in a crystallographic diffraction experiment. *Inelastic scattering*, where there *is* such an energy exchange (to or from the neutron), is used in different varieties of neutron experiment beyond crystallography, such as spectroscopic experiments that observe phonons or magnons.

Unlike X-rays, which scatter from the electron clouds of atoms, neutrons scatter directly from the atomic nuclei. This gives neutrons a different level of penetrability compared to X-rays, and therefore a different level of 'sensitivity' - different scattering lengths - with regard to certain elements.

This situation is compounded further with isotopes that possess non-zero nuclear spins. In those situations, each spin state of the isotope will *also* have its own scattering length. This means that unlike X-rays, where scattering strength increases proportionally with atomic number; there is no such clear correlation with how well a neutron scatters from an element. This can be seen in the plot of scattering lengths in Figure 2.2.

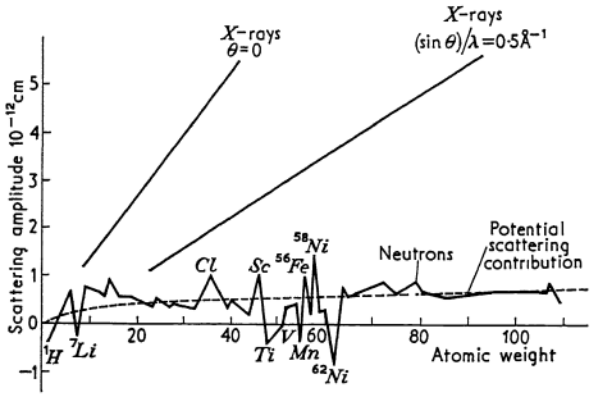

Figure 2.2: A plot of the coherent scattering lengths for each element. Figure reproduced from [3].

Furthermore, with neutrons the question of coherent and incoherent scattering comes into play. *Coherent scattering* results in interference effects (constructive or destructive), which if constructive lead to the observance of Bragg peaks and thus diffraction data. *Incoherent scattering* does not result in interference effects. This incoherent component therefore does not give useful diffraction data, and instead merely adds to the background noise in a diffraction experiment (Figure 2.3).

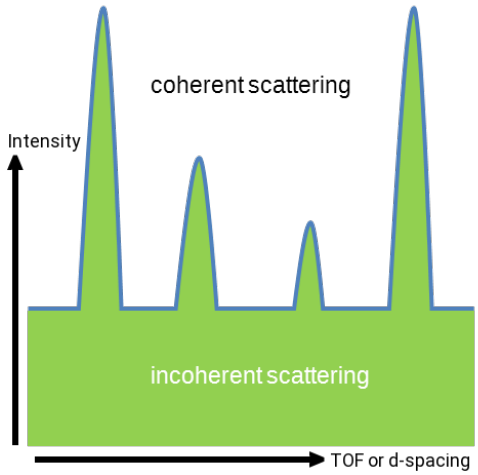

Figure 2.3: Diagrammatic representation of how coherent and incoherent scattering each contribute to a neutron powder diffraction pattern.

Each isotope or spin state has a distinct value (called a cross-section) for how well they scatter both coherently and incoherently, and this can affect neutron experiments accordingly. If the incoherent scattering cross-section is greater in magnitude than its coherent counterpart, that isotope or spin state will mostly diffract incoherently, and therefore will result in a greater degree of background noise than analysable diffraction data.

This point is extremely relevant when a sample contains hydrogen, specifically the ^{1}H isotope. ^{1}H has a very low coherent scattering cross-section, and an extraordinarily high incoherent scattering cross-section.

This means samples with large atom-percentages of hydrogen will have a massive incoherent scattering component, and their powder diffraction patterns will contain significant amounts of background scattering intensity. ^{2}H - deuterium - on the other hand, is the opposite case. It has a coherent cross-section far greater than its incoherent counterpart. For this reason, hydrogen-containing samples are generally deuterated prior to neutron powder diffraction experiments [4, 5].

Neutron diffraction from spallation sources

Generally there are two sources of neutrons for research purposes, and therefore two categories of facility at which neutron diffraction experiments can be performed.

A *nuclear reactor*, such as at the Institut Laue-Langevin (ILL) in Grenoble, will output neutrons continuously across a wide spectrum of wavelengths. These are then filtered such that neutrons of a specific wavelength encounter the sample of interest and are diffracted accordingly. In many ways, a neutron experiment performed at a reactor source is similar to a laboratory X-ray diffraction experiment, in that data is collected as a function of scattering angle (2θ).

The other type of neutron facility is a *spallation source* such as the ISIS Neutron Source in Oxfordshire, which produces neutrons in pulses. As the neutron work in this thesis has been produced using the PEARL instrument at the ISIS facility, this section will focus on the spallation method.

At ISIS, neutrons are produced using a combination of particle accelerators and a synchrotron, shown in Figure 2.4. Firstly, a linear accelerator uses electromagnetic forces to accelerate bursts of hydride (H^-) ions to 70 MeV. These pass through an injector and into a synchrotron, being converted to protons (H^+) by a stripper foil in the process.

Within ten milliseconds, the protons entering this synchrotron are accelerated to 800 MeV in two pulses. Once the required momentum is reached, the protons are "kicked" out of the synchrotron *via* kicker magnets into a proton beamline. They are guided along this beamline until they strike a tantalum target (the "target station"). This produces a burst of "fast" (high-energy) neutrons, which then pass through a series of moderators to leave "slower" (lower-energy) thermal neutrons appropriate for experimental purposes. These reach the facility's instruments along evacuated guide tubes.[1]

[1] As derived from a combination of the online documentation of the ISIS Neutron Source - http://www.isis.stfc.ac.uk/about/how-isis-works—in-depth4371.html - and reference [4].

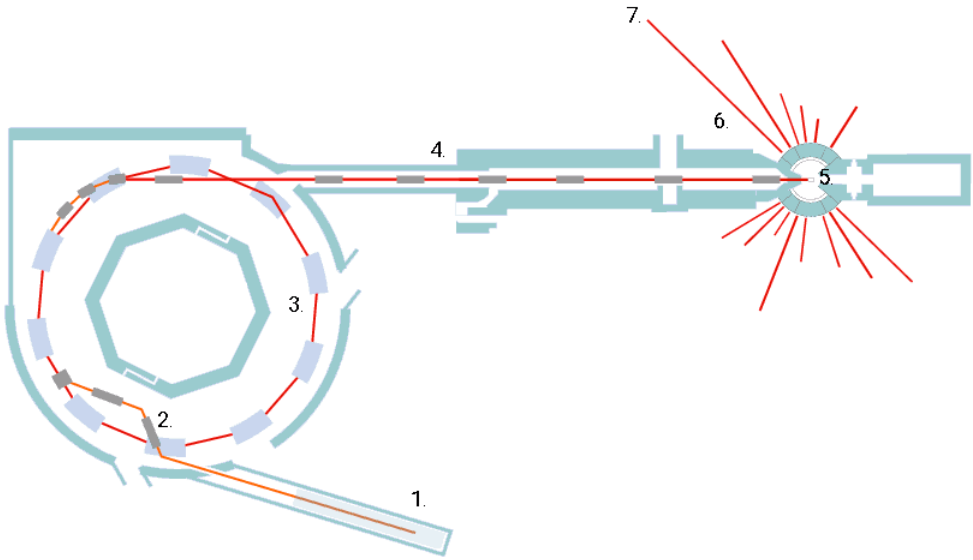

Figure 2.4: Diagrammatic representation of Target Station 1 at the ISIS Neutron Source, with features indicated as follows

1. Linear accelerator	5. Target station
2. Injector	6. Neutron beamline
3. Proton synchrotron	7. Neutron instrument
4. Proton beamline	

Diagram adapted from: http://pd.chem.ucl.ac.uk/pdnn/inst3/ral.gif

Diffraction experiments performed at a spallation source, such as those on the PEARL diffractometer at ISIS, which form the bulk of this thesis, proceed *via* measuring the "time-of-flight" (TOF) of neutrons.

Whereas most lab-based X-ray diffraction experiments vary the 2θ angle, measure the diffracted intensity, and hold the wavelength constant, time-of-flight neutron experiments operate in a different manner. The nature of the spallation process means a wide variety of neutron wavelengths are produced, and instead the 2θ angle is held constant. The de Broglie relation (Equation 3) allows these wavelengths to be determined if we know the time the neutrons take to reach the detector. Generally a range of detectors at various 2θ angles are used to build up a full diffraction pattern [4, 6].

$$\frac{h}{\lambda} = m_n v = m_n \left(\frac{L}{t}\right) \tag{3}$$

The de Broglie relation, where h is the Planck Constant, λ is the wavelength, m_n is the mass of a neutron, v is velocity of the neutrons, L is the total flight path distance from the neutron source to the detector, and t is the time-of-flight from neutron source to detector.

2.2 High-pressure conditions

The equipment of choice for high-pressure X-ray diffraction experiments is the diamond-anvil cell (DAC), where pressure is applied via a system of screws to two diamonds, to squeeze a sample loaded between them. However, DACs are designed to operate with micrograms of material, making them unsuitable for neutron diffraction experiments where hundreds of milligrams of sample are generally needed to obtain clear and useful diffraction data.

To bring a comparable level of high-pressure capability ot the field of neutron crystallography, a collaboration between the universities of Edinburgh and Paris resulted in the development of the Paris-Edinburgh (P-E) press, as seen in Figure 2.5 [7]. Numerous evolutions to the technology have taken place over the years [8][9], and the current incarnation of the press is capable of generating pressures of up to 28 GPa depending on choice of anvil [6].

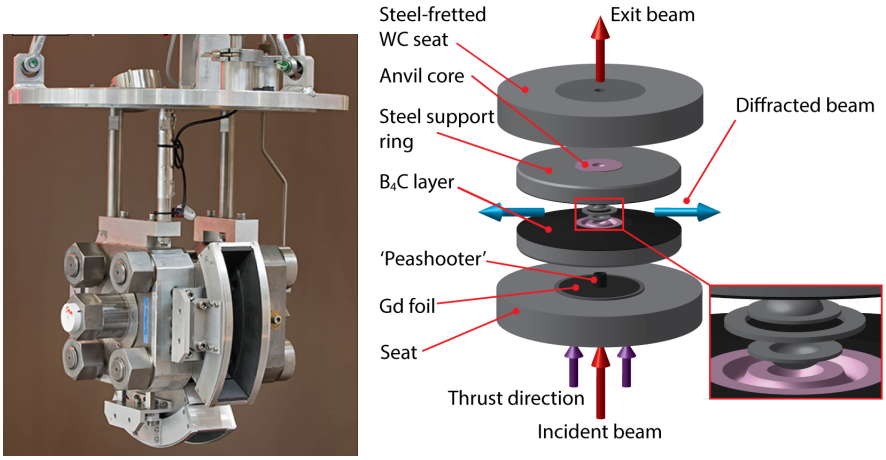

Figure 2.5: A photograph of a V3 Paris-Edinburgh pressure cell (left), used at PEARL; and a diagrammatic representation of the interior of the P-E press (right), with a close-up on the sample environment. Both images adapted from [6].

The press operates as follows. The sample, of approximate volume 88 mm^3, is placed within a gasket composed of a null-scattering material, such as titanium-zirconium alloy (TiZr). Included with the sample is a pressure-transmitting medium (PTM), to ensure pressure is applied hydrostatically to the entire sample [10]. Common pressure-transmitting media include mixtures of methanol and ethanol, or a mixure of pentanes (all deuterated to avoid incoherent scattering issues).

In addition to the sample and pressure-transmitting medium, the gasket also contains a small amount of pressure calibrant. This is a material for which the crystal lattice parameter(s) as a function of pressure are well known. By determining the unit-cell parameter(s) of the pressure calibrant on experiment, it is possible to calculate an applied pressure value using an equation of state - a curve describing the evolution

of the lattice parameters with pressure - and therefore measure the pressure without having to remove the press and sample from the neutron beam and instrument at each pressure point [6].

The prepared gasket is placed into the press between two anvils, composed of a material such as tungsten carbide (WC), zirconia-toughened alumina (ZTA), or sintered diamond (SD). Hydraulic pressure is then applied. When the desired applied load is reached and the sample is aligned, the shutter is opened and the neutron beam is allowed to reach the sample. Neutrons diffracted from the sample emerge and strike the 90-degree bank of detectors [7].

However, there are limitations to the P-E setup. The maximum achievable pressure is still lower than that of a DAC. The other caveat is that although a P-E press can handle extremes of pressure very well, there are currently limits to the achievable combination of temperature and pressure that can be applied simultaneously to a sample [8]. Whereas a DAC sample can be heated using lasers, there is no similar optical access (or instrument space) to allow this form of heating to take place with the P-E cell. Through the use of external cartridge heaters, the equipment is capable of reaching 500 K at 25 GPa. This can be pushed further to 1400 K using an internal heating system, but the maximum pressure is then limited to 10 GPa. Additionally, due to the geometry of the P-E cell and placement of detectors, the maximum d-spacing range that can be routinely studied in a P-E experiment on PEARL is 4 Å. This limits the observation of any reflections that occur at d-spacings beyond 4 Å, potentially hindering full structural analysis. D-spacings of up to 12 Å can be studied to a limited extent by exploiting the timing of the ISIS neutron pulses. However, long collection times are required to acquire refineable diffraction data over this range [6].

For the purposes of this thesis, studies will focus solely on the use of the P-E press to generate extremes of pressure, rather than via diamond-anvil cells.

Rietveld refinement and data analysis

Useful crystallographic parameters were extracted from PEARL diffraction data in this work using the technique of *Rietveld refinement*. This is a least-squares minimisation process used to fit a mathematical model to a dataset - in this case, fitting a crystallographic model with variables such as lattice parameters, atomic positions, thermal displacement factors, site occupancies, background noise, and phase fractions, to experimental diffraction data [2]. All of these factors have been refined to some extent for each crystal structure studied in this work, with more specific details given in the experimental sections of the relevant chapters.

In this particular work, the refinement software used reports the difference between any computed refinement model and the experimental data with a series of difference measurements. R_p and R_{wp} are known as residual

factors, or more commonly R-factors; while another type of difference measurement is the mathematical 'goodness of fit' (GoF) measurement. All have slightly different methods of calculation, but each gives some quantitative indication as to how close the Rietveld-refined model is to being an "answer" to the question posed by the data [2], and many crystallographers have their own preference as to which factor to focus on during refinement. R_p, R_{wp} and GoF values have been quoted in this work for refinements where applicable.

Once a series of crystal structures of suitable chemical sensibility and low enough R-factors and/or chi-square value are produced, their lattice parameters are plotted as a function of pressure to yield what is known as an *equation of state* (EoS). A line or curve is fitted to this plot to allow prediction of the pressure response of the material, as well as the calculation of factors such as the material's bulk modulus.

Different varieties of equation of state curve are available to fit to data - the choice of which is governed partly by the shape of the underlying plot, partly by the error values in the experimental data, partly by which thermodynamic variables are of interest or desired, partly by the number of data points available, and partly by personal preference where multiple EoS types produce similar results [11].

This work employs what is known as the *Birch-Murnaghan* equation of state, which is shown in Equation 4 below.

$$P(V) = \frac{3B_0}{2}\left((\frac{V_0}{V})^{\frac{7}{3}} - (\frac{V_0}{V})^{\frac{5}{3}}\right)\left(1 + \frac{3}{4}(B_0' - 4)((\frac{V_0}{V})^{\frac{2}{3}} - 1\right) \tag{4}$$

Birch-Murnaghan equation of state. Where P = pressure, V = the volume at pressure P, V_0 = the initial volume, B_0 = the bulk modulus, and B' = the first derivative of the bulk modulus (also known as the pressure derivative).

Computational software is generally used to fit this equation to experimental data, allowing the production of B_0 and B' values, which act as a measure of the material's 'stiffness'.

2.3 Resonant Acoustic Mixing

Resonant Acoustic Mixing (RAM) is a system developed by ResoDyn Systems. This technology combines elements of sonication and shaker tables to provide a low-energy, low-frequency mixer. The RAM system operates by clamping a sample container into place on top of the instrument (Figure 2.6). This clamp is attached to a metal plate, which is in turn connected to the rest of the RAM mixer by a series of springs.

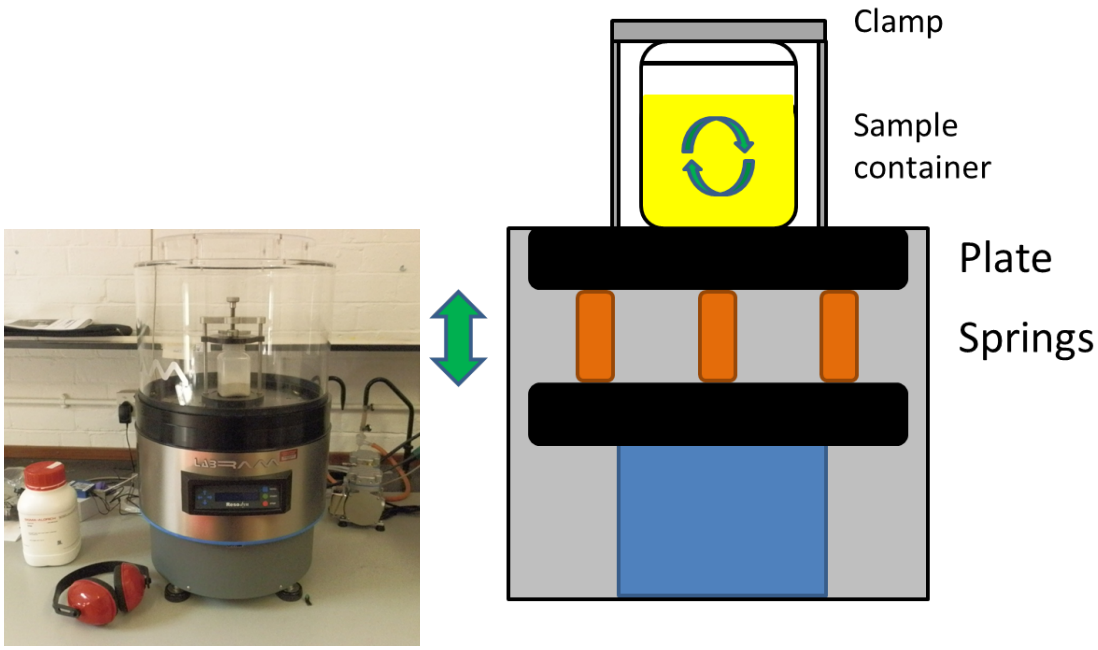

Figure 2.6: A diagrammatic representation of how a Resonant Acoustic Mixer operates.

A transducer produces low-frequency acoustic waves to oscillate the metal plate, with the help of the aforementioned springs. This oscillation is precisely tuned by the hardware and software so that the sample environment is exposed to a specified acceleration, specified as a multiple of G-force (9.81 m/s^2).

This oscillation of the sample environment induces microscopic mixing zones within the sample. The obvious application of this technology is for material mixing, and for preparing compositions and mixtures. The technology can work with powder-based, liquid, or viscous solid mixtures. This is especially useful for energetic materials, which can encompass all of these types of mixtures.

Additionally, current methods of mixing energetic materials involve the use of physical mixing media, such as blades or impellers. These are difficult to clean, and can cause problems with certain sensitive materials if they deliver too much friction or impact when in operation, or cause unwanted deformations or reductions in particle size [12, 13, 14].

Other non-physical methods of mixing, such as sonication, are equally problematic for energetic materials, as the high-frequency waves produced by sonication can also impart unsafe levels of energy to a material and can result in cavitation phenomena such as hotspots, causing initiation of the material [15].

RAM mitigates these concerns by using very low-frequency, low-energy acoustic waves to drive its mixing mechanism. The frequency difference between sonication (typically around 20,000 Hz) and RAM (typically around 60 Hz) is several orders of magnitude in size. The system can also be used with any sample container that can withstand the forces of the clamping system, and does not exceed the maximum mass of the metal

plate. This allows any material to be "mixed in-case", if need be, without any physical mixing media [16].

There are other applications of this technology. The RAM system can be used to coat materials, as seen in Figure 2.7 [17]. RAM technology can also be used to prepare co-crystals with the application of a small amount of solvent, analogous to solvent-drop grinding. This method has been successfully used to prepare both pharmaceutical and energetic co-crystals. Synthetic and mixing processes have also been found to be easily scalable using RAM technology, compared to techniques such as ball milling, potentially mitigating a key problem in energetic materials synthesis [17, 18, 19, 20].

Figure 2.7: An example of pellet coating performed using the RAM mixer - a series of polyurethane pellets have been coated with graphene nanoplatelets.

The use of RAM technology for co-crystallisation will be explored more fully in Chapter 5.

2.4 References

[1] A. Glazer, *Crystallography Reviews*, 2013, **19(3)**, 117–124.

[2] V. K. Pecharsky and P. Y. Zavalij, *Fundamentals of Powder Diffraction and Structural Characterization of Materials*, 2nd edn., 2009.

[3] G. Bacon, *Neutron diffraction*, 2nd edn., Oxford University Press, 1962.

[4] B. Willis and C. Carlile, *Experimental Neutron Scattering*, Oxford University Press, 2012.

[5] C. Hammond, *The Basics of Crystallography and Diffraction*, 4th edn., Oxford University Press, 2015.

[6] C. L. Bull, N. P. Funnell, M. G. Tucker, S. Hull, D. Francis and W. G. Marshall, *High Pressure Research*, 2016, **36**, 493–511.

[7] J. Besson, R. Nelmes, G. Hamel, J. Loveday, G. Weill and S. Hull, *Physica B: Condensed Matter*, 1992, **180**, 907–910.

[8] J. Besson and R. Nelmes, *Physica B: Condensed Matter*, 1995, **213**, 31–36.

[9] C. L. Bull, M. Guthrie, S. Klotz, J. Philippe, T. Strässle, R. J. Nelmes, J. S. Loveday and G. Hamel, *High Pressure Research*, 2005, **25(4)**, 229–231.

[10] S. Klotz, J. Chervin, P. Munsch and G. Le Marchand, *Journal of Physics D: Applied Physics*, 2009, **42(7)**, 075413.

[11] R. J. Angel, *Reviews in Mineralogy and Geochemistry*, 2000, **41(1)**, 35–59.

[12] C. Suryanarayana, *Progress in Materials Science*, 2001, **46(1-2)**, 1–184.

[13] M. L. Trudeau, R. Schulz, D. Dussault and A. Van Neste, *Physical Review Letters*, 1990, **64(1)**, 99–102.

[14] G. Gorrasi, M. Sarno, A. Di Bartolomeo, D. Sannino, P. Ciambelli and V. Vittoria, *J. Polym. Sci. B Polym. Phys.*, 2007, **45(5)**, 597–606.

[15] A. B. Morgan and J. D. Harris, *Polymer*, 2004, **45(26)**, 8695–8703, doi:10.1016/j.polymer.2004.10.067.

[16] ResoDyn Corporation, "ResonantAcoustic Mixing - Technical White Paper", , 2010.

[17] K. S. Hope, H. J. Lloyd, D. W. Ward, A. A. Michalchuk and C. R. Pulham, *Proceedings of the 18th NTREM Seminar*, 2015, 134–143.

[18] K. S. Hope, D. W. Ward, H. J. Lloyd, S. Hunter, C. L. Bull and C. R. Pulham, *Proceedings of the 19th NTREM Seminar*, 2016, 132–140.

[19] D. J. am Ende, S. R. Anderson and J. S. Salan, *Org. Proc. Res. Dev.*, 2014, **18(2)**, 331–341.

[20] S. R. Anderson, D. J. am Ende, J. S. Salan and P. Samuels, *Prop., Expl., Pyro.*, 2014, **39(5)**, 637–640.

Chapter 3

High-pressure studies of CL-20 co-crystals

This chapter describes the high-pressure behaviour of two CL-20 co-crystals, namely 2(CL-20):HMX and CL-20:TNT, and one CL-20 solvate - 2(CL-20):hydrogen peroxide. Some background about the materials involved in this chapter is given below.

CL-20 (Figure 3.1a), alternatively known as "hexanitro-hexaaza-isowurtzitane" (and hence often abbreviated HNIW), is an energetic material first synthesised by the US Navy in the late 1980s, as part of a programme to develop new energetic materials with increased performance and decreased sensitivity to stimuli [1]. With its strained nitramine cage structure, CL-20 certainly succeeded in one of these aspects - at present it is one of the most powerful energetic materials [2]. However, its success in other areas - reduced sensitivity - was substantially less pronounced. CL-20 was found to display markedly increased sensitivity compared to common energetic materials used for civilian and military applications. This has limited its use in modern-day compositions and so it is usually included in only small quantities as a minor component to add additional explosive output, rather than forming the bulk of a munition or charge in its own right [2].

HMX (Figure 3.1b), or more systematically "1,3,5,7-tetranitro-1,3,5,7-tetrazocine" (also known as Octogen), has been used in military applications since the closing months of the Second World War [3]. HMX was originally developed as an improved replacement for the earlier explosive, RDX (see Chapter 1), and thanks to having a reasonable ratio of sensitivity to performance, has formed a mainstay of military compositions for most of the mid-to-late 20th century [4].

From modern video games such as Minecraft, to the classic perils of Wile E. Coyote in Looney Tunes, **TNT** (or 1,3,5-trinitrotoluene, Figure 3.1c) has entered the public consciousness almost as a synonym for "explosive". This material has a long history of use, both in civilian and military applications [3]. It possesses a comparable impact sensitivity to RDX, but has a greater solubility in water and is well known as an environmental toxin [5].

Hydrogen peroxide (HP, Figure 3.1d) is perhaps most commonly known for its use in the fashion industry as a hair bleaching agent. However, it is also used as an oxidiser in rocket propellants, and in high concentrations ($\geq$ 85 %) it also finds use as a propellant in its own right, due to its ability to readily decompose

into steam and oxygen in the presence of a catalyst.

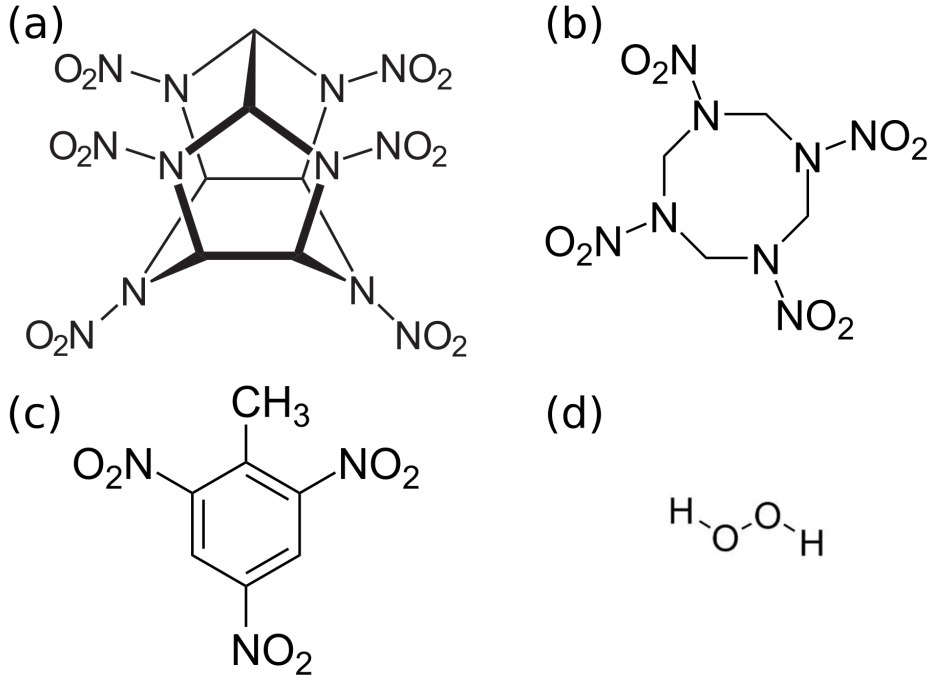

Figure 3.1: Molecular structures of (a) CL-20 - $C_6H_6N_{12}O_{12}$; (b) HMX - $C_4H_8N_8O_8$; (c) TNT - $C_7H_5N_3O_6$; (d) HP - H_2O_2.

CL-20, HMX and TNT also exhibit diverse polymorphic behaviour. In particular for CL-20, the fact that it exists in six known forms (each with differing levels of sensitivity) is another potential factor in its unsuitability as a single-component material. Details of these forms are given in Table 3.1 below, with the ϵ-form being the most stable under ambient conditions.

Table 3.1: Details of the six forms of CL-20.

Form	Crystal System	Space Group	Conditions for formation	Reference
Alpha (α)	Orthorhombic	$Pbca$	Hydrated form of CL-20	[6]
Beta (β)	Orthorhombic	$Pca2_1$	Crystallisation from benzene	[6]
Gamma (γ)	Monoclinic	$P2_1/n$	Phase transition from β-form at $\sim$ 185 $^{\circ}C$	[7]
Delta (δ)	Presumed hexagonal	Structure not known	Apparent phase transition from α-form at $\sim$ 130 $^{\circ}$C	[6]
Epsilon (ϵ)	Monoclinic	$P2_1/n$	Most stable form under ambient conditions	[7]
Zeta (ζ)	Monoclinic	$P2_1/n$	Phase transition from γ at 0.7 GPa	[8]

For HMX, the polymorphic behaviour is less pronounced - four forms exist, with the β-form being the most stable at room temperature and pressure. Details of each form of HMX are given in Table 3.2 below.

Table 3.2: Details of the four forms of HMX.

Form	Crystal System	Space Group	Conditions for formation	Reference
Alpha (α)	Orthorhombic	$Fdd2$	Crystallisation from hot nitric acid	[9]
Beta (β)	Monoclinic	$P2_1/n$	Most stable form under ambient conditions	[10]
Gamma (γ)	Monoclinic	Pn	Hydrated form of HMX	[11]
Delta (δ)	Hexagonal	$P6_1$	Phase transition from β-form above 160 °C	[12]

Only two polymorphs are known for TNT. The orthorhombic form is the most stable under ambient conditions, but converts to the monoclinic form at elevated temperatures. The details of these polymorphs are shown in Table 3.3.

Table 3.3: Details of the two forms of TNT.

Form	Crystal System	Space Group	Conditions for formation	Reference
Ortho-TNT	Orthorhombic	$Pca2_1$	Most stable form under ambient conditions	[13]
Mono-TNT	Monoclinic	$P2_1/a$	Slow crystallisation from hot ethanol	[14]

Co-crystals of CL-20 are of particular interest in the field of energetic materials. As CL-20 possesses exceptional energetic performance tempered only by its relatively high sensitivity, it is believed that co-crystallisation of CL-20 can serve to tune this sensitivity without compromising significantly on the explosive power.

2(CL-20):HMX was first prepared in 2011 by Bolton *et al.*, and characterised by single-crystal X-ray diffraction. The material crystallises in the monoclinic crystal system with space group $P2_1/n$, with four molecules of CL-20 located entirely within the unit cell, eight corner-sharing molecules of HMX, and two face-sharing molecules of HMX. The structure shows a layered arrangement, consisting of a plane of HMX molecules on two opposing faces of the unit cell, separated by a bi-layer of CL-20 molecules (Figure 3.2) [15].

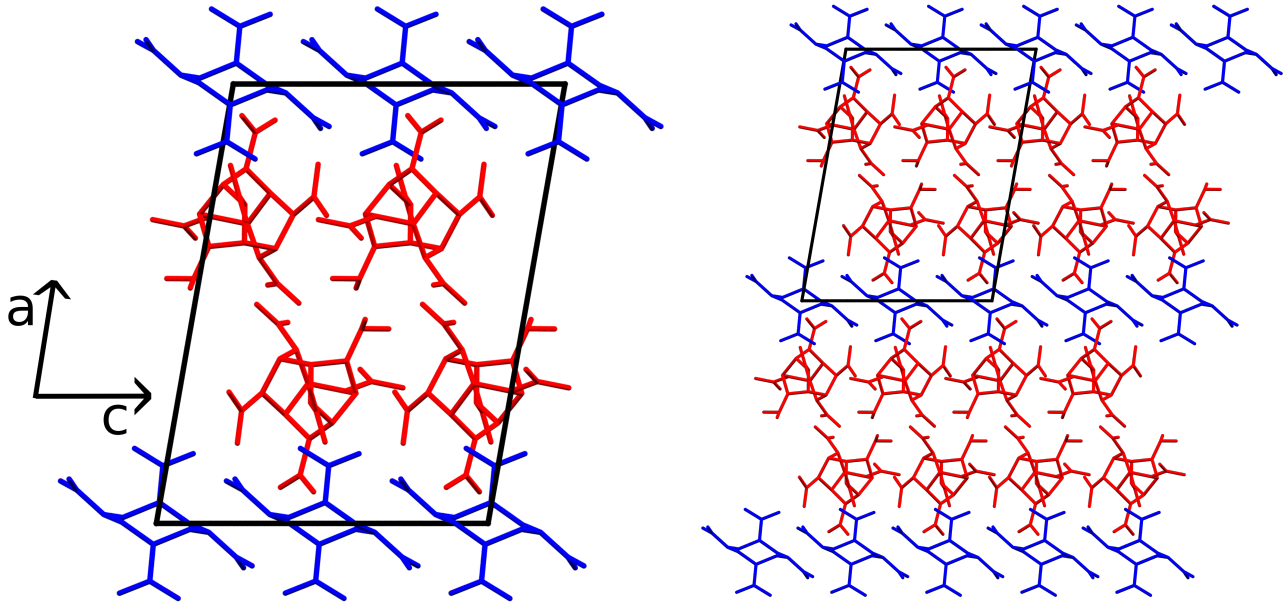

Figure 3.2: Crystal structure of 2(CL-20):HMX reproduced from the Cambridge Structural Database (refcode ZEBHOH from [15]), viewed along the *b*-axis. CL-20 molecules are highlighted in red, with HMX molecules in blue, showing the layered packing present in this crystal structure. The unit cell is shown on the left, with an expanded 2 x 2 packing arrangement to the right. Hydrogen atoms have been omitted for clarity.

This co-crystal was initially reported by Bolton *et al.* to possess greatly reduced impact sensitivity relative to ϵ-CL-20, determined using their in-house impact testing apparatus [15]. However, subsequent impact sensitivity testing by Nalas Engineering has revealed that 2(CL-20):HMX actually possesses *greater* impact sensitivity relative to ϵ-CL-20 [16]. This discrepancy in testing results means the material's potential behaviour under high-pressure conditions is of interest.

CL-20:TNT crystallises in the orthorhombic crystal system with space group *Pbca*, with eight molecules each of TNT and CL-20 per unit cell. This system also exhibits a layered packing arrangement, with layers of TNT and CL-20 propagating throughout the structure (Figure 3.3) [17].

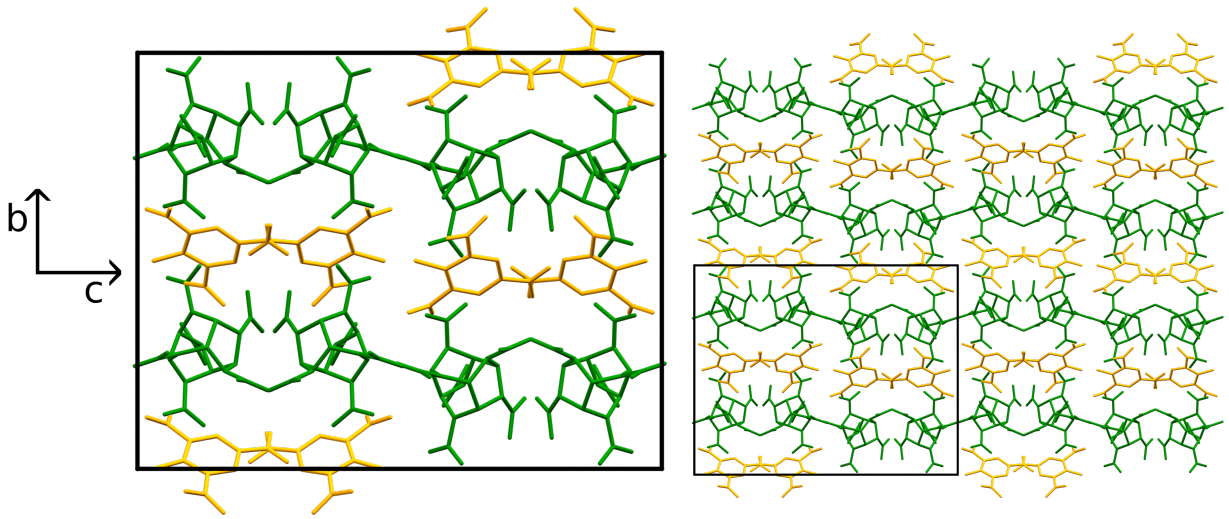

Figure 3.3: (a) Crystal structure of CL-20:TNT reproduced from the Cambridge Structural Database (ref-code IZUZUZ from [17]), viewed along the *a*-axis, with an expanded 2x2 packing arrangement in (b). CL-20 molecules have been highlighted in green and TNT molecules displayed in orange, with the layering clearly apparent. Hydrogen atoms have been omitted for clarity. From this viewpoint, it appears that adjacent molecules of CL-20 or TNT are linked together. However, this is merely a misleading impression given by adjacent NO_2 groups partially-eclipsing each other.

This co-crystal has also been reported by Bolton *et al.* to display reduced impact sensitivity compared to ϵ-CL-20 [17]. At present, no impact sensitivity testing has been performed by other groups with standardised apparatus to confirm this statement.

2(CL-20):HP crystallises in two distinct polymorphs depending on the crystallisation conditions - a stable orthorhombic form (*Pbca* space group), and a metastable monoclinic form ($P2_1/n$ space group). As it was difficult to produce the monoclinic form on the scale required for neutron diffraction due to crystallisation issues, this study focused on the orthorhombic polymorph, and the 2(CL-20):HP section of this chapter will focus on that form in particular.

The orthorhombic 2(CL-20):HP form (Figure 3.4) contains four molecules of CL-20 entirely within the unit cell, four face-sharing molecules of CL-20, one molecule of HP within the unit cell, and twelve edge-sharing molecules of HP. All hydrogen peroxide sites possess 50 % fractional occupancy - i.e. there is a 50 % chance of finding atoms in each of these positions. Each peroxide molecule is, in turn, disordered over two adjacent sets of fractional co-ordinates with a 50:50 split of relative occupancy between them. Given the large difference in relative size between CL-20 and hydrogen peroxide molecules, it would not be appropriate to describe the structure as "layered" in the same way the two previous CL-20 systems are. However, the HP molecules do occupy three distinct "bands" across the structure - two on opposing unit cell faces, and one parallel through the middle of the unit cell [18].

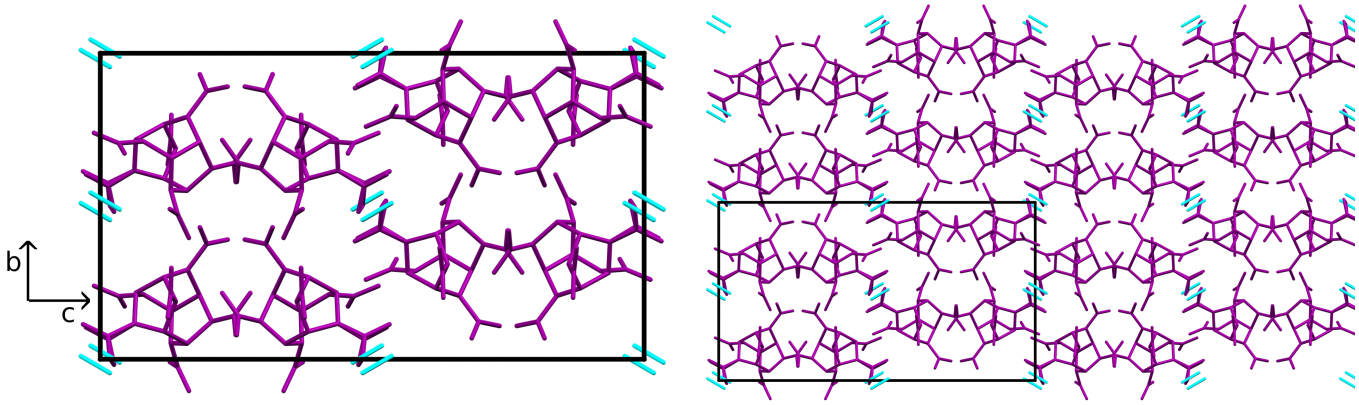

Figure 3.4: Crystal structure of ortho-CL-20:HP reproduced from the Cambridge Structural Database (ref-code AZAMIZ from [18]), viewed along the a-axis, with an expanded 2x2 packing arrangement on the right. CL-20 molecules have been highlighted in purple and HP molecules in cyan, showing the "banding" of the peroxide molecules. Hydrogen atoms have been omitted for clarity. Each HP molecule is disordered over two adjacent sites with 50 % occupancy.

To date, no high-pressure diffraction or spectroscopic studies of these materials (or indeed any other energetic co-crystal) have been reported in the open literature. Therefore, following successful beamtime proposals, these materials were studied on the PEARL instrument in November 2015 [2(CL-20):HMX]; February 2017 (CL-20:TNT); and March 2018 [2(CL-20):HP]. The details and results of these experiments will be described in the next sections of this chapter.

3.1 Experimental

3.1.1 Preparation of 2(CL-20):HMX

The co-crystal was prepared through adaptation of a known method, described by Nalas Engineering [16].

Materials utilised in this preparation were as follows: ϵ-CL-20 (hexanitro-hexaaza-isowurtzitane, $C_6H_6N_{12}O_{12}$, acquired from DSTL), β-HMX ($C_4D_8N_8O_8$, prepared previously at the University of Edinburgh by Millar), acetonitrile-d_3 (CD_3CN, 99.9 %, purchased from Cambridge Life Sciences), and isopropanol-d_8 [$CD_3CD(OD)CD_3$, 99.9 %, purchased from Cambridge Life Sciences].

Stoichiometric quantities of ϵ-CL-20 and β-HMX-d_8 (0.374 g and 0.126 g respectively) were combined in a 15 ml sellotaped glass sample vial. A 1:1 (v/v) solution (10 ml) of acetonitrile-d_3 and isopropanol-d_8 was prepared, and a drop ($\sim 30\mu L$) of this was added to the mixture of energetic materials.

The vial was then immediately subjected to a one-hour mixing cycle on a ResoDyn LabRAM Resonant Acoustic Mixer (RAM, Figure 3.5) at an acceleration of 100 G. This process was repeated twice. Powder X-ray diffraction patterns were recorded for the sample after each RAM cycle. The sample was subsequently suspended in a mixture of 4:1 deuterated methanol and ethanol ($\sim$ 2 ml) and stirred for three hours - further

driving the formation of the co-crystal - before being dried in a vacuum desiccator. This additional solution-based step was required as the geometry of sample vials used in the RAM for this experiment inhibited full conversion to co-crystal, on account of incomplete mixing.

Figure 3.5: A ResoDyn LabRAM Resonant Acoustic Mixer.

The identity of the sample was confirmed using powder X-ray diffraction, with data collected using a Bruker D2 Phaser in flat-plate Bragg-Brentano geometry, using Cu-Kα radiation over a 2θ range of 5 to 45 °. Experimental and simulated X-ray patterns of the material are shown in Figure 3.6. Small amounts of un-reacted ϵ-CL-20 and β-HMX were identified from the powder X-ray diffraction patterns - 7.2 mole-% ϵ-CL-20 and 1.6 mole-% β-HMX. The CL-20 impurity was underestimated during initial pre-experiment analysis, hence why the neutron experiment proceeded with what appears to be a rather impure sample. More accurate phase fractions were determined during post-experiment analysis.

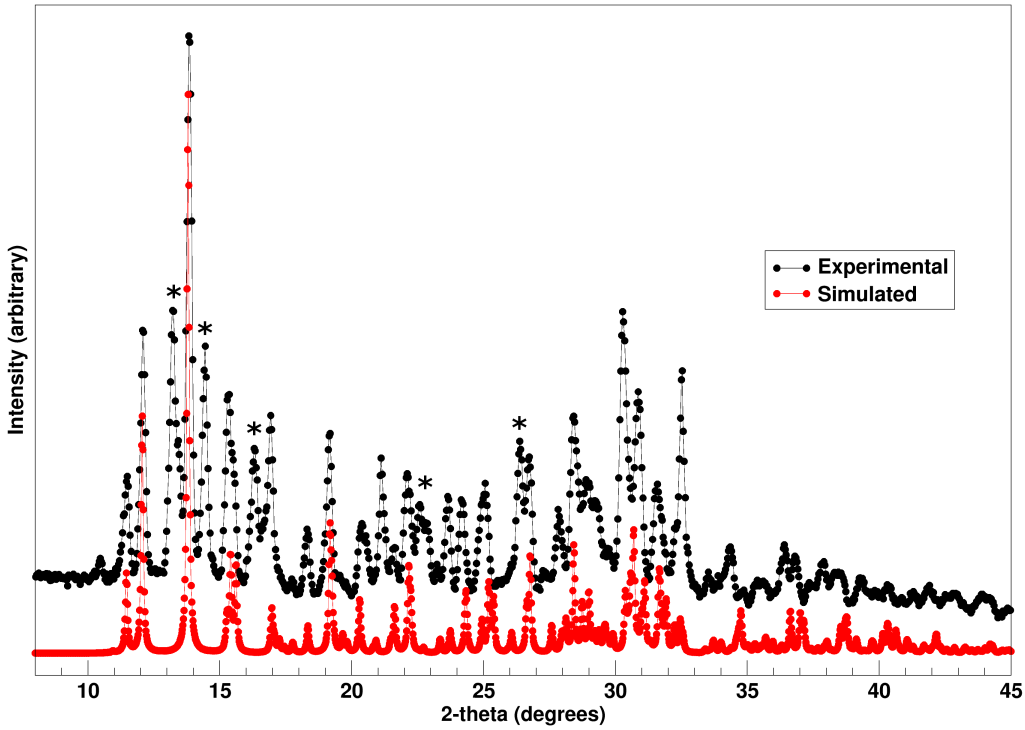

Figure 3.6: Powder X-ray diffraction patterns of 2(CL-20):HMX. The experimental pattern is shown in black. A simulated pattern at the appropriate X-ray wavelength, generated using Mercury, is shown in red. Impurity peaks arising from ϵ-CL-20 and β-HMX are indicated with asterisks in the experimental pattern.

After careful transportation of the sample to the ISIS Neutron Facility, it was loaded into a Paris-Edinburgh pressure cell following the common procedures outlined in Section 3.1.4. The maximum load achieved in this particular experiment was 55 tonnes, equating to a pressure of approximately 3.5 GPa.

3.1.2 Preparation of CL-20:TNT

Deuteration of TNT

Deuterated 2,4,6-trinitrotoluene (TNT-d_5) was prepared through direct synthesis from toluene-d_8. This method was adapted from a published synthetic route for TNT [19], and is shown schematically in Figure 3.7.

The following materials were employed in this synthetic method: nitric acid (HNO_3, 98 %, purchased from Sigma-Aldrich), fuming sulfuric acid ($H_2SO_4.SO_3$, 20 % oleum, purchased from Sigma-Aldrich), toluene-d_8, ($C_6D_5CD_3$, 99.9 %, purchased from Cambridge Life Sciences), chloroform-d_1, ($CDCl_3$, 99.9%, purchased from Sigma-Aldrich), sodium hydrogen carbonate ($NaHCO_3$, purchased from Fisher Scientific), deuterium oxide (D_2O, 99.9 %, purchased from Sigma-Aldrich), and carbon tetrachloride (CCl_4, purchased from Fisher Scientific).

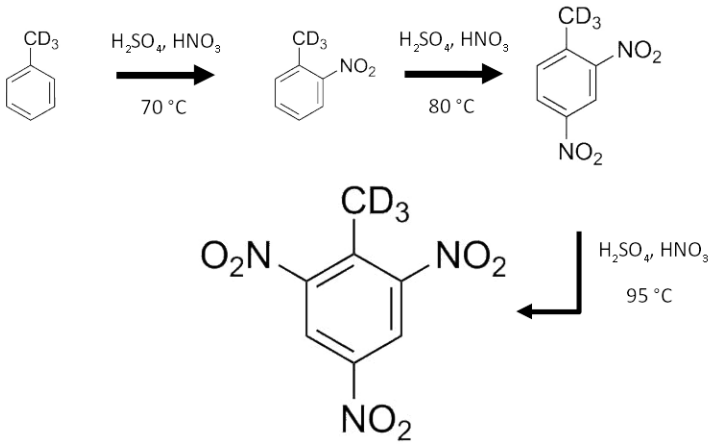

Figure 3.7: Scheme for the synthesis of TNT-d_5 from toluene-d_8, as performed in this study.

A nitrating mixture was formed by carefully combining 6 ml of the nitric acid with 17.5 ml of fuming sulfuric acid. This mixture was cooled to -5 °C using a PolarBear Crystal chiller-hotplate (Figure 3.8), manufactured by Cambridge Reactor Design. 4.5 ml of toluene-d_8 was added dropwise over twenty minutes, with the temperature being maintained at -5 °C throughout.

Figure 3.8: A PolarBear Crystal chiller-hotplate, used to perform heating and cooling steps in this synthesis.

Once the toluene had been completely added, the reaction mixture was allowed to warm to room temperature. The mixture was then heated to 70 °C for one hour. At this point, the mixture was further heated to 85 °C for 45 minutes, and then 90 °C for another 45 minutes. These heating steps initiated progressive nitrations of the aromatic ring system. After 45 minutes at 90 °C had elapsed, the mixture was poured hot into a clean flask and allowed to cool to room temperature. The PolarBear was then employed to cool the mixture to -10 °C , where it was held for fifteen minutes to ensure any remaining reaction was quenched within the flask.

A quantity of deuterated chloroform ($\sim$ 25 ml) was added, and the mixture allowed to separate into distinct organic and aqueous layers. The aqueous layer was separated and disposed of safely. Any remaining acid in the organic layer was neutralised with a 30 % m/v solution of sodium hydrogen carbonate in D_2O. Following the evolution of CO_2 from neutralisation, solid TNT-d_5 began to precipitate out in the flask. This product was vacuum filtered, and dried overnight in a desiccator. The solid TNT-d_5 was then recrystallised twice from hot carbon tetrachloride. The crystallisation solvent was again removed using vacuum filtration, and the recrystallised sample was stored in a vacuum desiccator. The success of the preparation, and the extent of deuteration, were verified using powder X-ray diffration and a combination of ^{1}H- and ^{2}H-NMR spectroscopy.

An experimental powder X-ray diffraction pattern of TNT-d_5 is shown alongside a powder pattern from the program Mercury in Figure 3.9, while the ^{1}H- and ^{2}H-NMR spectra are shown in Figure 3.10.

The powder X-ray diffraction pattern was collected on a flat-plate Bruker D2 Phaser, using Cu-Kα radiation for the 2θ range of 5 to 45 $^\circ$ for a duration of twenty minutes. The NMR spectra were collected using a Bruker AVA500 spectrometer (for the ^{1}H-NMR), and a Bruker PRO500 spectrometer (for the ^{2}H-NMR). Deuterated chloroform was used as the solvent for ^{1}H data, and hydrogenated chloroform used for ^{2}H data. Shimming, locking and normalisation corrections were applied by the instrument automation suite.

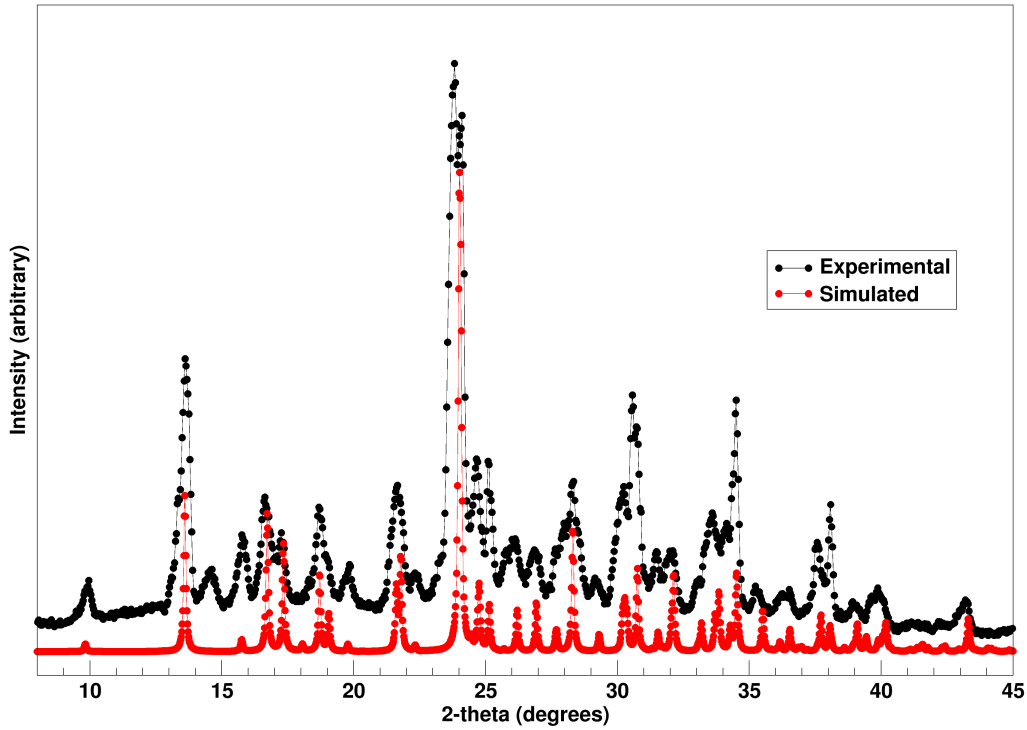

Figure 3.9: Experimental powder X-ray diffraction data of TNT-d_5 (black) at 1.5406 Å, compared to a pattern simulated from an existing CIF file (reference [13], ref-code ZZZMUC01 in the Cambridge Structural Database). For safety reasons, the sample was only very lightly ground prior to analysis, as rough or excessive grinding can cause initiation of energetic samples *via* friction and electrostatic shock, so a degree of preferred orientation may be present in the experimental data.

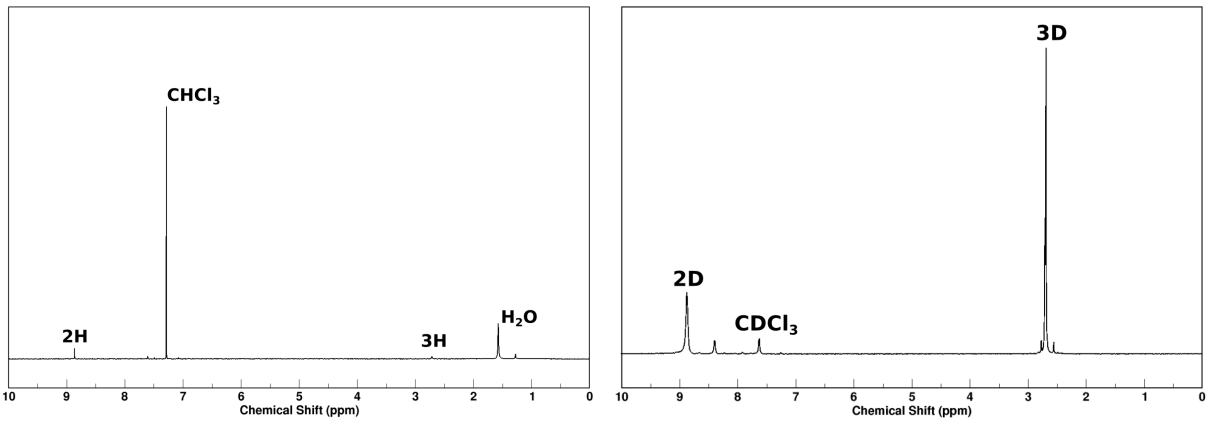

Figure 3.10: NMR spectra of TNT-d_5. The ^{1}H spectrum is on the left, and the ^{2}H spectrum is on the right. The largest peaks (with the greatest integration values) in the ^{1}H spectrum result from the (negligible) quantity of hydrogen contained within the deuterated solvent (rated at 99.9 % purity). This indicates that TNT-d_5 is in a smaller relative quantity than the residual non-deuterated solvent, and was therefore presumed to be present at a concentration of < 0.1 mol%.

CL-20:TNT preparation

This material was prepared through a new RAM-based method, rather than following the original evaporative route from [17], as this allowed the material to be prepared on a larger scale in a more manageable

timeframe.

Materials utilised in this preparation were as follows. ϵ-CL-20 (hexanitro-hexaaza-isowurtzitane, $C_6H_6N_{12}O_{12}$, acquired from DSTL), 2,4,6-trinitrotoluene-d_5 ($C_6D_3CD_3(NO_2)_3$, TNT-d_5, prepared by the method described earlier), and acetone-d_6 (C_3D_6O, 99.9 %, purchased from Cambridge Life Sciences).

Firstly, stoichiometric samples of ϵ-CL-20 and TNT-d_5 in a 1:1 molar ratio (0.329 and 0.171 g respectively), were gently ground together with two drops of acetone-d_6 ($\sim$ 60 μl) to generate seed crystals within the bulk mixture. The mixture was then placed into a purpose-built 15 ml metal sample vial, and a further one drop of acetone-d_6 ($\sim$ 30 μl) added. The ground material then underwent a RAM mixing cycle at 50 G for one hour using a ResoDyn LabRAM Resonant Acoustic Mixer, which had modifications made by The Falcon Project to allow improved processing of energetic materials (Figure 3.11).

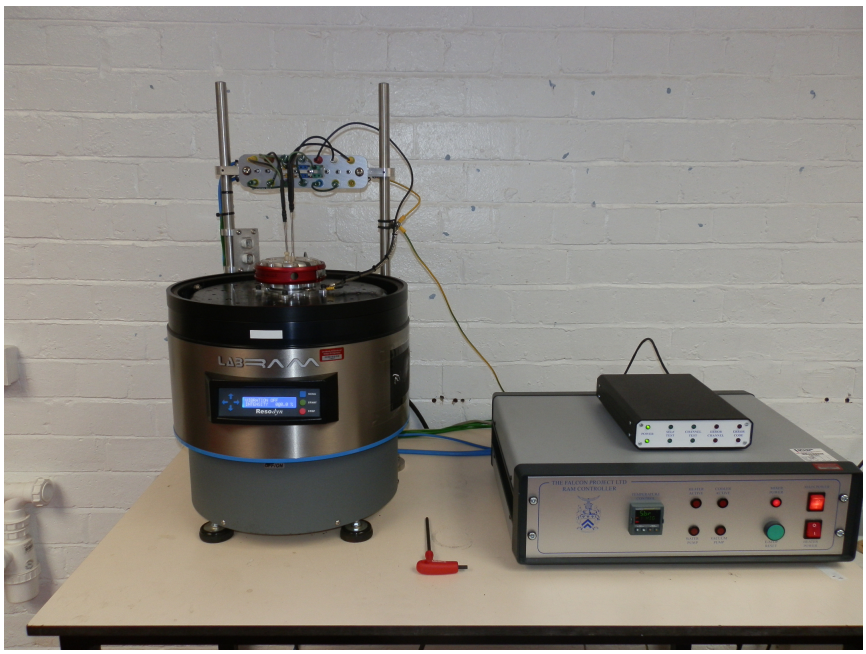

Figure 3.11: Improved LabRAM setup, with additions developed by The Falcon Project enabling additional monitoring and control of the sample environment, and safer handling of energetic materials.

This RAM mixing cycle was repeated twice to generate product at $\sim$ 70 % yield. The remaining 30 % of the product was not recovered as a result of electrostatic build-up that caused some of the material to adhere to the sample container in a manner which rendered its removal either difficult or unsafe. The success of the co-crystallisation was verified by powder X-ray diffraction, as shown in Figure 3.12. One of the modifications made by Falcon to the RAM setup was the use of sample vials with rounded internal geometry, specifically designed to maximise the RAM's mixing abilities, negating the build-up of any un-reacted starting material, as occurred in the 2(CL-20):HMX system. As with the previous experimental patterns, the powder X-ray diffraction was performed using a Bruker D2 Phaser in flat-plate geometry with Cu-Kα radiation, over a 2θ

range of 5 to 45 ° for a total collection duration of 20 minutes.

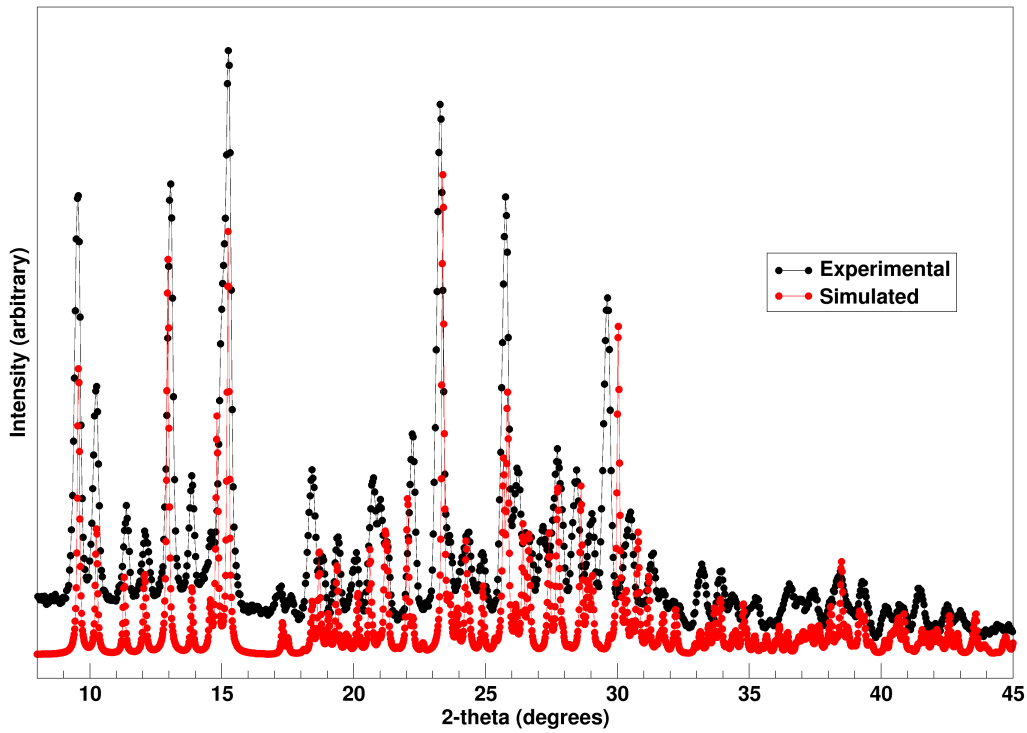

Figure 3.12: Experimental powder X-ray diffraction data of CL-20:TNT (black) at 1.5406 Å, compared to a pattern simulated from the original CIF file (red, reference [17], ref-code IZUZUZ in the Cambridge Structural Database). For safety reasons, the sample was only very lightly ground prior to analysis, so a degree of preferred orientation may be present in the experimental pattern.

Following transport of the sample to the ISIS Neutron Source, it was loaded into a Paris-Edinburgh pressure cell according to the common procedures outlined in the upcoming section 3.1.4. The maximum load applied to the sample in this study was 35 tonnes, giving a pressure of approximately 4.1 GPa. However, for reasons that will be outlined in Section 3.2.2, useful structural data was only obtained up to approximately 3.5 GPa.

3.1.3 Preparation of ortho-2(CL-20):HP

The orthorhombic polymorph of 2(CL-20):HP was prepared *via* the method originally outlined in reference [18].

Materials utilised in this preparation were as follows. ϵ-CL-20 (hexanitro-hexaaza-isowurtzitane, $C_6H_6N_{12}O_{12}$, purchased from Event Horizon Ltd), hydrogen peroxide (H_2O_2, 90 wt.% concentration, acquired from The Falcon Project), and acetonitrile (CH_3CN, 99.9 %, purchased from Sigma-Aldrich).

Initially, a quantity of ϵ-CL-20 ($\sim$ 0.481 g) was dissolved in the minimum amount of acetonitrile ($\sim$ 10 ml) at 50 °C in a beaker. Once all of the CL-20 had dissolved, the beaker was removed from the heat, and a

stoichiometric quantity of hydrogen peroxide ($\sim$ 7 ml) was added.

After 5 minutes of vigorous stirring, a white solid began to precipitate. This solid product was separated out by vacuum filtration, and left to dry under air for 30 minutes. The material was then safely stored.

Successful synthesis was confirmed by powder X-ray diffraction, as shown in Figure 3.13. Powder X-ray diffraction was performed using a Bruker D8 Advance on a 0.5 mm diameter capillary with Cu-Kα radiation, over a 2θ range of 5 to 45 $^\circ$ for a total time duration of 40 minutes.

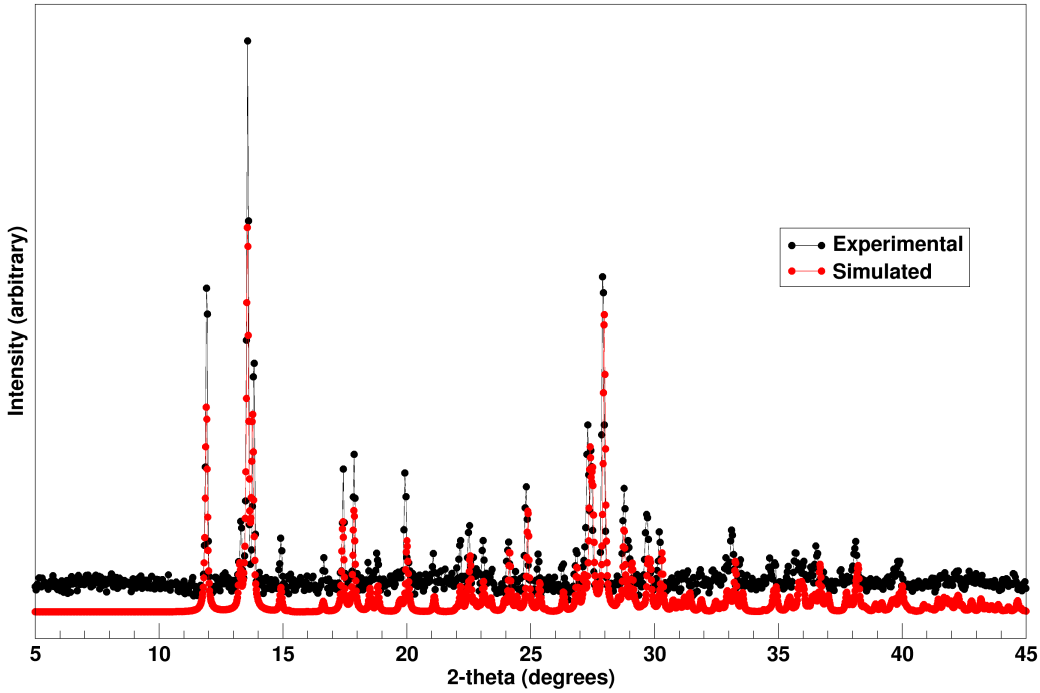

Figure 3.13: Experimental powder X-ray diffraction pattern of ortho-2(CL-20):HP (black) at 1.5406 Å, compared to a pattern simulated from the original CIF file (red, reference [18], ref-code AZAMIZ in the Cambridge Structural Database). For safety reasons, the sample was only very lightly ground prior to analysis, so a degree of preferred orientation may be present in the experimental pattern.

However, a key point to note here is that 2(CL-20):HP is isostructural with α-CL-20 - the hemihydrate of CL-20. This means that the powder diffraction patterns of both are almost identical in terms of peak positions (see Figure 3.14 for comparison). Hence, a chemical test was performed to determine whether hydrogen peroxide was present in the material.

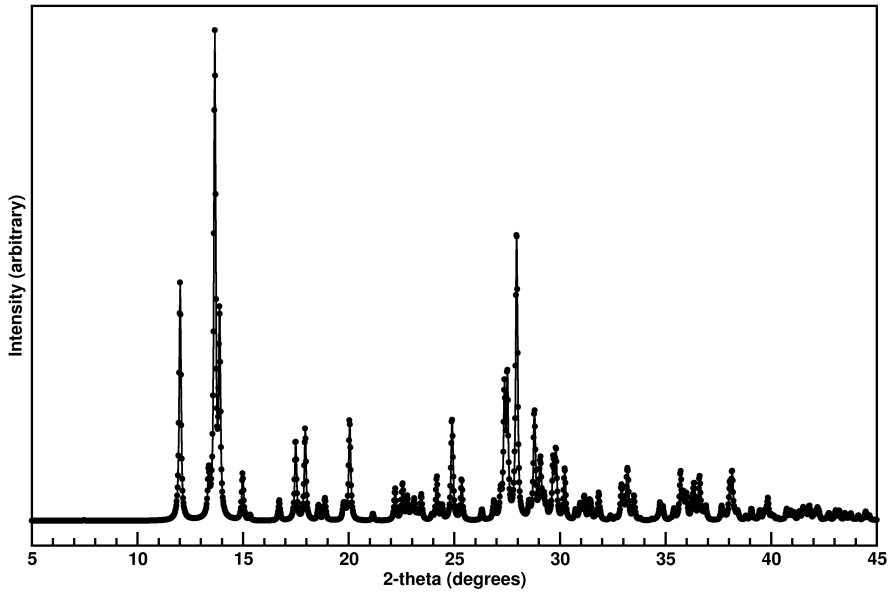

Figure 3.14: Simulated pattern of α-CL-20, using the CIF file PUBMII01 from the Cambridge Structural Database [20].

Test for presence of hydrogen peroxide

Materials used for this test were potassium iodide (KI, purchased from Fisher Scientific), glacial acetic acid (CH_3COOH, 99.9 %, purchased from Acros), the orthorhombic form of 2(CL-20):HP ($C_6H_6N_{12}O_{12}.{}^1/_2H_2O_2$, prepared using aforementioned method), and ϵ-CL-20 ($C_6H_6N_{12}O_{12}$), purchased from Event Horizon Ltd).

0.1 g of potassium iodide was dissolved in $\sim$ 1 ml of glacial acetic acid in three different vials. In the first vial, 30 mg of the solvate was added. In the second vial, 30 mg of CL-20 was added. The third vial had no additional solid added, acting as a control. A stopwatch was then used to measure how long until each vial discoloured with the production of iodine (example shown in Figure 3.15). These tests were repeated twice to ensure reproducibility, assuming the following ionic reaction equation:

$$2I^-_{aq} + 2H^+_{aq} + H_2O_2 \leftarrow I_{2(s)} + 2H_2O_{(l)} \tag{5}$$

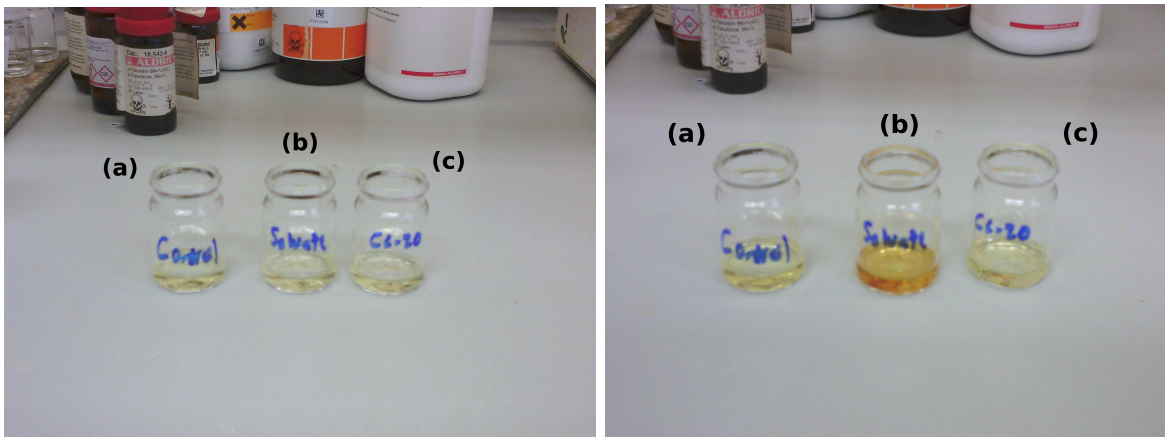

Figure 3.15: Example of the chemical test performed in this section. On the left, the three vials contain just KI and acetic acid. The image on the right was taken approximately one minute after adding a 30 mg sample of 2(CL-20):HP to vial (b), and a 30 mg sample of ϵ-CL-20 to vial (c). Vial (a) contained just KI and acetic acid in both images.

In all runs of this test, the vials containing the 2(CL-20):HP solvate were observed to become yellow-brown within 30 - 60 seconds after addition of the solvate. The vials containing just CL-20 took, on average, 20 minutes to discolour. The vials with no additional solid discoloured after an average time of 45 minutes, presumably due to oxidation by the air. These observations were taken as proof there was hydrogen peroxide present in the solvate material.

Following transport of the sample to the ISIS Neutron Source, the solvate was loaded into a Paris-Edinburgh pressure cell following the procedures outlined in Section 3.1.4. The maximum load applied to the sample in this study was 62 tonnes, giving a pressure of approximately 5.7 GPa.

3.1.4 High-pressure studies and common aspects

With all three systems, there were common experimental aspects in terms of the neutron studies. To avoid repetition, these will be detailed here.

A V3 Paris-Edinburgh (P-E) press was employed on the PEARL instrument in all three studies to generate the required high pressures. Single-toroidal anvils of zirconia-toughened alumina (ZTA) were used, with a gasket composed of a titanium zirconium alloy (TiZr). A 4:1 mixture of deuterated methanol and ethanol was utilised as a pressure transmitting medium (PTM), ensuring the sample experienced hydrostatic pressure within the P-E cell.

A small amount of lead was used as a pressure calibrant for the experiments involving 2(CL-20):HMX and CL-20:TNT. For the study of 2(CL-20):HP, sodium chloride (in a sample:salt mass ratio of 1:3) was used as the pressure calibrant. This was because a Bragg reflection from the solvate was found to partially obscure

a key reflection from lead in a pre-experiment simulation of the neutron patterns.

A d-spacing range of 1 - 4 Å was studied in each experiment. The region of less than 1 Å was excluded in each case, as the large amount of overlapping low-intensity Bragg reflections in this region inhibited suitable Rietveld refinement. The region beyond 4 Å is not normally accessible in the standard PEARL setup, on account of the sample geometry of the P-E cell.

In each case, the in-house Mantid software was utilised to normalise the collected data. The software also applied corrections for any attenuation of the neutron beam caused by the anvils and gasket [21, 22]. Rietveld refinement was used to refine lattice parameters and structural information for each system, using GSAS with EXPGUI [23, 24]. The known crystal structures reported by Bolton and Bennion (references [15], [17] and [18]) were used as a starting point for refinements, with an example fit shown in Figure 3.16. Additional scattering from the anvil components (zirconia and alumina) and the pressure calibrant (lead or sodium chloride), and the small amounts of contamininant ϵ-CL-20 and β-HMX-d_8 remaining in the 2(CL-20):HMX sample, were accounted for as additional refinement phases. Existing crystal structures from the Cambridge Structural Database were used to refine the ϵ-CL-20 and β-HMX impurity phases in this system [6, 10].

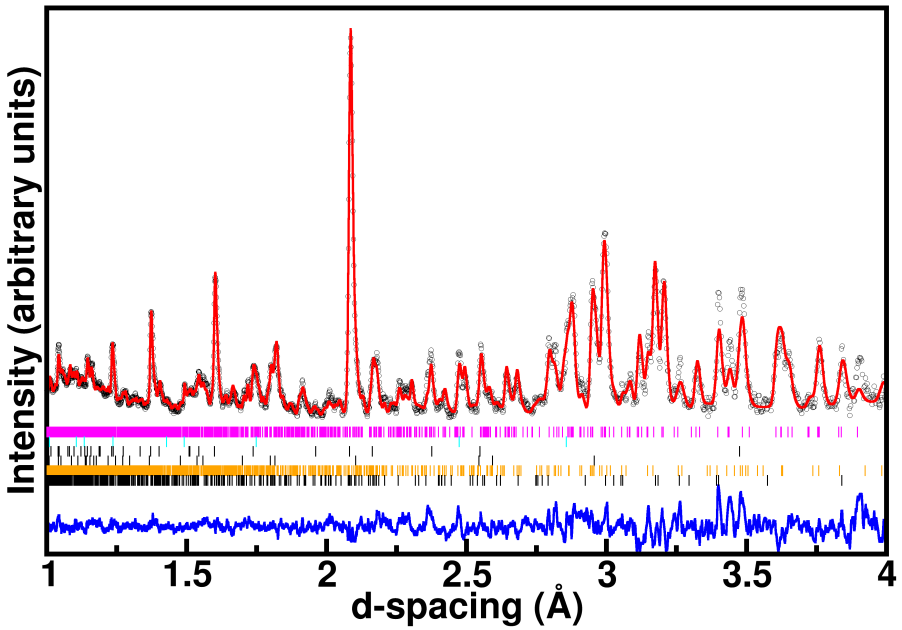

Figure 3.16: Example Rietveld refinement of 2(CL-20):HMX, from data recorded at 1.51 GPa. The Rietveld refinement model is denoted in red, with black circles representing experimental data points. The blue line denotes the difference between the model and experimental data. The tickmarks, from top to bottom, show Bragg reflections from the co-crystal; the lead pressure calibrant; the alumina and zirconia components of the anvils; and un-reacted ϵ-CL-20 and β-HMX, respectively.

To allow for more accurate Rietveld refinement of the atomic positions in each co-crystal, rigid bodies were applied to the CL-20, HMX and TNT moieties in each system. A Cartesian co-ordinate file was generated

for each moiety using the Mercury software package, and GSAS-II was used to map these co-ordinates to the co-crystal structure as a rigid body [25]. The lattice parameters from the initial GSAS/EXPGUI Rietveld refinements were used as a starting point for this subsequent GSAS-II analysis, in which the position and rotation angles of each rigid body unit were refined.

After application of the rigid bodies, refinements proceeded by first refining the background of the pattern using a shifted Chebyschev function with 10-12 terms in the background function. The lattice parameters were then allowed to refine with mild damping applied, along with the phase fractions of each component. Following this, the rigid body origins and torsion angles were allowed to refine, along with the rigid body thermal displacement. Finally, where appropriate, the sigma-1 and gamma-1 profile functions of the pattern were allowed to refine until optimal R-factors were achieved.

Equations of state were determined from the experimental data using EOSFit7 [26]. In each case, a third-order Birch-Murnaghan equation of state was fitted to the experimental volume data. This allowed prediction of unit-cell volumes as a function of pressure beyond the ranges studied experimentally. The experimental data-sets were also used with the program PASCal to determine how the compressibility of each material related to the principal axes of compression [27].

3.2 Results and Discussion

3.2.1 2(CL-20):HMX

The a, b and c lattice parameters were found to decrease at a similar rate relative to each other as a function of pressure, for the majority of the studied pressure range. A normalised plot of the lattice parameters as a function of pressure is shown below in Figure 3.17, with un-normalised values given in Table 3.4. The progression of the diffraction patterns with increasing pressure is displayed in Figure 3.18. The accompanying pressure-volume curve, with an overlaid equation of state derived from the experimental data, follows in Figure 3.19.

The lattice parameters have been normalised in these plots, for ease of presentation, to the values obtained at the first pressure point (0.02 GPa). Owing to time constraints, it was not possible to acquire a room-temperature ambient-pressure crystal structure of this material for indexing.

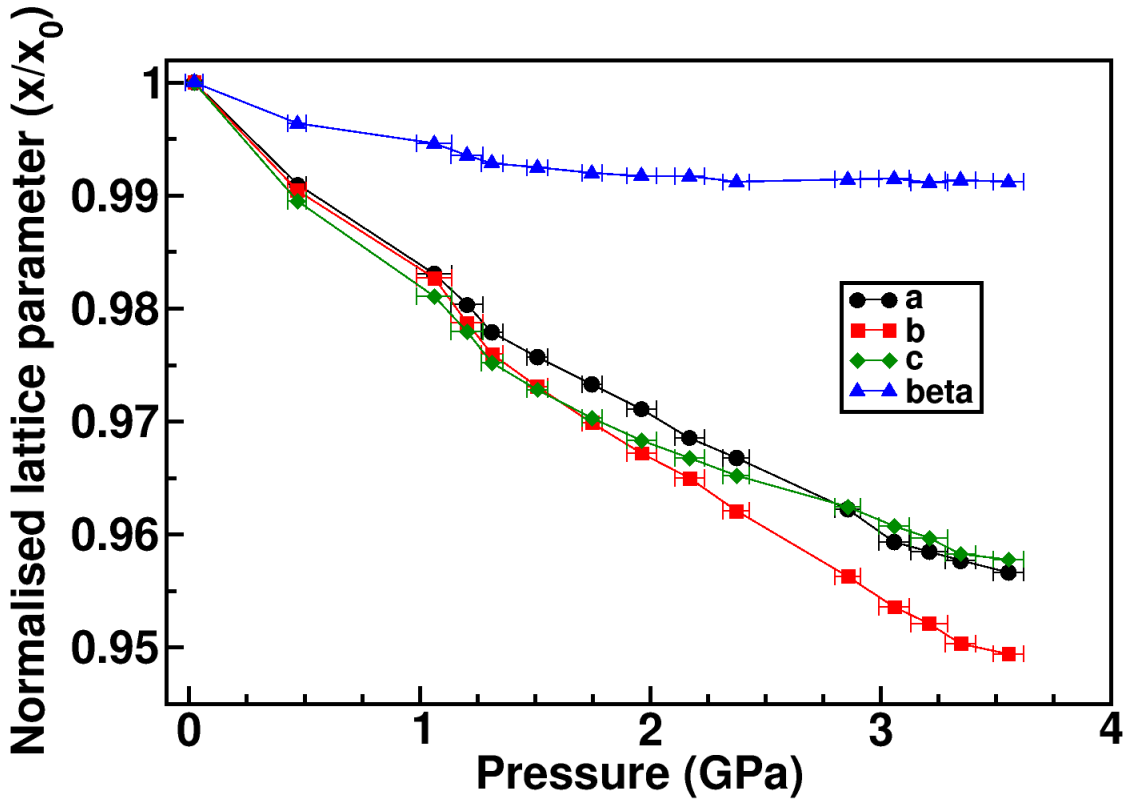

Figure 3.17: Variation of the normalised lattice parameters of 2(CL-20):HMX as a function of pressure at 298 K, normalised to unit cell parameters determined at the first pressure point, 0.02 GPa. Error bars on the y-axis, as calculated from the Rietveld refinement, are too small to be displayed on this scale.

Table 3.4: Lattice parameters for 2(CL-20):HMX at each pressure point during this experiment, together with associated refinement factors. Rietveld refinement took place as described in Section 3.1.4

Pressure (GPa)	a (Å)	b (Å)	c (Å)	β (°)	V (Å^3)	R_p (%)	R_{wp} (%)	GoF
0.02(4)	16.4607(55)	9.9712(11)	12.2167(30)	99.799(15)	1975.9(3)	3.35	3.24	1.38
0.47(4)	16.3117(61)	9.8758(12)	12.0883(32)	99.435(17)	1921.0(4)	3.40	3.40	1.42
1.06(8)	16.1818(70)	9.7983(16)	11.9850(42)	99.257(19)	1876.2(5)	3.30	3.34	1.88
1.21(7)	16.1367(51)	9.7589(14)	11.9470(28)	99.155(14)	1857.4(4)	2.44	2.53	1.20
1.32(5)	16.0969(40)	9.7312(11)	11.9137(21)	99.085(11)	1842.8(3)	2.10	2.19	1.03
1.51(5)	16.0599(44)	9.7028(13)	11.8844(22)	99.044(12)	1828.9(2)	2.28	2.16	1.18
1.75(4)	16.0206(45)	9.6710(12)	11.8540(22)	98.998(12)	1814.0(3)	2.23	2.15	1.04
1.96(6)	15.9850(60)	9.6438(15)	11.8292(30)	98.973(17)	1801.2(4)	2.48	2.46	1.22
2.17(6)	15.9430(56)	9.6216(14)	11.8100(28)	98.968(15)	1789.5(4)	2.45	2.39	1.15
2.37(6)	15.9134(55)	9.5928(14)	11.7916(29)	98.917(16)	1778.3(4)	2.45	2.47	1.18
2.86(6)	15.8390(49)	9.5353(13)	11.7579(26)	98.941(14)	1754.2(4)	2.32	2.36	1.11
3.06(7)	15.7906(51)	9.5082(13)	11.7369(25)	98.946(14)	1740.7(4)	2.29	2.32	1.06
3.21(8)	15.7771(52)	9.4935(15)	11.7239(24)	98.914(14)	1734.8(4)	2.29	2.34	1.05
3.35(7)	15.7635(57)	9.4758(15)	11.7069(27)	98.936(16)	1727.5(4)	2.53	2.61	0.99
3.56(7)	15.7467(52)	9.4668(15)	11.7009(23)	98.919(15)	1723.2(4)	2.10	2.28	1.48

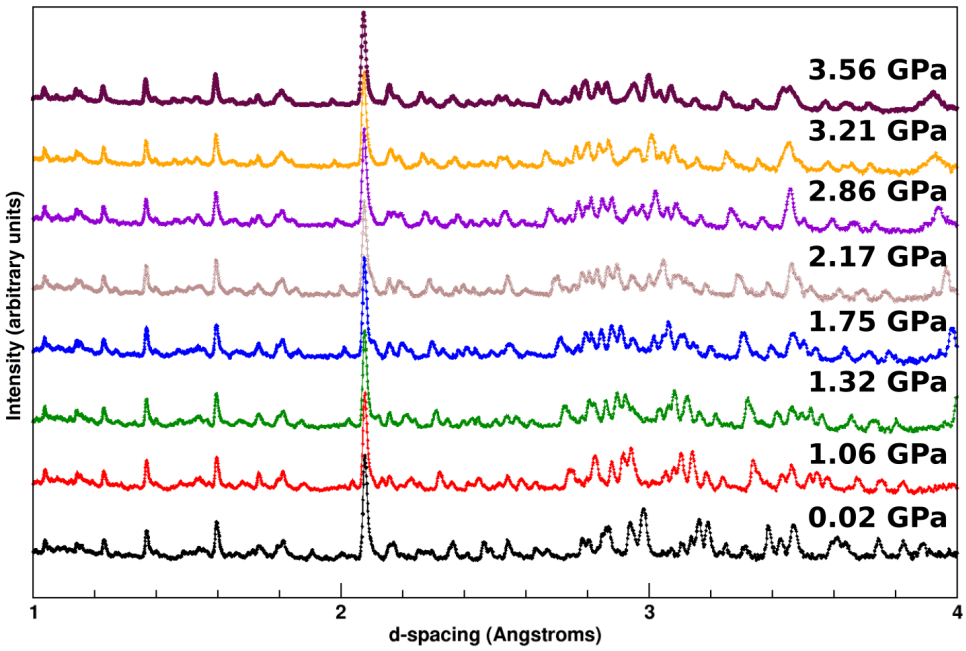

Figure 3.18: Progression plot of selected 2(CL-20):HMX diffraction patterns as a function of pressure. The movement of peaks as a result of the pressure increase can be clearly seen.

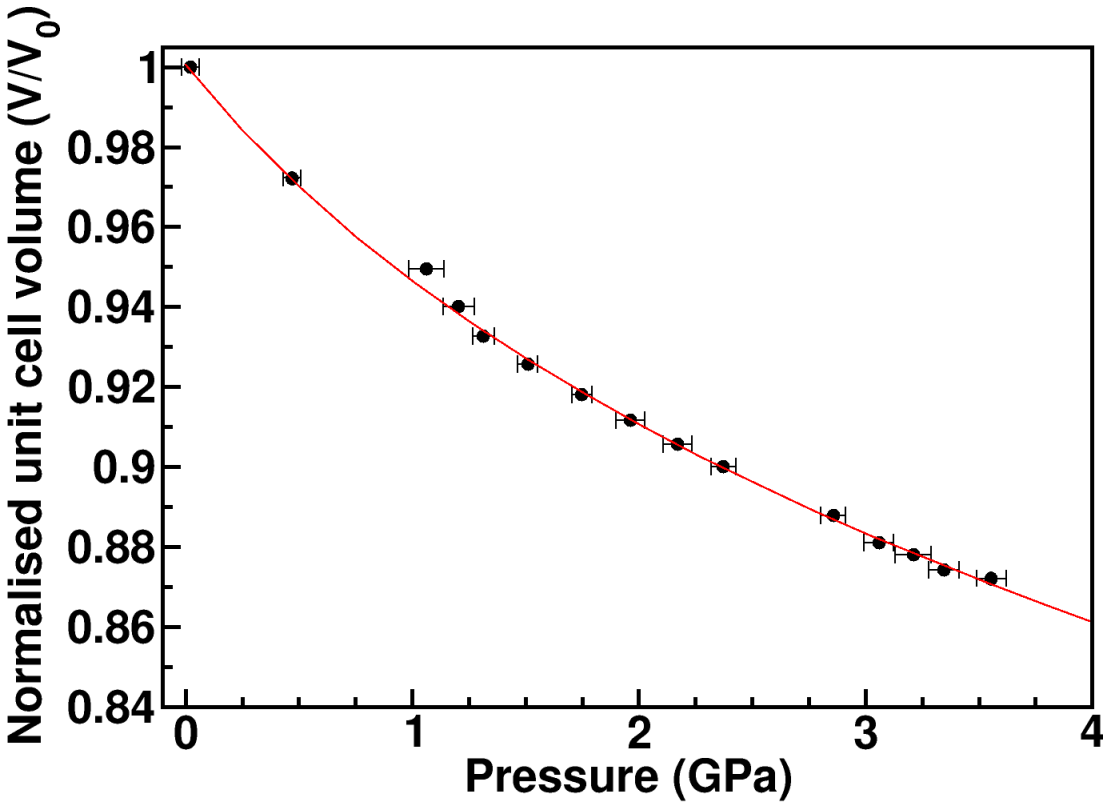

Figure 3.19: Third-order Birch-Murnaghan equation of state for 2(CL-20):HMX, fitted to normalised experimental data. Error bars on the y-axis are too small to be displayed on this scale.

The compression behaviour observed over the entire pressure range is unusually isotropic in nature for a layered structure, with very similar decreases in each axis. Previous studies of energetic materials under

pressure have tended to display greatly increased compressibility perpendicular to the inter-layer spacing [28]. In this particular case, one might have expected increased relative compressibility along the *a*-axis, as this axis represents the inter-layer spacing between the HMX and CL-20 bi-layers (as shown in Figure 3.2, but this is clearly not observed.

A change in slope of the *c*-axis is observed beyond 2.1 GPa. Given that the steric environment is similar along the *b* and *c* axes, and they are of comparable lengths, the reason for a difference in compressibility is not immediately apparent. However, when one considers the void space present along each axis, things become clearer. As can be seen in the side-by-side plots in Figure 3.20, for most of the voids shown, their longest diameter is along the *b*-axis. This means there is more scope for these voids to compress along that axis, compared to the *c*-axis, which has comparatively smaller void diameters. As these voids compress, there is less scope for compression of the smaller voids along the *c*-axis than for compression of the voids along the *b*-axis.

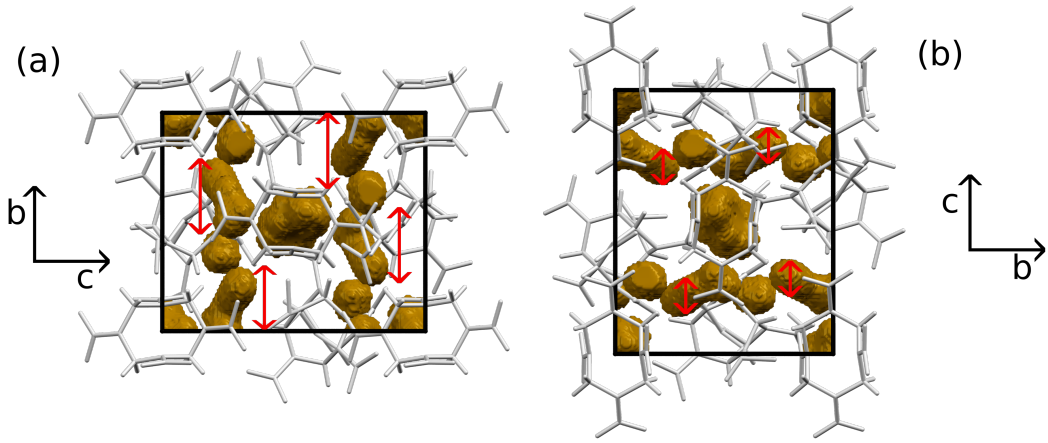

Figure 3.20: A view of 2(CL-20):HMX at 0.02 GPa along the *a*-axis from two angles, with void spaces highlighted in yellow, and void diameters indicated with red arrows. In (a), the view is with the *b*-axis running vertically; and in (b), the *c*-axis is running vertically. The differences in void diameter between the *b*- and *c*-axes are illustrated. Voids were calculated in Mercury using a probe size of 0.8 Å, as this showed the effects most clearly, and a grid spacing of 0.3 Å. Atoms and bonds have been shown in grey to enhance clarity of the rest of the image.

The program PASCal was used to compare this compressibility behaviour relative to the principal axes. This allows for direct comparison of compressibilities between materials of different crystallographic symmetries. The directions of the principal axes in the co-crystal were set by the software as shown in Table 3.5, along with the calculated compressibility values of each principal axis.

Table 3.5: Table showing how much each crystallographic axis (on a scale from -1 to 1) contributes to the three principal stress/strain axes, as calculated by PASCal, with associated compressibility values.

Principal axis	a component	b component	c component	Compressibility (TPa^{-1})
X_1	-0.4762	0.0000	0.8793	10.418(377)
X_2	0.0000	-1.000	0.0000	12.316(342)
X_3	0.6805	0.0000	0.7327	8.344(214)

The compressibilities were found to be very similar along all three principal axes. The bulk modulus (B_0) of the co-crystal was determined from the aforementioned equation of state to be 14.1(8) GPa, with pressure derivative $B' = 9.1(9)$. The initial volume (V_0) of the room-temperature equation of state was not fixed during EOS calculation, as the original co-crystal data were collected at 95 K. The EOS determined the initial volume at 298 K to be 1977.04(2.75) Å^3, very close to the unit-cell volume at 0.02 GPa - 1975.9(3) Å^3. The calculated bulk modulus lies between that of the two co-formers, with $B_0 = 9.5(2)$ GPa for ϵ-CL-20 [29], and 21.0(2) GPa for β-HMX [30].

The primary intermolecular interactions in the co-crystal comprise a series of weak hydrogen bonding interactions between different moieties. Two contacts in particular have been illustrated in Figure 3.21 below.

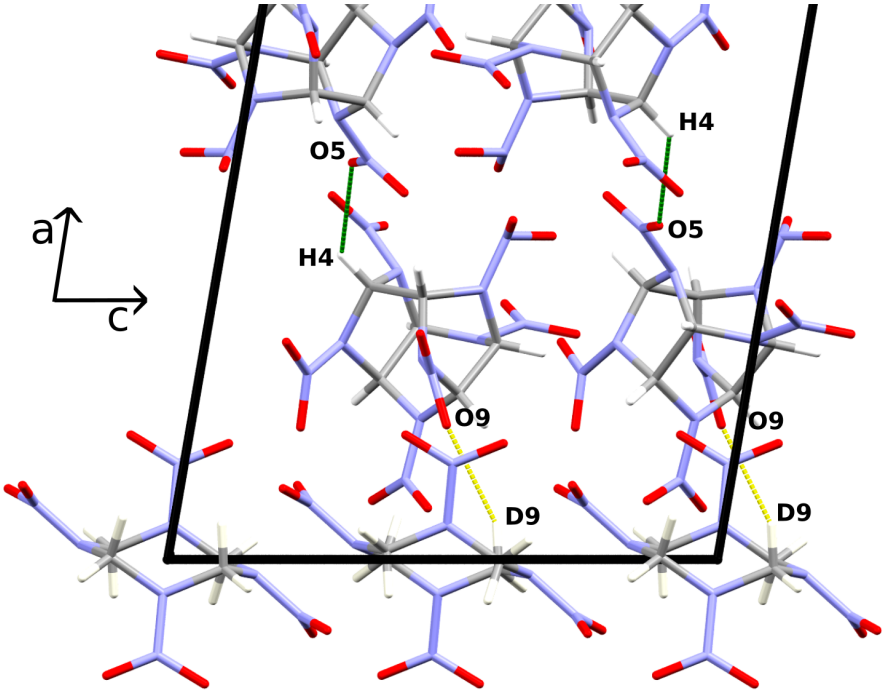

Figure 3.21: The most and least compressible C-H...O interactions present in 2(CL-20):HMX, as viewed along the *b*-axis (cf. Figure 3.2. The most-compressible contact, O9...D9, is highlighted in yellow; and the least-compressible contact, O5...H4, is highlighted in green. As the HMX molecules on the upper and lower faces are symmetrically aligned, some atoms appear eclipsed in this view. Since the intermolecular interactions are mirrored on the opposite side of the unit cell, the upper half of the cell has been omitted for clarity.

The most compressible hydrogen bonding interaction is the O9...D9 contact, between adjacent CL-20 and HMX moieties. This decreases by 0.327 Å over the studied pressure range from 2.517(44) to 2.190(35) Å. This bond is representative of the spacing between the layers of CL-20 and HMX molecules. Interestingly, the least-compressible hydrogen bonding interaction proved to be the O5...H4 contact between the two 'halves' of the CL-20 bi-layer, decreasing by only 0.04 Å over the studied pressure range (from 2.527(40) to 2.487(32) Å). Despite this contact also being representative of inter-layer spacing (between two CL-20 mono-layers), the lack of compression here implies the steric bulk of the CL-20 molecules is hindering compression within the bi-layer itself thereby making the bi-layer act as a rigid 'block' between the 'softer' HMX layers.

No phase transitions were observed over the course of the experiment, as demonstrated by a lack of discontinuities in the pressure-volume curve, and a lack of noticeable changes in the diffraction patterns beyond the normal peak-shifting effects of hydrostatic compression. Although the inclusion of impurity phases of ϵ-CL-20 and β-HMX was not intended, their subsequent refinement actually proved to be helpful. As the phase fractions of these two impurities (Table 3.6, determined from the Rietveld refinements) do not fluctuate by any meaningful amount outside of experimental error, this demonstrates that no phase separation or solvent-mediated transformations have occurred over the studied pressure range. This indicates that

the co-crystal remains the thermodynamically favourable phase over this pressure range, assuming that the kinetic barriers for interconversion are low. This assumption is reasonably valid as all three phases have some limited solubility in the deuterated methanol/ethanol pressure-transmitting medium.

Table 3.6: Phase fractions for impurity CL-20 and HMX phases, as expressed in weight percentages calculated by GSAS-II

Pressure (GPa)	CL-20 PF (wt%)	HMX PF (wt%)
0.02(4)	2.8(6)	2.2(4)
0.47(4)	3.1(6)	2.1(5)
1.06(8)	2.9(5)	1.9(4)
1.21(7)	3.3(4)	1.9(3)
1.32(5)	3.4(5)	2.3(4)
1.51(5)	2.9(4)	2.1(4)
1.75(4)	3.3(5)	1.9(3)
1.96(6)	3.4(6)	1.7(4)
2.17(6)	3.4(6)	1.9(4)
2.37(6)	3.3(5)	1.8(4)
2.86(6)	3.2(4)	1.9(3)
3.06(7)	2.9(5)	2.2(4)
3.21(8)	3.0(4)	2.2(3)
3.35(7)	3.3(5)	2.0(4)
3.56(7)	3.0(4)	2.1(3)

3.2.2 CL-20:TNT

In CL-20:TNT, the *b*-axis lattice parameter was found to decrease at a substantially greater rate over the studied pressure range compared to the *a*- and *c*-axes. This can be seen clearly in Figure 3.22, where the normalised lattice parameters have been plotted as a function of pressure. Absolute values are given in Table 3.7, and a series of diffraction patterns are shown in Figure 3.23. The pressure-volume curve, with an overlaid equation of state derived from the experimental data, is also displayed in Figure 3.24.

As with the previous system, the lattice parameters have been normalised in these plots for ease of presentation to the values obtained at the first pressure point (0.16 GPa). Owing to time constraints, it was not possible to acquire a room-temperature ambient-pressure crystal structure of this material for indexing.

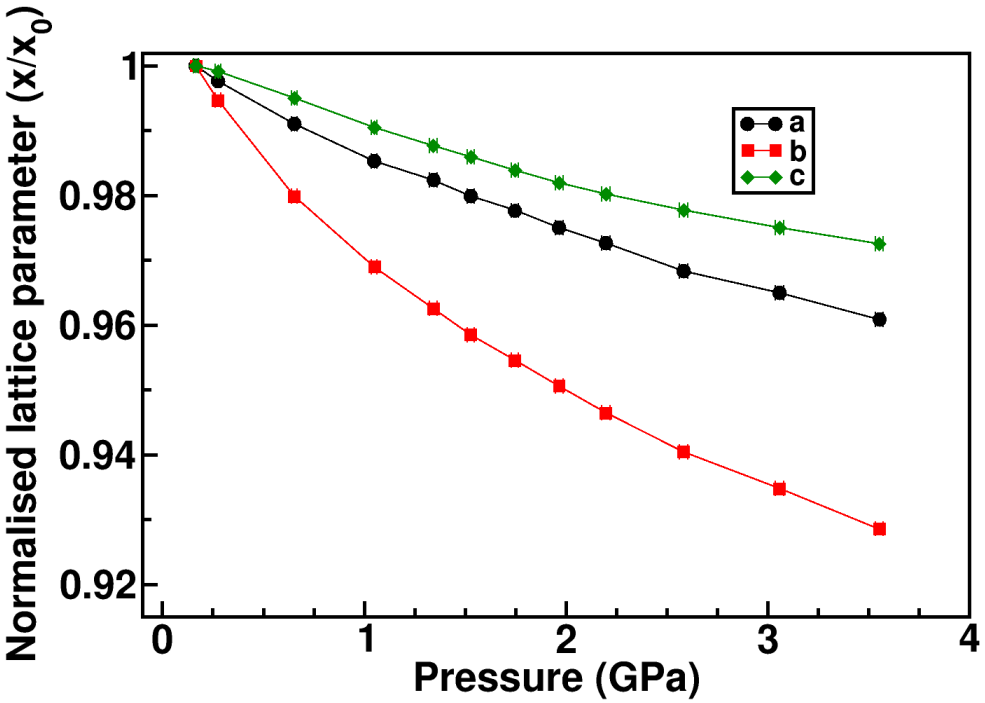

Figure 3.22: Variation of the normalised lattice parameters of CL-20:TNT as a function of pressure, normalised to the values obtained at the first pressure point of the experiment. Error bars on the y-axis, as calculated from the Rietveld refinement, are too small to be displayed on this scale.

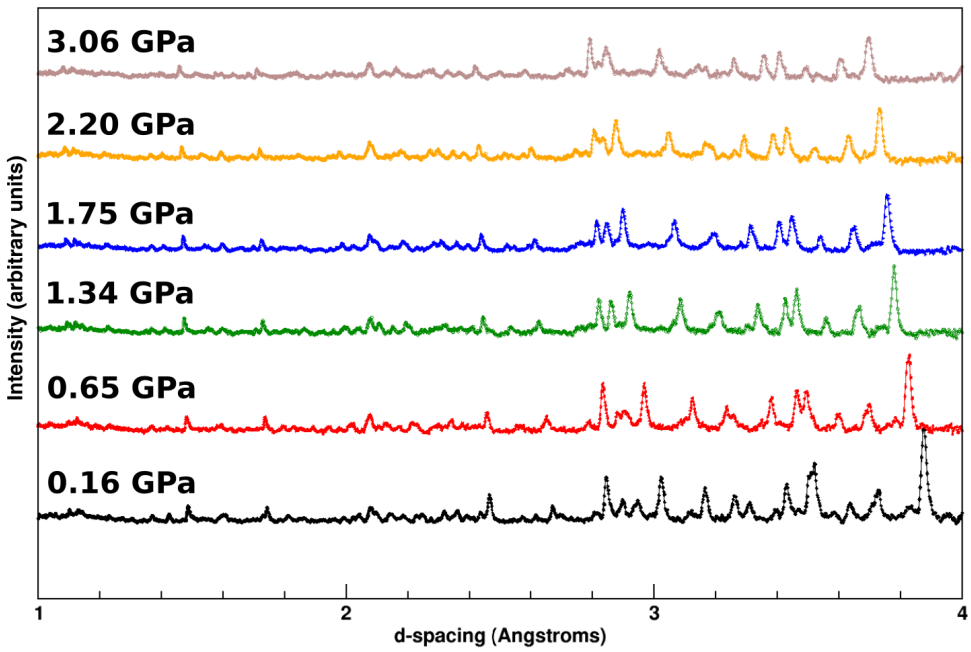

Figure 3.23: Progression plot of selected CL-20:TNT diffraction patterns as a function of pressure.

Table 3.7: Lattice parameters for CL-20:TNT at each pressure point during this experiment, along with associated refinement factors.

Pressure (GPa)	a (Å)	b (Å)	c (Å)	V (Å^3)	R_p (%)	R_{wp} (%)	GoF
0.16(1)	9.6846(9)	19.5811(20)	24.6924(25)	4682.6(5)	2.31	2.15	0.86
0.28(1)	9.6621(1)	19.4765(22)	24.6705(30)	4642.6(6)	2.59	2.39	0.77
0.65(2)	9.5975(12)	19.1865(24)	24.5686(28)	4524.1(7)	2.75	2.55	0.80
1.05(1)	9.5423(8)	18.9737(16)	24.4565(24)	4427.9(5)	2.32	2.18	0.93
1.34(2)	9.5141(11)	18.8479(22)	24.3875(29)	4373.2(6)	2.88	2.69	0.80
1.53(2)	9.4900(11)	18.7685(24)	24.3454(27)	4336.2(6)	2.75	2.58	0.76
1.75(2)	9.4684(12)	18.6911(26)	24.2938(23)	4299.4(5)	2.42	2.32	0.97
1.97(2)	9.4425(13)	18.6134(25)	24.2464(27)	4261.5(6)	2.62	2.50	0.74
2.20(2)	9.4199(11)	18.5323(21)	24.2038(26)	4225.3(6)	2.65	2.48	0.72
2.58(2)	9.3773(14)	18.4143(27)	24.1424(30)	4168.8(7)	2.85	2.92	1.14
3.06(2)	9.3452(12)	18.3035(24)	24.0748(29)	4118.0(7)	2.85	2.75	0.74
3.55(2)	9.3056(11)	18.1821(22)	24.0131(26)	4062.9(6)	2.64	2.50	0.73

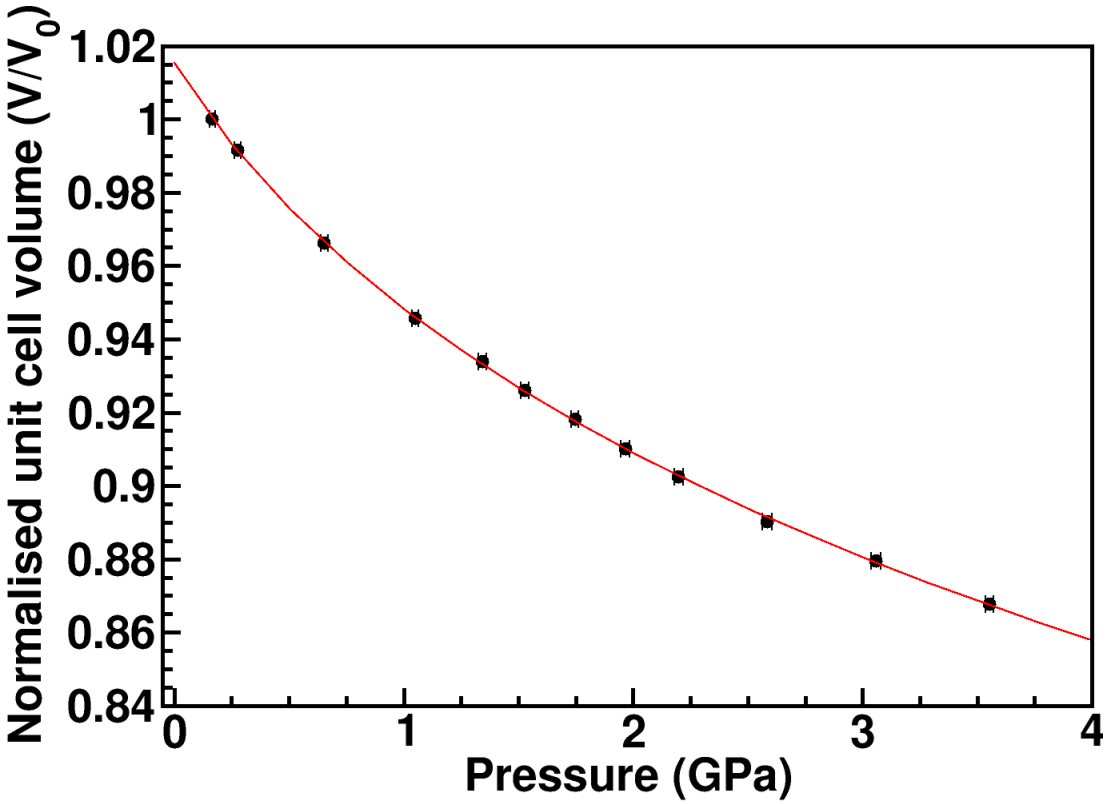

Figure 3.24: Calculated third-order Birch-Murnaghan equation of state for CL-20:TNT, fitted to normalised experimental data, as a function of pressure. Error bars on the y-axis are too small to be displayed on this scale.

The bulk modulus (B_0) of the co-crystal was determined from the equation of state to be 10.1(5) GPa, with pressure derivative $B' = 11.6(7)$. The initial volume (V_0) of the room-temperature equation of state was determined to be 4753.9(6.3) Å^3. The calculated bulk modulus is comparable to that of the two co-formers, with $B_0 = 9.5(2)$ GPa for pure ϵ-CL-20 [29], and $B_0 = 8.52$ GPa for the orthorhombic form of TNT [31].

The greater compression along the *b*-axis can be easily rationalised by considering the layering present in the structure of CL-20:TNT. As shown in Figure 3.3, these alternating layers of CL-20 and TNT are parallel to the *c*-axis, and perpendicular to the *b*-axis. Hence this makes the *b*-axis the main component of the inter-layer spacing. With increasing pressure, these layers move closer together as the *b*-axis is preferentially compressed.

Principal axis compressibilities were also calculated for this system using PASCal [27]. Since this system possesses orthorhombic symmetry, the principal axes map directly onto the crystallographic axes. Compressibility values are given for each axis in Table 3.8 below.

As with the 2(CL-20):HMX system, the main intermolecular interactions are a series of weak C-H...O hydrogen bonding interactions between the different moieties. The most and least compressible contacts are illustrated in Figure 3.25.

Table 3.8: Principal axis compressibilities for CL-20:TNT, as calculated by PASCal.

Principal Axis	Crystallographic Axis	Compressibility (TPa^{-1})
X_1	b	16.98(95)
X_2	a	10.39(18)
X_3	c	7.69(27)

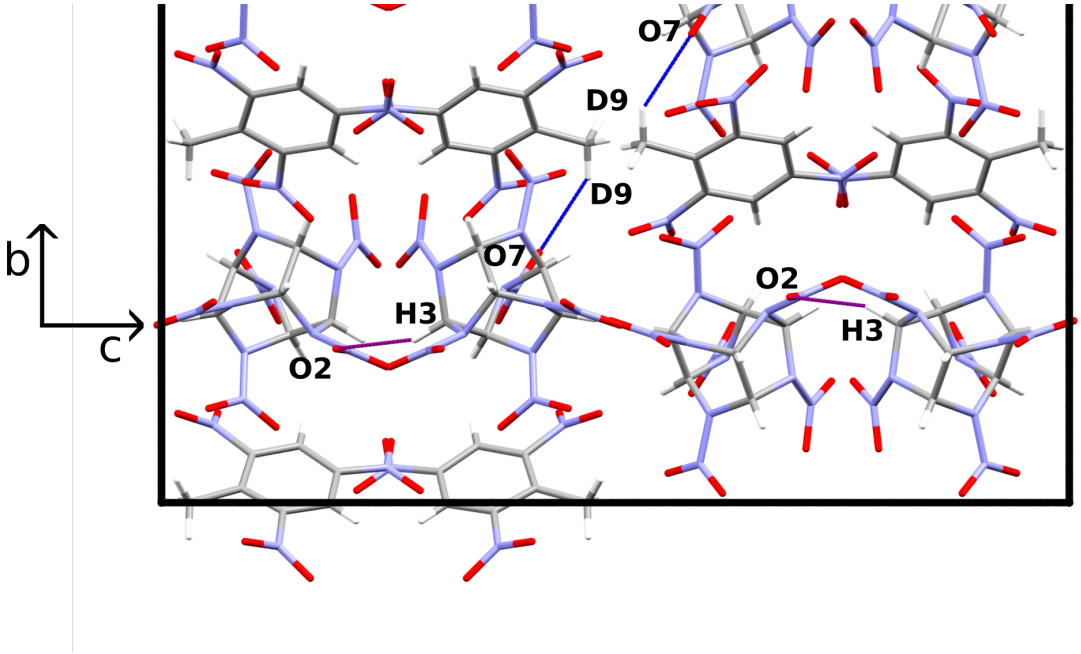

Figure 3.25: The most and least compressible C-H...O interactions present in CL-20:TNT, as viewed along the a-axis (cf. Figure 3.3. The most compressible contact, O7...D9, is highlighted in blue; and the least compressible contact, O2...H3, is highlighted in purple. Since the intermolecular interactions are mirrored on the opposite side of the unit cell, the upper half of the cell has been omitted for clarity.

The most compressible hydrogen bonding interaction is the O7...D9 contact between the CL-20 and TNT layers. This decreases by 0.603 Å over the studied pressure range, from 2.649(21) to 2.046(17) Å. The least-compressible H-bond, however, was the O2...H3 contact along the CL-20 layers, with a decrease of only 0.096 Å over the studied pressure range from 2.479(19) to 2.383(19). This is a similar to the behaviour seen in the previous system, where these sterically bulky CL-20 molecules strongly resist being compressed together.

It was mentioned earlier in this chapter that although the experiment reached a maximum pressure of 4.1 GPa, high-quality diffraction data were obtained only up to 3.5 GPa. Approximately thirty minutes into the data collection at 4.1 GPa, a brief spike was registered in the vacuum gauge of the instrument tank. The sensors controlling the applied load also began to fluctuate wildly. The cell was deliberately decompressed to ambient pressure for diagnostics, at which point no sample was observed in the neutron diffraction pattern.

Upon removing the cell from the instrument, it was discovered that the cell had “blown out” (as seen in

Figure 3.26). This indicates that some sort of event within the cell had caused failure of the gasket.

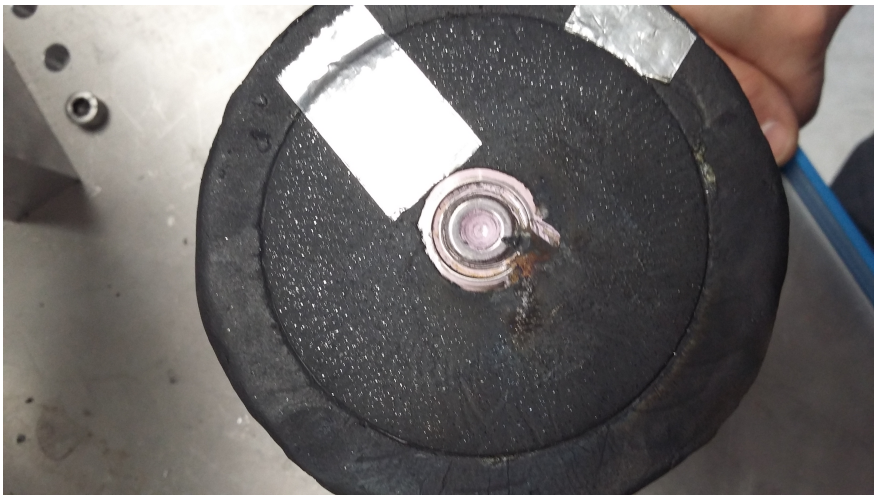

Figure 3.26: One of the damaged anvils, after disassembly of the P-E cell following the event at 4.1 GPa.

It is unlikely that this event was caused by a simple structural failure during pressure equilibration - normally such events would occur within minutes of reaching the new pressure, or during compression. Instead, because the event happened over half an hour after the pressure increase, it is presumed to be related to the sample. Insufficient data statistics exist at 4.1 GPa to allow meaningful refinement of the neutron data; but the diffraction patterns collected at 3.5 GPa and 4.1 GPa can be visually compared, as shown in Figure 3.27. Comparisons of these two patterns suggest that up to this point, no phase transition had occurred. However, it is possible that a phase transition occurred very suddenly after this period of time at 4.1 GPa. If such a phase transition resulted in a sudden, substantial decrease in volume, then this might cause the gasket to fail.

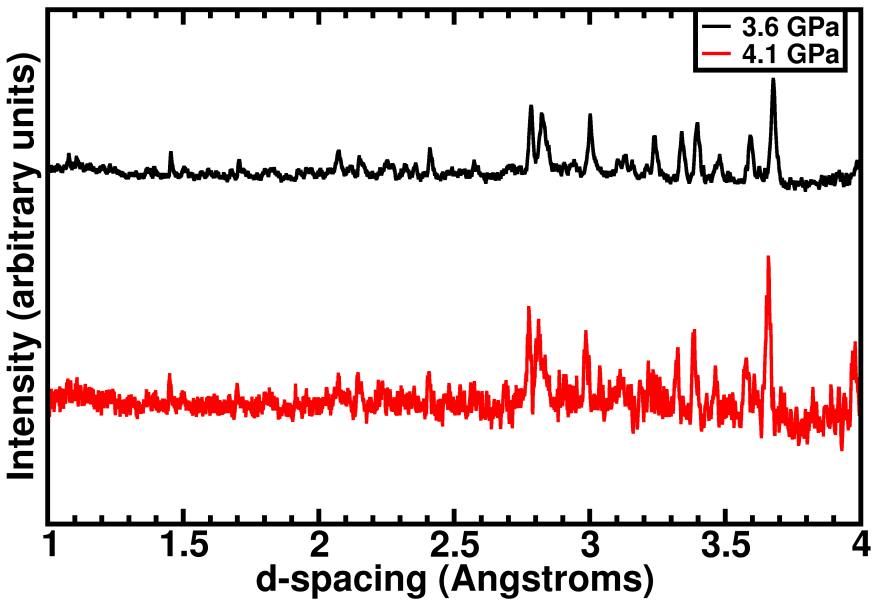

Figure 3.27: Diffraction patterns of CL-20:TNT taken at 3.6 and 4.1 GPa. The 4.1 GPa collection is only from thirty minutes' worth of neutrons, so has significantly poorer data resolution. No obvious differences between the two patterns can be seen that cannot be accounted for by noise.

An alternative and more likely explanation is that a violent chemical reaction occurred, causing a dramatic change in the sample volume within the cell. This then led to the structural failure mentioned previously, and loss of the sample. The most likely reactions to have taken place that would cause such a dramatic volume change are either initiation of the energetic sample, possibly by frictional contact between particles of the co-crystal, or a reaction with the methanol-ethanol pressure-transmitting medium.

3.2.3 2(CL-20):HP

For the orthorhombic form of 2(CL-20):HP, the a, b and c-axes were found to decrease at a similar rate relative to each other over the pressure range studied.

A normalised plot of these lattice parameters as a function of pressure is shown in Figure 3.28, with absolute values given in Table 3.10, and a selection of diffraction patterns in Figure 3.29. The pressure-volume curve, with overlaid equation of state derived from the experimental data, is also displayed in Figure 3.30.

Lattice parameters for this system have been normalised to values obtained from powder X-ray data at ambient temperature and pressure. The pattern was indexed using DICVOL06, and treated with a Pawley refinement using DASH [32]. The resulting lattice parameters and refinement factors achieved are shown in Table 3.9. This indexing process was necessary as the original structure in the CSD was collected at 95 K. Normalisation to the x-ray data was considered preferable as this was high-quality diffraction data collected at both ambient temperature and pressure, which was not available for the preceding two CL-20 systems.

Table 3.9: Lattice parameters for the orthorhombic form of 2(CL-20):HP at 298 K, as derived from an indexing and Pawley refinement of X-ray diffraction data recorded at ambient temperature and pressure. These parameters were used for normalisation of the neutron diffraction data discussed in this section.

Parameter	Value
a	9.558(8) Å
b	13.197(11) Å
c	23.574(14) Å
V	2973.62(12) Å^3
χ^2	1.41

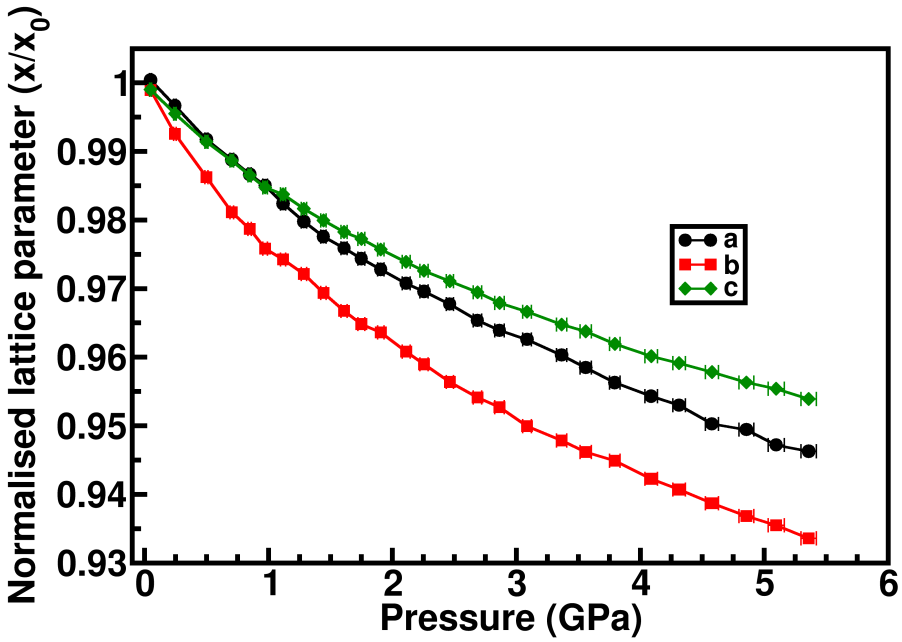

Figure 3.28: Evolution of the lattice parameters of 2(CL-20):HP as a function of pressure, as normalised to the indexed values obtained at 209 K and ambient pressure.

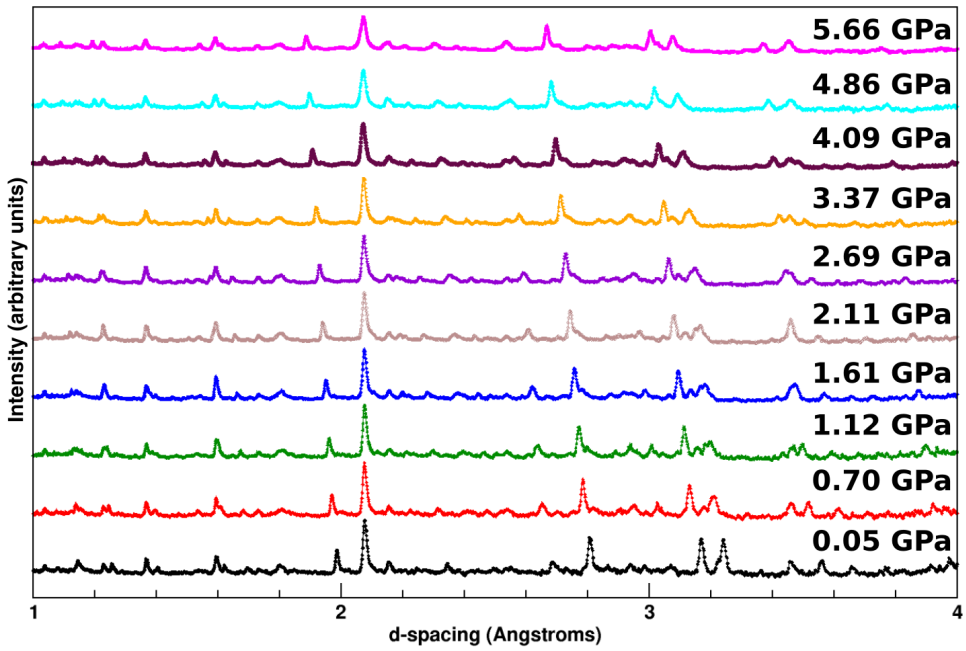

Figure 3.29: Progression plot of selected 2(CL-20):HP diffraction patterns as a function of pressure.

Table 3.10: Lattice parameters for the orthorhombic form of CL-20:HP at each pressure point during this experiment, along with associated refinement factors.
$*$ - data collection for this pressure point was markedly shorter than others, resulting in higher R-factors.

Pressure (GPa)	a (Å)	b (Å)	c (Å)	V (Å^3)	R_p (%)	R_{wp} (%)	GoF
0.05(1)	9.5620(19)	13.1831(27)	23.5505(36)	2968.7(5)	2.70	2.73	1.24
0.25(1)	9.5262(18)	13.0986(27)	23.4671(34)	2928.2(6)	3.10	3.05	0.88
0.50(1)	9.4792(18)	13.0153(28)	23.3707(33)	2883.3(6)	2.97	3.02	0.95
0.70(1)	9.4511(19)	12.9476(29)	23.3058(30)	2851.9(6)	2.73	2.78	0.93
0.85(1)	9.4307(14)	12.9157(23)	23.2553(23)	2832.6(4)	1.93	1.99	0.88
0.97(2)	9.4150(34)	12.8778(48)	23.2137(56)	2814.5(9)	4.96	4.77	0.73$*$
1.06(1)	9.4017(18)	12.8753(26)	23.2028(32)	2808.7(5)	3.61	3.11	0.78
1.12(2)	9.3900(18)	12.8569(26)	23.1903(27)	2799.7(5)	2.60	2.53	0.81
1.29(2)	9.3649(19)	12.8289(26)	23.1405(28)	2780.1(6)	2.67	2.64	0.85
1.44(2)	9.3438(20)	12.7925(30)	23.1002(29)	2761.2(6)	2.87	2.78	1.22
1.61(2)	9.3277(13)	12.7579(20)	23.0609(20)	2744.3(4)	1.92	2.00	0.91
1.75(2)	9.3132(17)	12.7326(24)	23.0371(24)	2731.8(5)	2.49	2.45	0.87
1.91(3)	9.2981(21)	12.7166(30)	23.0004(31)	2719.6(6)	2.93	2.89	1.26
2.11(3)	9.2787(16)	12.6798(21)	22.9581(24)	2701.1(4)	2.03	2.11	0.85
2.26(3)	9.2676(22)	12.6553(29)	22.9272(32)	2689.0(6)	2.83	2.86	0.88
2.46(3)	9.2498(22)	12.6213(35)	22.8915(37)	2672.5(7)	2.95	2.95	1.17
2.69(3)	9.2270(14)	12.5914(22)	22.8535(22)	2655.1(4)	1.95	1.99	0.81
2.86(3)	9.2130(18)	12.5728(24)	22.8167(30)	2643.0(5)	2.87	2.77	0.86
3.09(4)	9.2005(20)	12.5362(30)	22.7865(34)	2628.2(7)	2.97	2.97	1.22
3.37(3)	9.1787(15)	12.5088(20)	22.7424(25)	2611.2(5)	2.12	2.12	0.82
3.56(4)	9.1612(21)	12.4864(30)	22.7188(35)	2598.8(7)	2.95	2.86	0.88
3.80(5)	9.1404(26)	12.4698(35)	22.6760(43)	2584.6(8)	3.07	3.10	0.88
4.09(4)	9.1215(17)	12.4349(22)	22.6336(26)	2567.2(5)	2.02	2.15	1.20
4.31(5)	9.1088(29)	12.4142(33)	22.6097(46)	2556.7(8)	3.19	3.09	0.87
4.58(5)	9.0826(22)	12.3879(29)	22.5792(34)	2540.5(7)	2.90	2.88	0.80
4.86(5)	9.0749(21)	12.3633(29)	22.5435(35)	2529.3(7)	2.62	2.67	1.04
5.10(6)	9.0534(27)	12.3455(35)	22.5221(44)	2517.3(8)	3.00	2.98	0.81
5.36(6)	9.0448(24)	12.3205(37)	22.4865(40)	2505.8(8)	2.92	2.95	0.80
5.66(6)	9.0219(23)	12.3047(33)	22.4523(39)	2492.5(7)	2.33	2.48	1.32

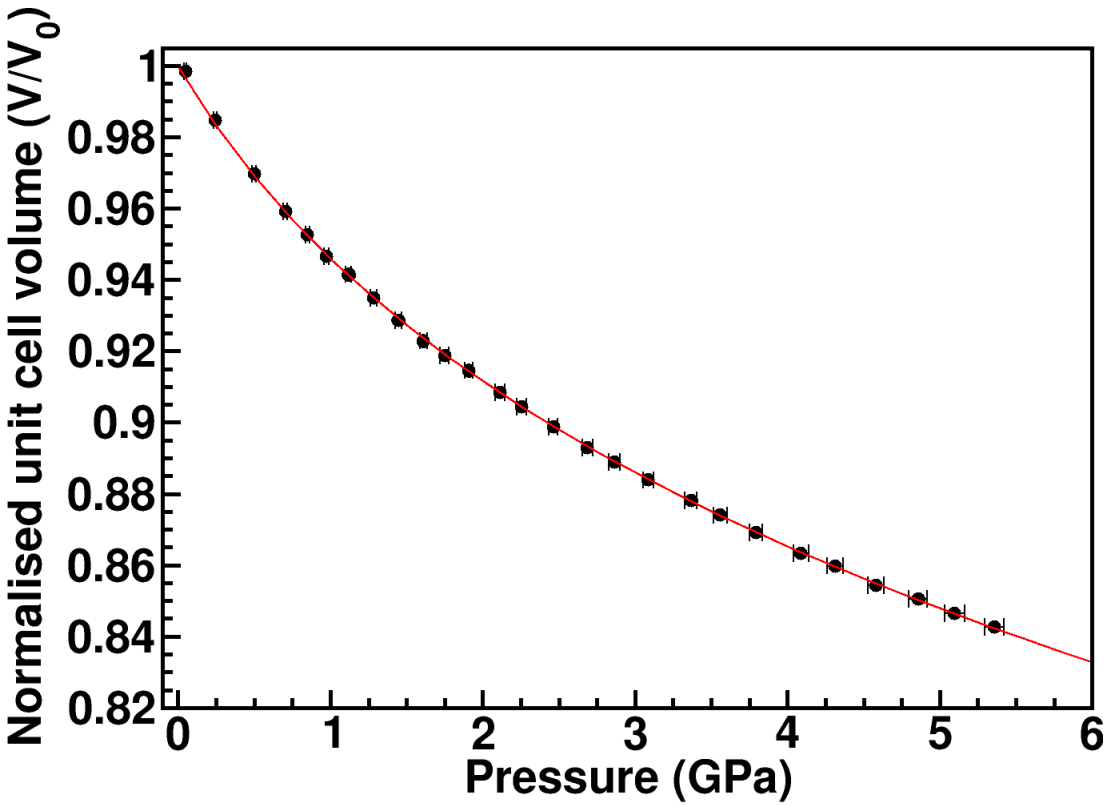

Figure 3.30: Third-order Birch-Murnaghan equation of state for ortho-2(CL-20):HP, overlaid on normalised experimental data as a function of pressure. The calculated equation of state shows good agreement with the experimental data.

Like the 2(CL-20):HMX system, isotropic compression behaviour was observed for the 2(CL-20):HP system. There are minor differences between the compressibility along each axis - for example, the b-axis overall reduced in length by 6.830% over the studied pressure range, compared to a change of 4.770% in the c-axis. However, these differences can be explained by minor changes in void space aligned with each axis - i.e. a greater diameter of void space aligned with b than c.

The bulk modulus (B_0) of the solvate was determined from the equation of state to be 13.4(2) GPa, which is greater than that of ϵ-CL-20 - 9.5(2) GPa. No high-pressure study of α-CL-20 has been performed, so any direct comparison with the isostructural α-CL-20 hydrate is difficult. The pressure derivative (B') was 11.2(3). The initial volume (V_0) was fixed at 2973.62 Å^3 in line with the room-temperature and ambient-pressure lattice parameters achieved from the Pawley refinement and indexing described earlier.

In the same way as for the other two systems, principal axis compressibilities were also calculated for 2(CL-20):HP using PASCal [27]. Since this system also possesses orthorhombic symmetry, the principal axes map directly onto the crystallographic axes. Compressibility values are given for each axis in Table 3.11 below. The greater compressibility value for X_1 (aligned with the b-axis) supports the suggestion above of an increased amount of void space being aligned with b than c.

Table 3.11: Principal axis compressibilities for 2(CL-20):HP, as calculated by PASCal.

Principal Axis	Crystallographic Axis	Compressibility (TPa^{-1})
X_1	b	10.48(6)
X_2	a	9.45(9)
X_3	c	7.68(3)

As with the other two systems, the main interactions in this solvate are a series of C-H...O hydrogen bonding interactions. However, owing to the distances between the HP molecules and suitable atoms on the CL-20 moieties, these interactions mainly only exist between neighbouring CL-20 molecules. The most- and least-compressible contacts have been illustrated in Figure 3.31 below.

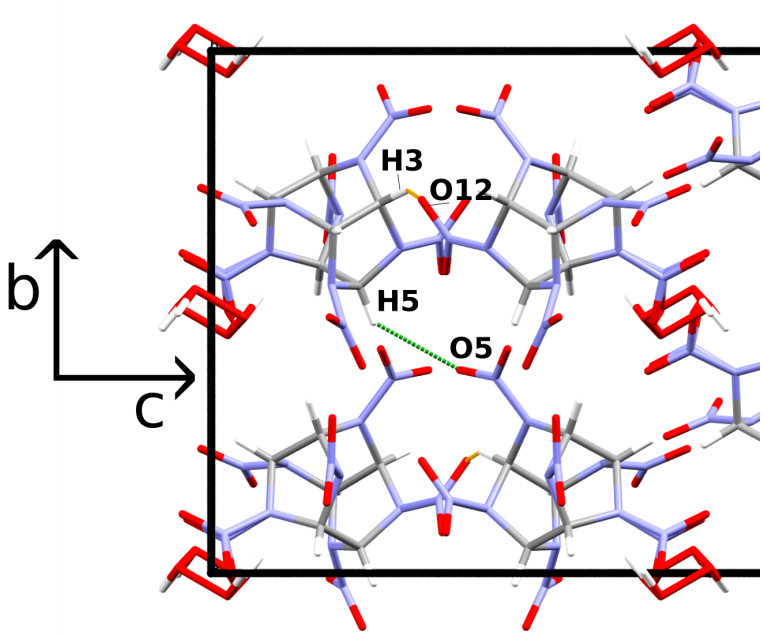

Figure 3.31: The most-and least-compressible hydrogen bonding interactions present in ortho-2(CL-20):HP, as viewed along the b-axis (cf. Figure 3.4). The most-compressible contact, O5...H5, is highlighted in green. The least-compressible contact, O12...H3, is highlighted in orange. As the interactions are mirrored on the opposite side of the unit cell, half of the cell has been omitted for clarity.

The most-compressible hydrogen bonding interaction is the O5...H5 contact, decreasing by 0.514 Å over the studied pressure range, from 2.466(24) to 1.952(19) Å. The least-compressible contact was O12...H3, decreasing by only 0.272 Å over the studied pressure range, from 2.550(21) to 2.278(22) Å. Both of these are contacts between adjacent CL-20 molecules. The O5...H5 contact is aligned primarily along the b-axis, with some c-axis component. The O12...H3 contact, however, is aligned almost-exactly along the a-axis, with only a minuscule b-axis component. The fact that these contacts behave the way they do can be explained by the steric environments they each occupy. O5...H5 exists in such a space that the two CL-20 molecules can conceivably move closer under compression without too much steric hindrance. O12...H3, however, is in a very hindered environment. The NO_2 group and associated C-H are already physically close to each

other. Compression will result in even more steric hindrance occurring, limiting the degree to which this contact can shorten.

No polymorphic transitions were observed over the course of this experiment, as demonstrated by a lack of any significant changes in the diffraction pattern with increasing pressure, and a lack of any significant discontinuities in the pressure-volume curve.

Future steps and directions for further studies of these materials are discussed in Chapter 6.

3.3 References

[1] R. Wardle, J. Hinshaw, P. Braithwaite, M. Rose, G. Johnston and R. Jones, "ADPA", Arlington, Virginia, 27–31.

[2] U. R. Nair, R. Sivabalan, G. M. Gore, M. Geetha, S. N. Asthana and H. Singh, *Combustion, Explosion and Shock Waves*, 2005, **41(2)**, 121–132.

[3] J. Akhavan, *The Chemistry of Explosives*, 3rd edn., RSC Publishing, 2011.

[4] J. Giles, *Nature*, 2004, **427**, 580–581.

[5] J. Pichtel, *Applied and Environmental Soil Science*, 2012, **2012**, 617236.

[6] A. Nielsen, S. Christian, D. Moore, M. Nadler, R. Nissan, D. Vanderah, R. Gilardi, C. George and J. Flippen-Anderson, *Tetrahedron*, 1998, **54**, 11793–11812.

[7] N. Bolotina, M. Hardie, R. Speer Jr. and A. Pinkerton, *Journal of Applied Crystallography*, 2004, **37**, 808–814.

[8] D. I. Millar, H. E. Maynard-Casely, A. K. Kleppe, W. G. Marshall, C. R. Pulham and A. S. Cumming, *CrystEngComm*, 2010, **12(9)**, 2524–2527.

[9] H. Cady, A. Larson and D. Cromer, *Acta Crystallographica*, 1963, **16**, 617–623.

[10] J. Deschamps, M. Frisch and D. Parrish, *Journal of Chemical Crystallography*, 2011, **41**, 966–970.

[11] P. Main, R. Cobbledick and R. Small, *Acta Crystallographica C*, 1985, **41**, 1351–1354.

[12] R. Cobbledick and R. Small, *Acta Crystallographica B*, 1974, **30**, 1918–1922.

[13] W. Carper, L. Davis and M. Extine, *Journal of Physical Chemistry*, 1982, **86**, 459–462.

[14] R. Vrcelj, J. Sherwood, A. Kennedy, H. Gallagher and T. Gelbrich, *Crystal Growth & Design*, 2003, **3**, 1027–1032.

[15] O. Bolton, L. R. Simke, P. F. Pagoria and A. J. Matzger, *Crystal Growth & Design*, 2012, **12(9)**, 4311–4314.

[16] S. R. Anderson, D. J. am Ende, J. S. Salan and P. Samuels, *Propellants, Explosives, Pyrotechnics*, 2014, **39(5)**, 637–640.

[17] O. Bolton and A. J. Matzger, *Angewandte Chemie International Edition*, 2011, **50(38)**, 8960–8963.

[18] J. Bennion, N. Chowdhury, J. Kampf and A. Matzger, *Angewandte Chemie International Edition*, 2016, **55**, 13118–13121.

[19] J. Ledgard, *The Preparatory Manual of Explosives*, 3rd edn., Lulu. com, , 2014.

[20] G. Jacob, L. Toupet, L. Ricard and G. Cagnon, *CSD Communication*, 1999.

[21] O. Arnold, *Nuclear Instruments and Methods in Physics A*, 2014, **764**, 156–166.

[22] C. L. Bull, N. P. Funnell, M. G. Tucker, S. Hull, D. Francis and W. G. Marshall, *High Pressure Research*, 2016, **36**, 493–511.

[23] A. C. Larson and R. B. Von Dreele, *General Structure Analysis System. LANSCE, MS-H805, Los Alamos, New Mexico*, 1994.

[24] B. H. Toby, *Journal of Applied Crystallography*, 2001, **34(2)**, 210–213.

[25] B. H. Toby and R. B. Von Dreele, *Journal of Applied Crystallography*, 2013, **46(2)**, 544–549.

[26] R. J. Angel, M. Alvaro and J. Gonzalez-Platas, *Zeitschrift für Kristallographie-Crystalline Materials*, 2014, **229(5)**, 405–419.

[27] M. Cliffe and A. Goodwin, *Journal of Applied Crystallography*, 2012, **45**, 1321–1329.

[28] S. M. Peiris and G. J. Piermarini, *Static Compression of Energetic Materials*, Springer-Verlag, 2008.

[29] D. I. Millar, "Energetic Materials at Extreme Conditions", Ph.D. thesis, University of Edinburgh, 2011.

[30] J. C. Gump and S. M. Peiris, *Journal of Applied Physics*, 2005, **97(5)**, 053513.

[31] L. Stevens, N. Velisavljevic, D. Hooks and D. Dattelbaum, *Applied Physics Letters*, 2008, 081912.

[32] A. Boultif and D. Louër, *Journal of Applied Crystallography*, 1991, **24(6)**, 987–993.

Chapter 4

High-pressure studies of Nitroguanidine co-crystals

This chapter concerns the high-pressure behaviour of two co-crystals of nitroguanidine - NQ:2-hydroxy-5-nitropyridone (NQ:NP), and NQ:2-hydroxy-3,5-dinitropyridone (NQ:DNP).

Nitroguanidine (**NQ**, Figure 4.1a) is a nitro derivative of guanidine. It is classed as a flammable solid if appropriately wetted, and a secondary explosive when dry. First synthesised in the late 19th century [1], the material has since found an array of niche uses. NQ is primarily employed as a component of smokeless triple-base propellants in weapons systems - a role that was historically performed by mixtures such as gunpowder. For example, NQ is the primary component in modern formulations of Cordite. The material also finds use in civilian applications, such as in car airbags.

On account of NQ's combination of very low sensitivity (> 320 cm drop height needed to initiate) and high detonation velocity (8,800 m/s) [2], NQ-containing compositions are of interest for both military and civilian applications.

NP and **DNP** (Figures 4.1b and 4.1c respectively) do not have any notable uses outside of synthetic chemistry. Their choice as co-formers in these experiments is a result of an earlier co-crystal screening project performed by Paul Coster [3], which was aimed at identifying potential co-formers with which NQ might form co-crystals.

None of the three co-former compounds possess any known polymorphic behaviour. NQ crystallises in the orthorhombic crystal system with space group $Fdd2$ [4], while no crystal structures of NP or DNP have been published. Keto-enol tautomerism is present in NP and DNP, as illustrated in Figure 4.2.

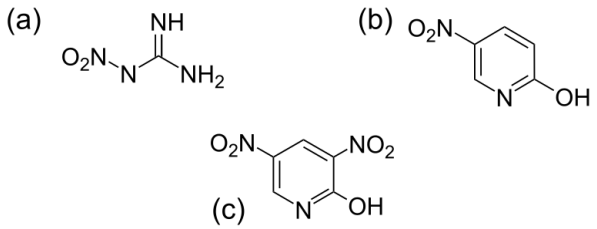

Figure 4.1: Molecular structures of (a) NQ - $CH_4N_4O_2$; (b) NP - $C_5H_4N_2O_3$; (c) DNP - $C_5H_3N_3O_5$.

Table 4.1: Lattice parameters for NQ:NP, collected at 120 K and solved/refined by the author using ShelXT and ShelXL with Olex2. Associated refinement factors are also given.

Parameter	Value
a	13.4128(6) Å
b	11.2200(3) Å
c	13.8451(6) Å
α	90 °
β	114.255(5) °
γ	90 °
V	1899.65(15) Å^3
R_1	4.12 %
$G_{of}(F^2)$	1.256
$\sigma_{max/min}$	0.29 / -0.26
ρ_{calc}	1.281 g/cm^3
λ	0.7107 Å
Reflections	23821
Z	8
Space group	$P2_1/c$

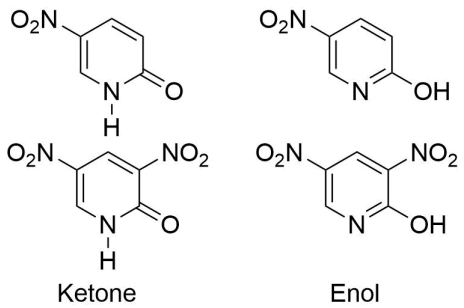

Figure 4.2: Keto-enol tautomerism present in NP (upper) and DNP (lower), where the molecule can interconvert between pyridine (enol) and pyridone (ketone) forms.

Coster showed that NQ:NP crystallised in the monoclinic crystal system with space group $P2_1/c$, with 8 molecules of NQ and 8 molecules of NP per unit-cell. The structure is distinctly layered, with flat planes of NQ and NP molecules parallel to each other (Figures 4.3 and 4.4). The structure was solved from single-crystal X-ray diffraction data, using ShelXT (Intrinsic Phasing structure solution) and ShelXL (Least Squares minimisation) through Olex2 [5, 6], giving the lattice parameters in Table 4.1.

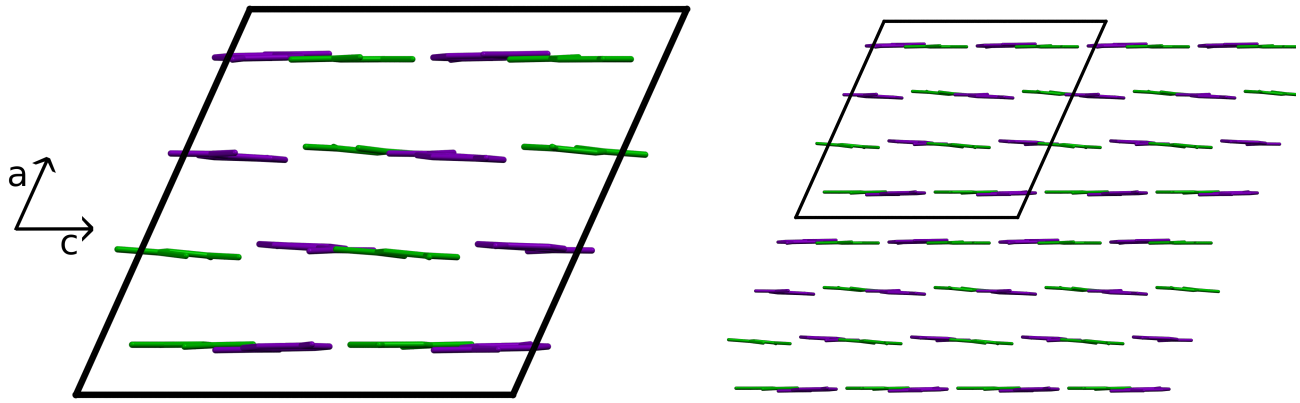

Figure 4.3: Crystal structure of NQ:NP, viewed along the *b*-axis. NQ molecules are highlighted in green, with NP molecules in purple. The sheet-type layering is clearly visible in this view. The unit-cell is shown on the left, with an expanded 2x2 packing arrangement shown on the right. Hydrogen atoms have been omitted for clarity. The crystal structure contains the keto-tautomer of NP.

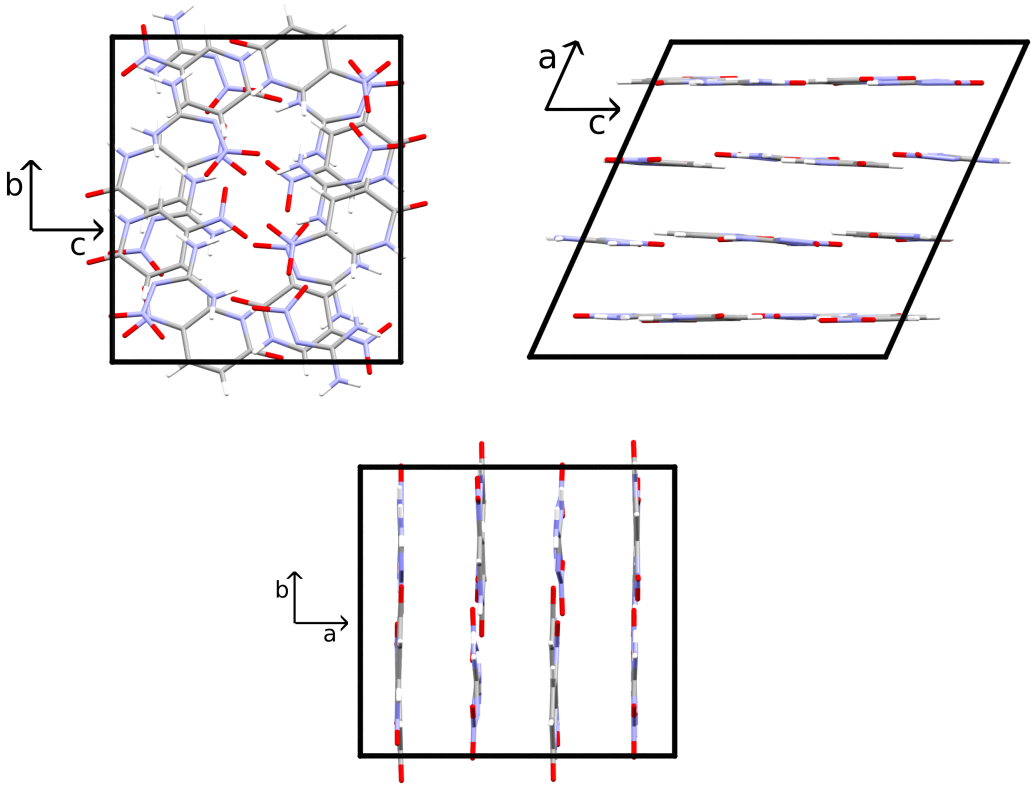

Figure 4.4: Crystal structure of NQ:NP, viewed along the *a*-, *b*- and *c*-axes, without molecular colouring, and with hydrogens present

NQ:DNP crystallises in the monoclinic $P2_1/n$ space group, with 4 molecules of NQ and 4 molecules of DNP per unit-cell. The layering in this structure forms a unique herringbone pattern, with zig-zagging layers of co-formers across the unit-cell (Figures 4.5 and 4.6). The structure was solved by the author from single-crystal X-ray diffraction data collected on an Oxford Diffraction Xcalibur single-crystal diffractometer at 120 K with Mo-Kα radiation across a $2 - theta$ range of 5.446 to 52.74 ° , using ShelXD (Dual Space

Table 4.2: Lattice parameters for NQ:DNP, collected at 120 K and solved/refined using ShelXD and ShelXL with Olex2. Associated refinement factors are also given.

Parameter	Value
a	9.6282(7) Å
b	11.3720(5) Å
c	10.7909(7) Å
α	90 °
β	113.049(8) °
γ	90 °
V	1087.20(13) Å^3
R_1	4.18 %
$G_{of}(F^2)$	1.049
$\sigma_{max/min}$	0.38 / -0.25
ρ_{calc}	1.334 g/cm^3
λ	0.7107
Reflections	17505
Z	6
Space group	$P2_1/n$

structure solution) and ShelXL (Least Squares minimisation) through Olex2 [5, 6]. Lattice parameters are given in Table 4.2.

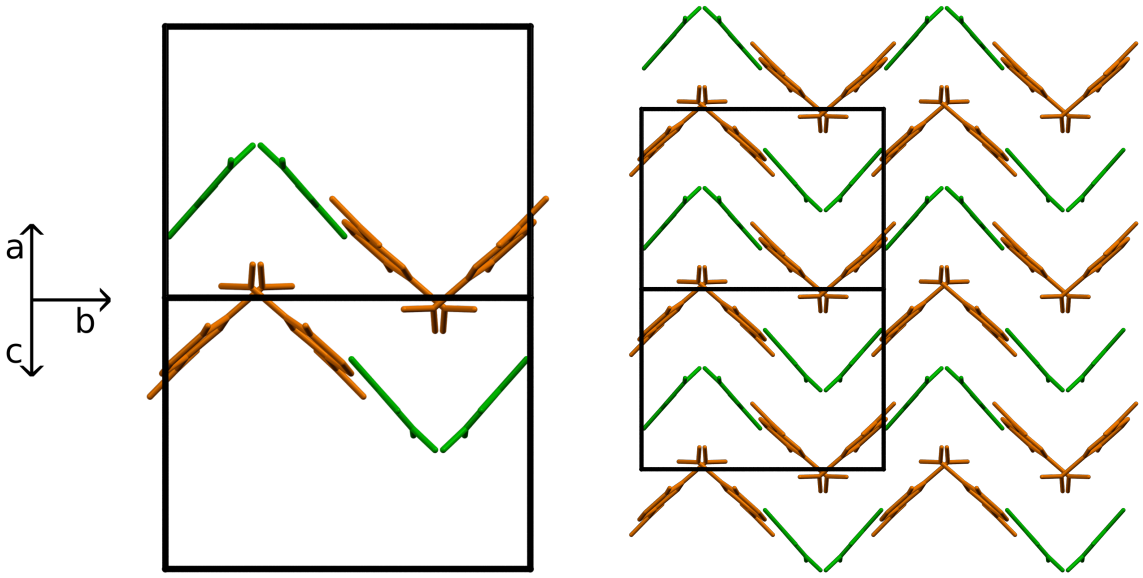

Figure 4.5: Crystal structure of NQ:DNP, viewed along a diagonal between the a and c-axes. Molecules of NQ have been highlighted in green, with DNP molecules shown in orange. The distinctly herringbone-layered unit-cell is shown on the left, with an enlarged packing arrangement on the right. Hydrogen atoms have been omitted for clarity. The crystal structure contains the keto-tautomer of DNP.

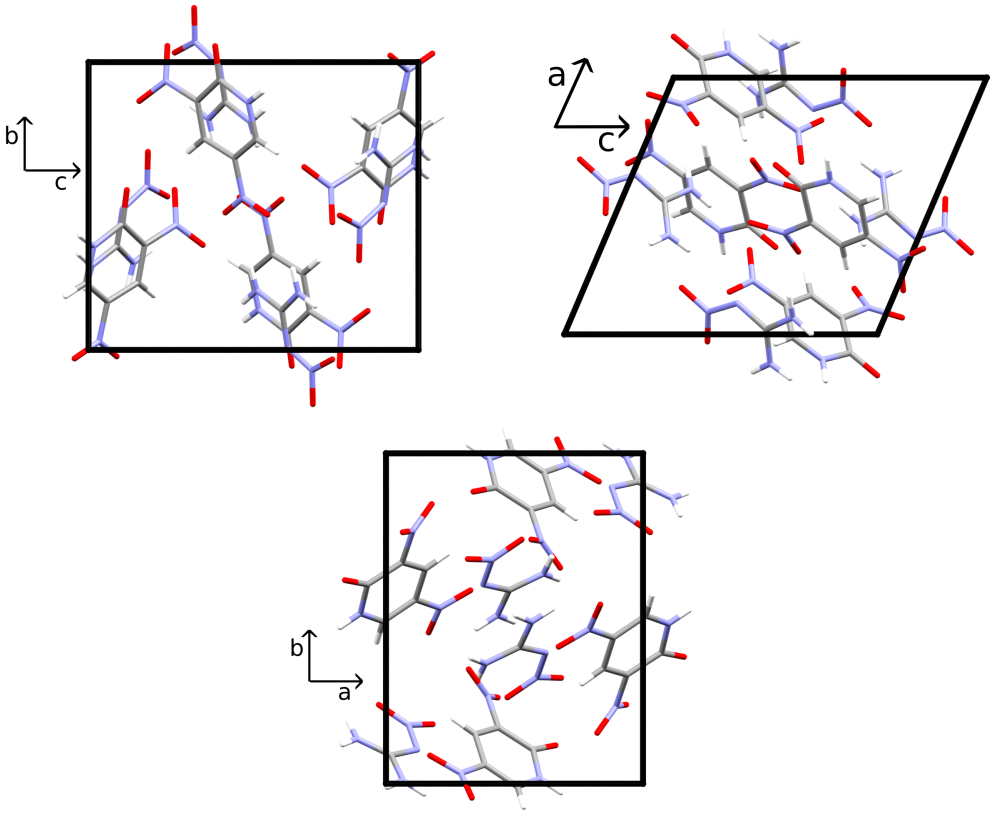

Figure 4.6: Crystal structure of NQ:DNP, viewed along the *a*-, *b*- and *c*-axes, without molecular colouring, and with hydrogens present.

To date, no high-pressure diffraction or spectroscopic studies of this class of materials had been reported in the literature. Following successful beamtime applications, these two systems were studied on the PEARL instrument at ISIS in March 2015 (NQ:DNP); and October 2017 (NQ:NP). The following sections of this chapter will describe these experiments in more detail.

4.1 Experimental

4.1.1 NQ:NP

Preparation of NP-d_4

Two of the three deuterated co-formers (NQ-d_4 and DNP-d_3) were previously prepared by Daniel Ward. NP-d_4 was produced as part of this study through recrystallisation from deuterated solvents. The following materials were used in the preparation of NP-d_4: 2-hydroxy-5-nitropyridine ($C_5H_4N_2O_3$, purchased from Fisher Scientific); deuterium oxide (D_2O, 99.9 %, acquired from Sigma-Aldrich); and methanol-d_4 (CD_3OD, 99.9 %, acquired from Cambridge Life Sciences).

A quantity of NP was dissolved in a 100 ml round-bottomed flask containing the minimum possible amount

of D_2O and methanol-d_4 ($\sim$ 40 ml). The flask was then heated (with an attached reflux condenser) to $\sim$ 80 °C and allowed to stir until all of the NP had dissolved. The flask was then left to stir under heat for three hours. Following this, the mixture was allowed to cool to room temperature (with the flask sealed to reduce exposure to atmospheric moisture), and the pale-yellow NP-d_4 began to precipitate out. The solid was removed by vacuum filtration, and dried overnight in a vacuum desiccator.

The solid NP was then subjected to an NMR study to ascertain the extent of deuteration. Difficulties were encountered in obtaining useable ^{2}H-NMR data for this sample. However, the ^{1}H NMR, shown in Figure 4.7 below, was taken as an indication that the sample was suitably deuterated. The integration values of sample peaks were found to be smaller than those of the residual hydrogenous material present in the deuterated solvent.

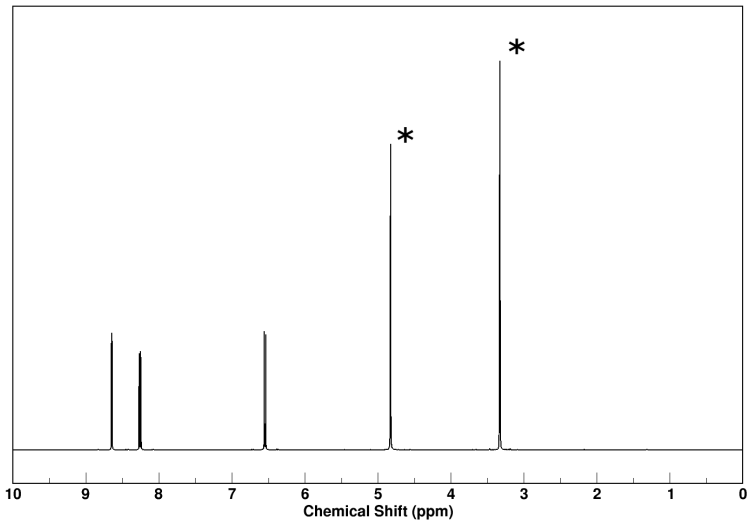

Figure 4.7: ^{1}H NMR spectrum of NP dissolved in methanol-d_4. The peaks with the greatest integration values (asterisked) in the ^{1}H spectrum result from the negligible quantity of hydrogen contained within the deuterated solvent (rated at 99.9 % purity). This implies that hydrogenous NP is in a smaller relative quantity than the residual non-deuterated solvent, and was therefore presumed to be in concentration of $<$ 0.1 mol%.

Preparation of the NQ:NP co-crystal

This co-crystal was prepared through solution methods and evaporative crystallisation, using the method employed by Coster [3]. Materials utilised in this preparation were as follows: nitroguanidine-d_4 ($CD_4N_4O_2$, NQ-d_4, previously prepared at the University of Edinburgh by Daniel Ward); 2-hydroxy-5-nitropyridine-d_4 ($C_5D_4N_2O_3$, NP-d_4, prepared by the method in Section 4.1.3); deuterium oxide (D_2O, 99.9 %, purchased from Sigma-Aldrich); and methanol-d_4 (CD_3OD, 99.9 %, purchased from Cambridge Life Sciences).

Stoichiometric amounts of NQ-d_4 and NP-d_4, in a 1:1 molar ratio (0.213 and 0.287 g respectively), were combined in a 100 ml round-bottomed flask. Minimum amounts of D_2O and methanol-d_4 were added (in

a 3:1 v/v ratio, total $\sim$ 35 ml). A reflux condenser was attached, and the flask was heated to 85 °C for 3 hours. The flask was then removed from heat, stoppered, and allowed to cool to room temperature. A pale yellow solid precipitated out at this point. The precipitate was separated by vacuum filtration and dried overnight in a vacuum desiccator, before being analysed by X-ray powder diffraction.

This evaporative process was repeated three times to generate a sample of sufficient mass and purity. The X-ray diffraction measurements were performed with a flat-plate geometry Bruker D2 Phaser using Cu-Kα radiation, over a 2θ range of 5 to 45 ° for 20 minutes duration. An example X-ray diffraction pattern is shown in Figure 4.8.

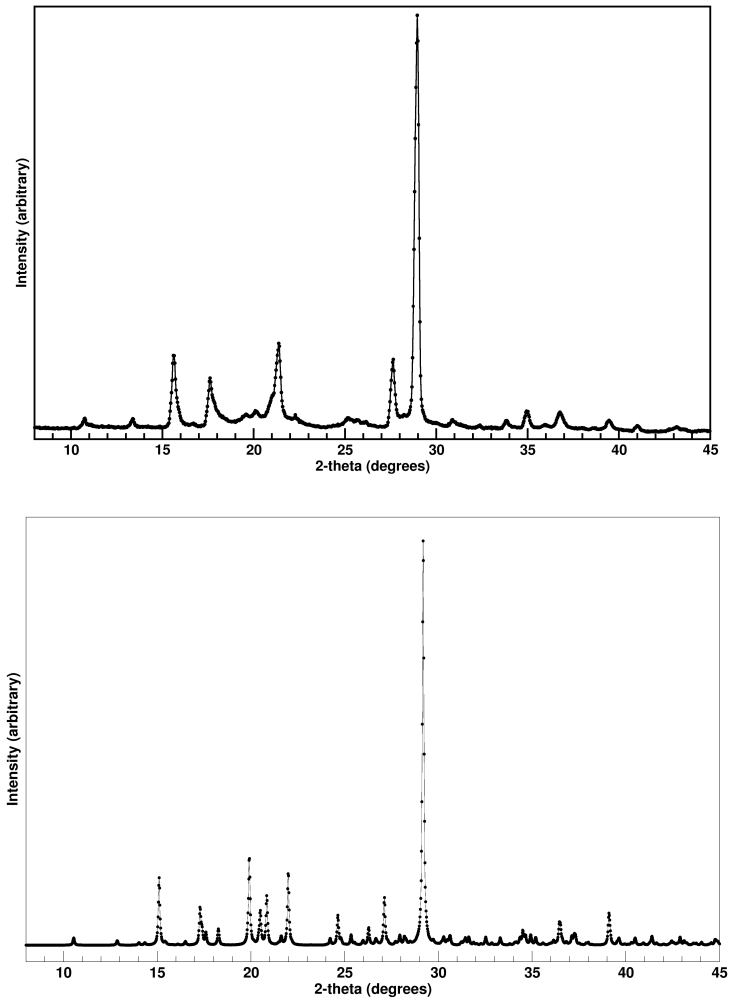

Figure 4.8: Experimental powder X-ray diffraction pattern of NQ:NP (top) at 1.5406 Å, compared to a simulated pattern generated from the single-crystal data collected at 120 K (bottom). For safety reasons, the sample was only lightly ground prior to analysis, so a degree of preferred orientation may be present in the data. No refinement was carried out on this data, as the quality of the pattern was poor and so of dubious value in calculating phase purity. However, the patterns show obvious similarities.

After transporting the sample to the ISIS Neutron Source, a high-pressure study was conducted according to the procedures outlined in Section 4.1.3. The maximum load applied to this sample was 50 tonnes, equating

to a pressure of approximately 4.78 GPa.

4.1.2 NQ:DNP

This co-crystal sample was, like the CL-20 systems discussed in the previous chapter, prepared using the Resonant Acoustic Mixing (RAM) method.

Materials utilised in this preparation were as follows: nitroguanidine-d_4 ($CD_4N_4O_2$, NQ-d_4, previously prepared by Daniel Ward at the University of Edinburgh); 2-hydroxy-3,5-dinitropyridine-d_3 ($C_5D_3N_3O_5$, DNP-d_3, also previously prepared by Daniel Ward); and methanol-d_4 (CD_3OD, 99.9 %, purchased from Cambridge Life Sciences).

Stoichiometric amounts of NQ-d_4 and DNP-d_4, in a 1:1 molar ratio (0.180 and 0.320 g respectively), were combined in a 15 ml glass sample vial. Two drops of methanol-d_4 ($\sim$ 60 μl) were added to the vial, which was immediately sealed. The vial was then subjected to a RAM cycle at an acceleration of 75 G for 1 hour. This process was repeated twice, with powder X-ray diffraction patterns collected after each cycle.

Powder X-ray diffraction measurements were performed using a Bruker D2 Phaser in flat-plate geometry using Cu-Kα radiation, over a 2θ range of 5 to 45 $^\circ$ for a total duration of 20 minutes. An example X-ray diffraction pattern is shown in Figure 4.9.

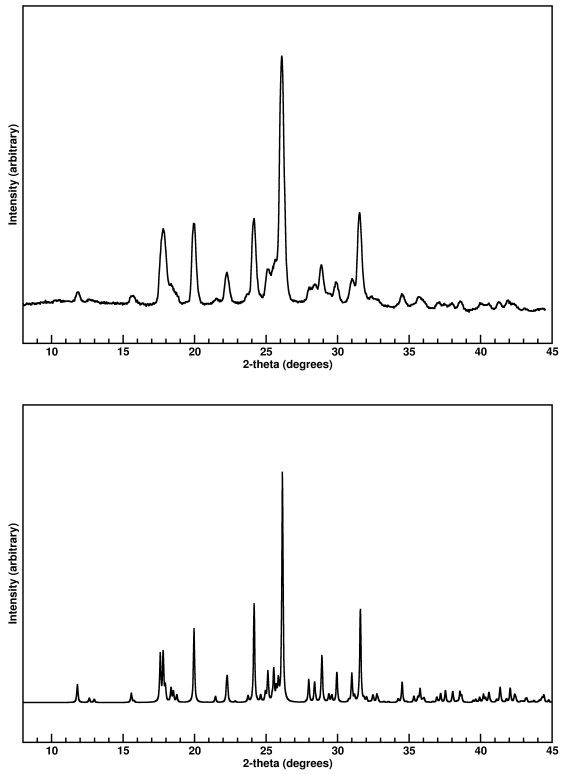

Figure 4.9: Experimental powder X-ray diffraction pattern of NQ:DNP (top) collected with Cu-Kα radiation (1.5406 Å), compared to a simulated pattern generated from the single-crystal data collected at 120 K (bottom). For safety reasons, the sample was only lightly ground prior to analysis, so a degree of preferred orientation may be present in the data. As before, no refinement was performed as the poor quality of the diffraction pattern would not necessarily yield useful phase purity results. However, the patterns appear similar.

Following careful transport of the sample to the ISIS Neutron Source, a study at high-pressure was conducted according to the procedures in Section 4.1.3. The maximum load applied to this sample was 43 tonnes - a pressure of approximately 4.49 GPa.

4.1.3 High-pressure studies and common aspects

As with the CL-20 systems, both NQ co-crystals contained common experimental aspects in how they were studied under high-pressure conditions.

In both cases, a V3 Paris-Edinburgh press was employed on the PEARL instrument to generate the required pressures. Each experiment used single-toroidal anvils of zirconia-toughened alumina (ZTA), with a titanium zirconium (TiZr) gasket. A 4:1 mixture of deuterated methanol and ethanol was used as a pressure transmitting medium in each case, with a small pellet of lead used as a pressure calibrant.

A d-spacing range of 1 - 4 Å was studied in each experiment. As with the systems in the previous chapter, the region of below 1 Å was excluded, as the large number of overlapping low-intensity reflections in this

region inhibited the completion of Rietveld refinements. The region beyond 4 Å is not normally accessible in the default PEARL setup due to the geometry of the P-E cell.

The program Mantid was used to normalise the collected data. The software also applied corrections for attenuation of the neutron beam caused by the anvils and gasket [7, 8]. Lattice parameters and structural information for each system were determined from Rietveld refinements, using GSAS with EXPGUI [9, 10]. The two single-crystal structures discussed in Section 4 were used as a starting point for refinements, with an example fit shown in Figure 4.10. Additional scattering from the ZTA anvils and the pressure calibrant were accounted for as additional refinement phases.

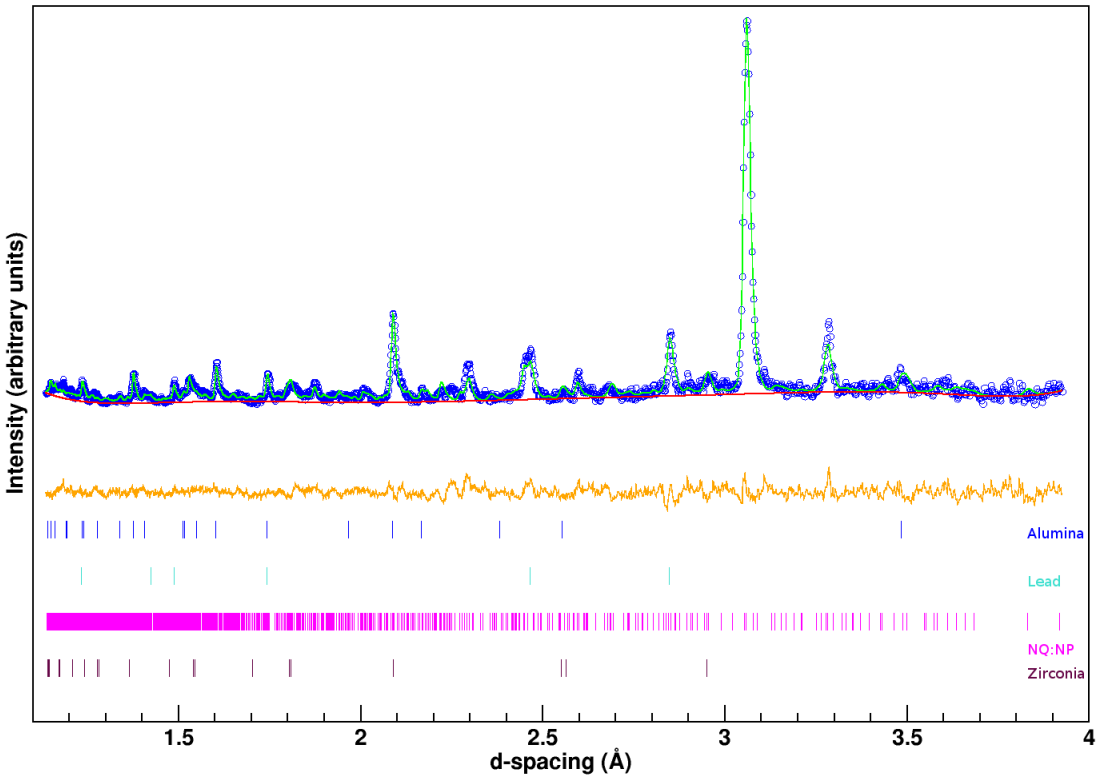

Figure 4.10: Example Rietveld refinement of NQ:NP, from data recorded at 0.56 GPa. The refinement pattern is denoted in green, with blue circles representing experimental data points. The orange line denotes the difference between the model and experimental data. The tickmarks, from top to bottom, show respectively Bragg reflections from the alumina component of the anvils (blue); the lead pressure calibrant (cyan); the NQ:NP co-crystal (magenta); and the zirconia component of the anvils (purple).

The good fit between the calculated refinement and experimental data demonstrated that the sample is phase-pure and fully deuterated.

Rigid bodies were applied to the NQ and co-former molecules for each system to restrain the refinement of atomic positions. Cartesian co-ordinates were generated for each molecule using Mercury, and mapped onto the co-crystal structures as separate rigid bodies using GSAS-II [11]. The initial GSAS/EXPGUI refinements were used as a starting point for the subsequent GSAS-II analyses, where the position and

rotation angles of each rigid body were allowed to refine.

Once rigid bodies were applied to the structure, refinements proceeded by first refining the background of the pattern using a shifted Chebyschev function with 8-12 terms in the background function. Following optimisation of the background, the lattice parameters and phase fractions were allowed to refine with mild damping applied. Subsequently, the rigid body origins and torsion angles were allowed to refine, along with the rigid body thermal displacement. Lastly, the sigma-1 and gamma-1 profile functions of the pattern were allowed to refine where appropriate until optimal R-factors were achieved.

The experimental data were used to determine equations of state for each system using EOSFit7 [12]. For both systems, a third-order Birch-Murnaghan equation of state was fitted to the experimental pressure-volume data. For NQ:DNP, this equation of state analysis was only performed using data up to 0.86 GPa, on account of an observed phase transition. For NQ:NP, the full experimental data-set up to 4.78 GPa was used in EOSFit calculations. The experimental datasets were also processed with PASCal to observe how the changes in unit-cell parameters related to the principal axes of compression [13].

4.2 Results and Discussion

4.2.1 NQ:NP

In NQ:NP, the a-axis appears to decrease at a markedly greater rate than b and c over the studied pressure range. This trend in the lattice parameter compression can be clearly seen in Figure 4.11, where normalised lattice parameters have been plotted as a function of pressure. Un-normalised values are given in Table 4.3.

As with the systems in the previous chapter, lattice parameters have been normalised to a "zero" value for graphing purposes. As time constraints prevented the acquiring of lattice parameters at 298 K and ambient pressure, plots have been normalised to the values in the original single-crystal data. As these data were collected at 120 K, compared to the high-pressure neutron study carried out at 298 K, some initial values may appear above 1 on the normalised plots due to thermal expansion between 120 and 298 K. Lattice parameters from the original crystal structure were given earlier in this chapter, in Table 4.1.

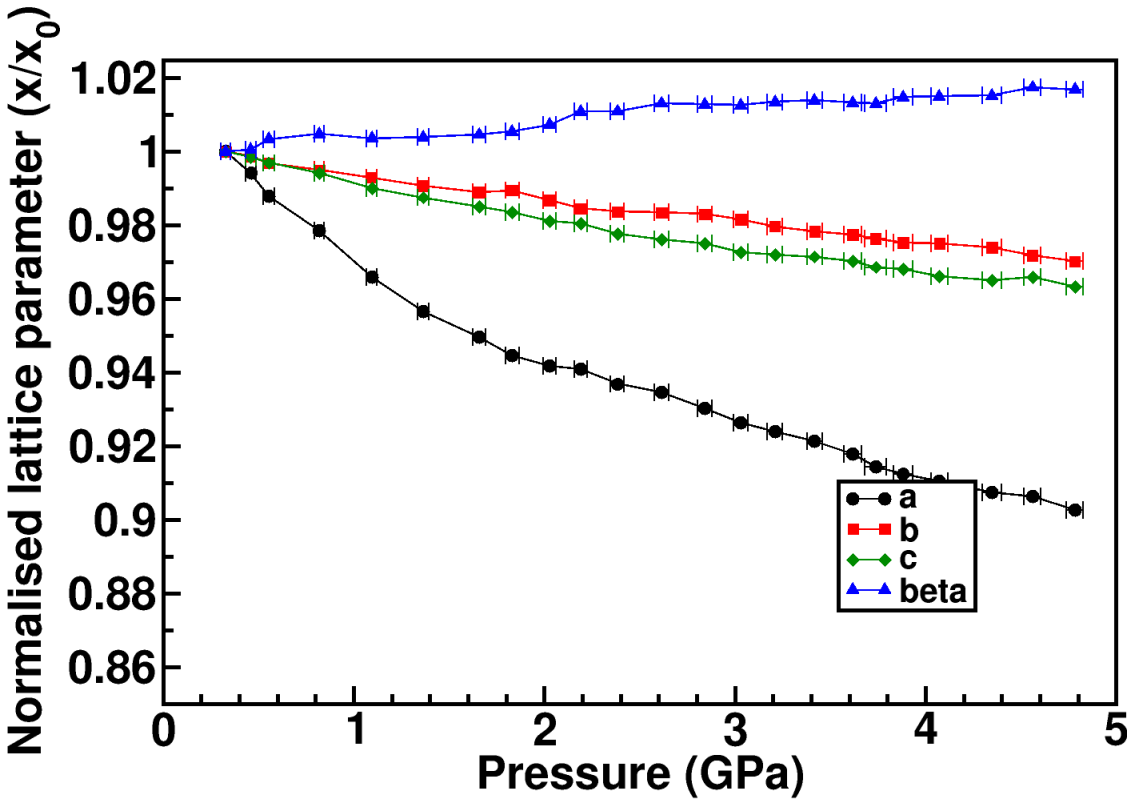

Figure 4.11: Normalised lattice parameters for NQ:NP as a function of pressure, normalised to the values acquired from the first pressure point data-set. Error bars on the y-axis, as calculated from the Rietveld refinement, are too small to display on this scale.

Table 4.3: Lattice parameters for NQ:NP at each pressure point during this experiment, along with associated refinement factors. Rietveld refinement was performed as described in Section 4.1.3

Pressure (GPa)	a (Å)	b (Å)	c (Å)	β (°)	V (Å^3)	R_p (%)	R_{wp} (%)	GoF
0.33(3)	13.603(18)	11.244(4)	13.831(24)	114.09(5)	1931.2(7)	3.49	4.10	1.39
0.46(3)	13.523(16)	11.230(3)	13.811(21)	114.16(4)	1913.7(6)	3.36	3.86	1.30
0.56(3)	13.437(14)	11.210(4)	13.788(18)	114.49(4)	1890.1(6)	3.39	3.72	1.24
0.82(3)	13.310(14)	11.188(4)	13.750(18)	114.65(3)	1861.1(6)	3.19	3.71	1.22
1.10(3)	13.139(14)	11.166(3)	13.693(18)	114.51(3)	1827.9(6)	3.40	3.87	1.29
1.37(3)	13.013(13)	11.140(3)	13.659(18)	114.55(3)	1801.2(6)	3.37	4.01	1.28
1.66(3)	12.918(15)	11.120(4)	13.623(20)	114.63(4)	1779.0(6)	3.70	4.27	1.36
1.83(4)	12.849(10)	11.127(3)	13.603(14)	114.72(3)	1766.5(6)	3.64	4.00	1.26
2.03(3)	12.811(12)	11.096(3)	13.571(17)	114.94(3)	1749.4(6)	3.77	4.11	1.29
2.19(3)	12.798(13)	11.071(3)	13.561(18)	115.34(3)	1736.5(6)	3.75	4.14	1.32
2.38(4)	12.744(13)	11.061(4)	13.523(19)	115.35(3)	1722.7(6)	3.93	4.20	1.29
2.62(4)	12.713(13)	11.059(4)	13.500(19)	115.60(3)	1711.6(7)	3.90	4.28	1.33
2.84(4)	12.654(11)	11.053(3)	13.487(16)	115.56(3)	1701.9(6)	3.95	4.22	1.28
3.03(4)	12.601(12)	11.038(4)	13.452(17)	115.54(3)	1688.3(6)	4.15	4.41	1.33
3.21(4)	12.569(11)	11.016(3)	13.445(15)	115.63(3)	1678.4(6)	4.04	4.23	1.27
3.42(4)	12.532(11)	11.000(3)	13.436(15)	115.68(3)	1669.3(5)	3.92	4.16	1.24
3.62(5)	12.485(13)	10.991(3)	13.420(19)	115.61(3)	1660.6(6)	4.10	4.37	1.29
3.74(6)	12.438(13)	10.978(3)	13.397(19)	115.59(3)	1649.9(5)	4.08	4.33	1.27
3.89(5)	12.413(12)	10.967(4)	13.389(18)	115.79(3)	1641.1(6)	4.08	4.42	1.29
4.07(5)	12.384(13)	10.964(3)	13.362(18)	115.81(3)	1633.3(6)	4.03	4.45	1.28
4.35(5)	12.344(14)	10.952(4)	13.348(20)	115.84(3)	1624.0(6)	4.28	4.54	1.30
4.56(4)	12.330(14)	10.927(4)	13.359(21)	116.09(4)	1616.4(7)	4.13	4.55	1.53
4.78(5)	12.278(13)	10.909(3)	13.323(19)	116.03(3)	1603.6(6)	3.94	4.28	1.20

In Figure 4.12, the pressure-volume curve is shown overlaid with the equation of state derived from the experimental data.

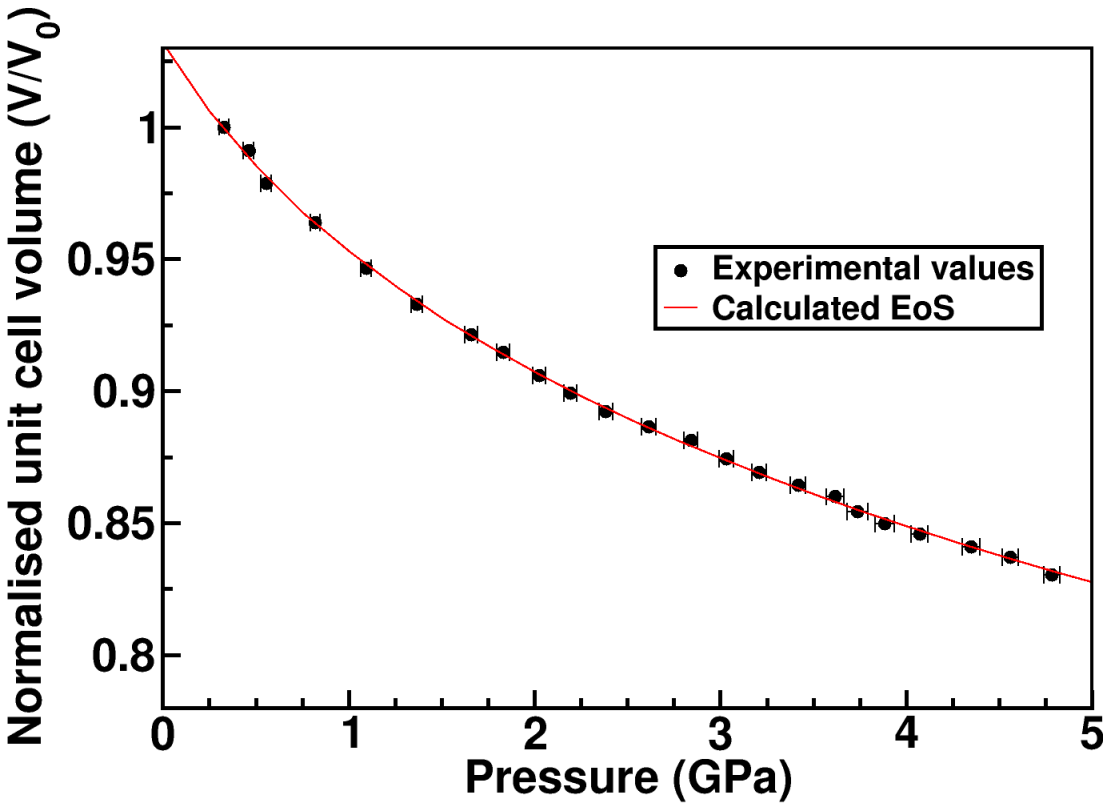

Figure 4.12: Calculated third-order Birch-Murnaghan equation of state for NQ:NP, overlaid on normalised experimental data, as a function of pressure. Error bars on the y-axis are too small to be displayed on this scale.

From the equation of state, the bulk modulus (B_0) of NQ:NP was determined to be 8.7(9) GPa, with pressure derivative $B' = 9.7(9)$. The initial volume (V_0) was determined to be 1993.0(9.3) Å^3, compared to the single-crystal volume of 1899.65 Å^3. No comparison can currently be made in terms of bulk modulus between the co-crystal and co-formers, as no bulk moduli have been published for NQ or NP individually.

The increased response of the *a*-axis to hydrostatic compression can be easily explained through the layering of the structure. As can be seen in Figure 4.3, the layers of NQ and NP are perpendicular to the *a*-axis, with the *b*- and *c*-axes parallel. Therefore, the *a*-axis becomes the primary component of the inter-layer spacing. With the reduced steric hindrance along this axis, this axis will preferentially compress, pushing the layers closer together in a manner similar to that seen in CL-20:TNT (Section 3.2.2). Interestingly, the beta angle is observed to *increase* with pressure in line with subtle movement of the layers.

PASCal was used to calculate principal axis compressibilities for this system.[13] The relation between the principal axes and crystallographic axes is given in Table 4.4 below, along with the compressibility value for each principal axis.

Table 4.4: The extent to which each crystallographic axis (on a scale of -1 to 1) contributes to the three principal stress/strain axes, as calculated by PASCal, with associated compressibility values for each principal axis.

Principal axis	a component	b component	c component	Compressiblity ($TPa^{-}1$)
X_1	-0.9106	0.0	-0.4134	18.5744(1917)
X_2	0.0669	0.0	-0.9978	7.1068(1624)
X_3	0.0	1.0	0.0	5.9449(1467)

These principal axis compressibilities very much resemble the picture seen on the crystallographic level - the X_1 axis, with a large a-axis component, shows the greatest compressibility over the studied pressure range.

As expected, the inter-layer spacing decreases with increasing pressure. Since this inter-layer distance (> 2.7 Å) is too great for hydrogen bonding to take place, the primary intermolecular interactions take place within the layers between individual NQ and NP moieties. The most- and least-compressible contacts in this category are shown in Figure 4.13.

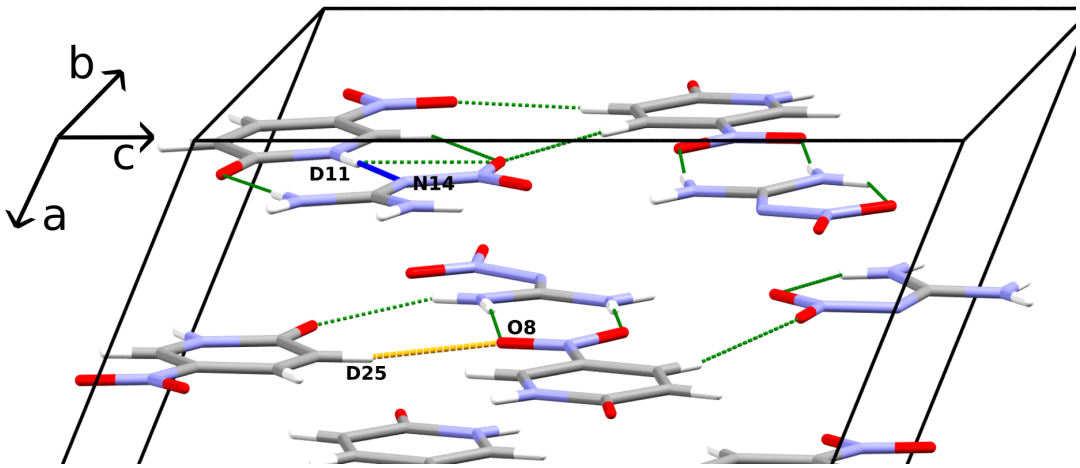

Figure 4.13: The most- and least-compressible hydrogen bonding interactions present within layers in NQ:NP, seen from a partially-offset b-axis view (c.f. Figure 4.3. The most-compressible contact, D11-N14 is highlighted in blue; with the least-compressible contact, O8-D25 highlighted in orange. As the intermolecular interactions are mirrored on the other side of the unit-cell, the image has been truncated for clarity. Other hydrogen bonding interactions are shown in green.

The most compressible intra-layer contact is the D11-N14 interaction between two adjacent NQ and NP moieties, which exists along a diagonal with the b- and c-axes. This decreases by a total of 0.676 Å over the studied pressure range. The least-compressible contact proved to be the O8-D25 interaction between the nitro group and a deuterium on two adjacent NP moieties, the direction of which is almost entirely parallel

with the *c*-axis.

Interestingly, this experimental study contrasts with the earlier (unpublished) synchrotron X-ray study performed at the Diamond Light Source by Paul Coster in 2013. This experiment used a diamond-anvil cell, with a tungsten gasket and ruby pressure marker, at X-ray wavelength 0.4131 Å, with a non-deuterated NQ:NP sample prepared by the same method as in the neutron experiment. In this X-ray study, NQ:NP was observed to undergo two phase transitions - one at 1.18 GPa, and one at 8.18 GPa, as shown in Figure 4.14. Unfortunately structures were not obtained for the high-pressure forms.

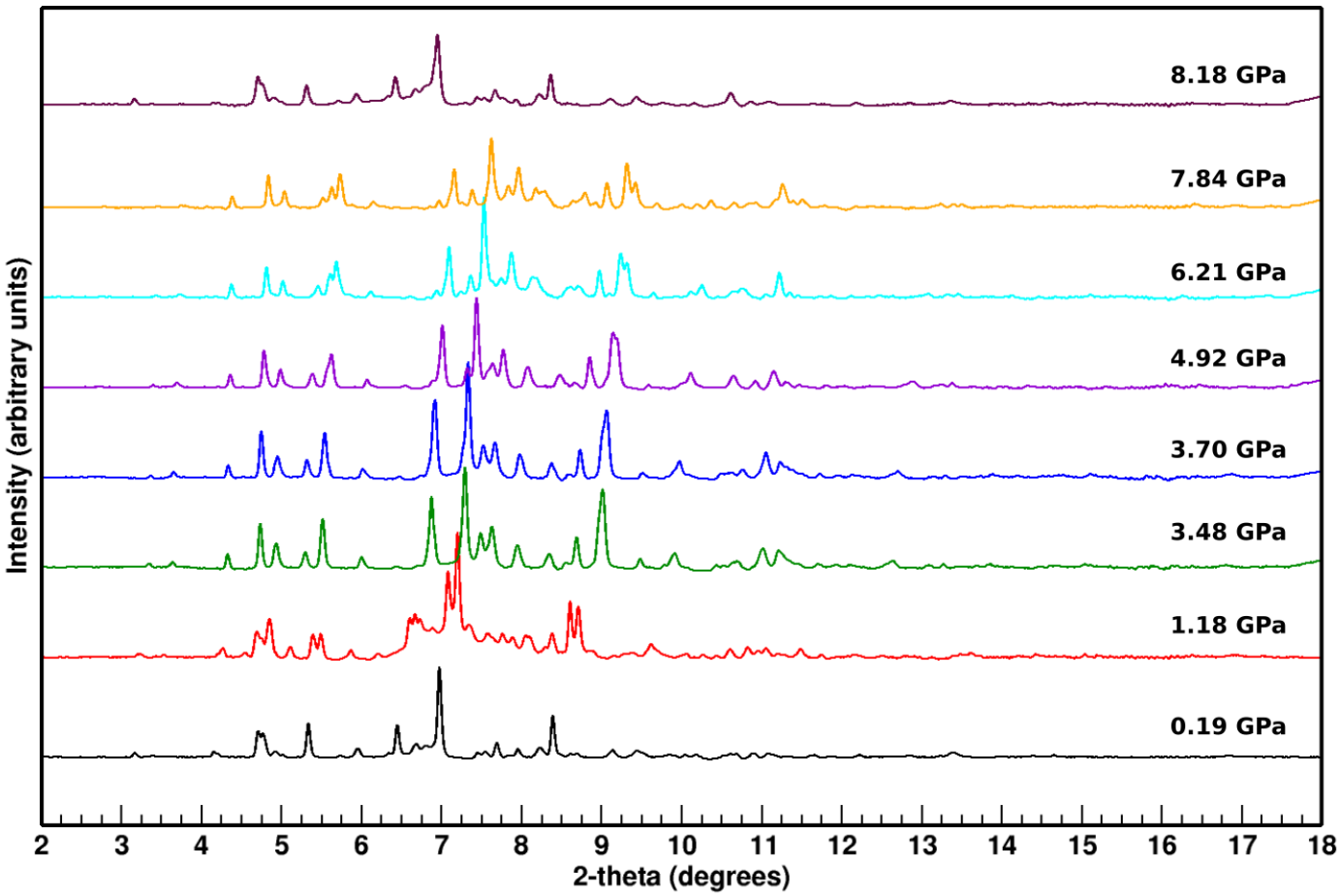

Figure 4.14: Synchrotron X-ray powder diffraction patterns of NQ:NP using the I-15 instrument at the Diamond Light Source (wavelength = 0.4134 Å). Two potential phase transitions can be seen in this progression of patterns - one at 1.18 GPa, and one at 8.18 GPa.

In this neutron experiment, however, NQ:NP was not observed to undergo any phase transitions over the studied pressure range. This can be inferred from a lack of discontinuities in the pressure-volume curve, and a lack of significant changes to peak positions and intensities as a function of pressure, as seen in the plot in Figure 4.15.

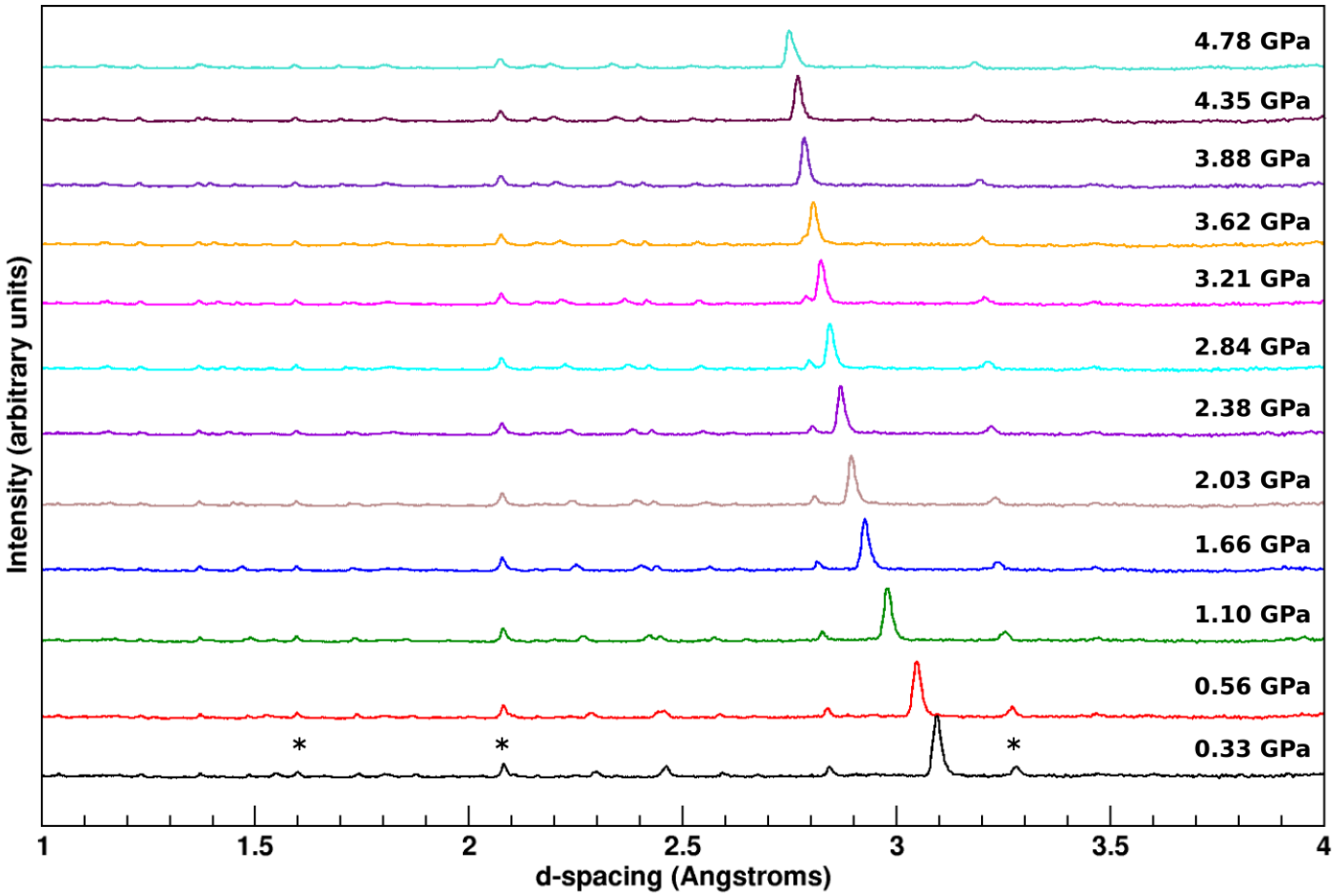

Figure 4.15: Selected neutron powder diffraction patterns of NQ:NP across the entire pressure range of this experiment. Peaks resulting from the lead or anvils (i.e. *non-sample* peaks) are asterisked - these do not move as significantly with increasing pressure.

There are some potential reasons for this discrepancy between the two experiments. It may be that this nitroguanidine co-crystal is more sensitive to the intense X-rays produced by the synchrotron and could have suffered radiation damage while exposed in the beam at Diamond [14, 15]. Alternatively, the presence of deuterium in place of hydrogen may suppress a phase transition that would otherwise be more favourable with the material in its non-deuterated form [16].

4.2.2 NQ:DNP

Below 1.22 GPa

For the NQ:DNP system, the *a*- and *c*-axes decrease at a similar rate relative to each other as a function of pressure, with the *b*-axis being markedly less compressible over this range. In Figure 4.17, the trend in the lattice parameters (normalised) can easily be seen. Un-normalised values can be found in Table 4.6. Figure 4.16 shows the waterfall plot of diffraction patterns collected during this experiment. Figure 4.18

shows the experimentally-derived equation of state overlaid atop the pressure-volume curve. An obvious change in the diffraction pattern of this compounds can be seen beginning at 0.82 GPa - this is the onset of a phase transition, which completes at 1.22 GPa. For this reason, values in the aforementioned figures are only shown up to 0.82 GPa.

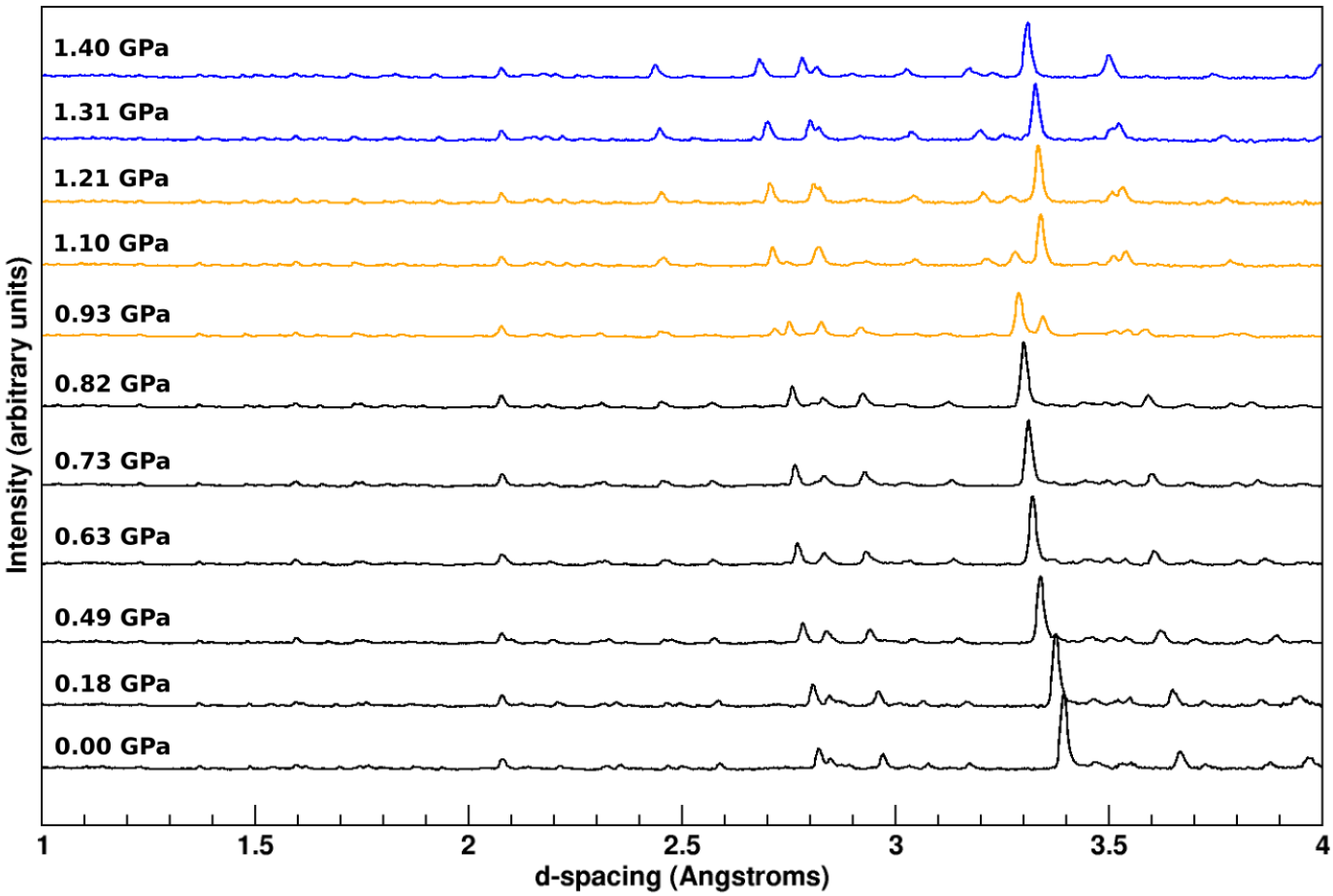

Figure 4.16: The progression of NQ:DNP patterns with increasing pressure, showing a potential phase transition between 0.93 and 1.22 GPa. The ambient-pressure phase is shown with black traces; the mixed phase region in orange; and the high-pressure polymorph in blue.

As the first pressure point in this system was found to be at 0.00(1) GPa (with 6 tonnes applied load), this was deemed close enough to ambient pressure to be used for normalisation of the subsequent high-pressure data points. The lattice parameters obtained at this pressure are given in Table 4.5

Table 4.5: Lattice parameters and refinement factors for NQ:DNP at 0.00(1) GPa. These parameters were subsequently utilised for normalisation of the experimental neutron diffraction data up to 0.82 GPa.

Parameter	Value
a	9.673(6) Å
b	11.367(1) Å
c	10.841(7) Å
β	113.31(1) °
V	1094.8(2) Å^3
R_p	4.03 %
R_{wp}	3.95 %
Temperature	298 K
Space group	$P2_1/n$

As only a limited set of data points were collected before the onset of the phase transition, extensive Rietveld refinement was only possible for the data sets up to 0.82 GPa. In the mixed-phase region beyond this pressure, the high-pressure behaviour begins to interfere with refinement of the ambient-pressure phase, preventing the determination of accurate lattice parameters. With the limited set of lattice parameters available for the ambient phase of NQ:DNP, attempts to fit a 3rd order Birch-Murnaghan equation of state were unsuccessful, and so instead a 2nd order Birch-Murnaghan equation of state was used.

The bulk modulus (B_0) was determined from the equation of state to be 14.4(2) GPa, with the initial volume fixed to that stated in Table 4.5. As this was a 2nd order Birch-Murnaghan EOS, the pressure derivative B' was fixed at 4.0. No bulk moduli have been determined for NQ or DNP. However, the bulk modulus for the co-crystal lies within the typical range for molecular organic solids [17].

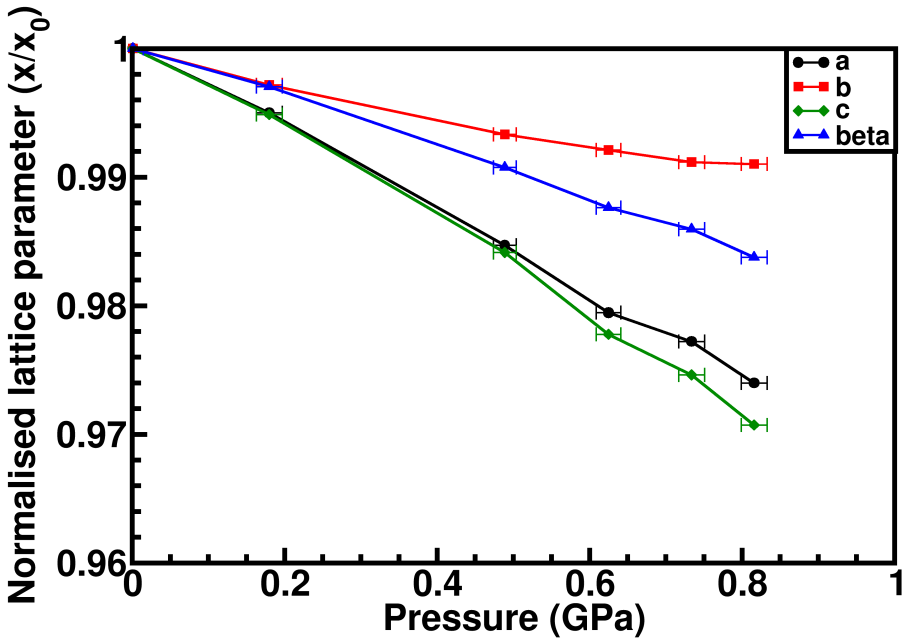

Figure 4.17: Normalised lattice parameters for NQ:DNP as a function of pressure up to 0.82 GPa. These have been normalised to the initial values in Table 4.5. Error bars on the y-axis, as calculated from the Rietveld refinement, are too small to display on this scale.

Table 4.6: Lattice parameters for the ambient-pressure polymorph of NQ:DNP at each pressure point during this experiment up to the onset of the phase transition, along with associated refinement factors.

Pressure (GPa)	a (Å)	b (Å)	c (Å)	β (°)	V (Å^3)	R_p (%)	R_{wp} (%)	GoF
0.00(1)	9.673(6)	11.367(1)	10.841(7)	113.31(1)	1094.8(2)	4.03	3.95	0.96
0.18(2)	9.625(5)	11.335(1)	10.786(6)	112.97(1)	1083.4(1)	3.92	3.80	0.92
0.49(2)	9.525(4)	11.292(1)	10.669(5)	112.26(1)	1062.9(1)	3.51	3.50	1.19
0.63(2)	9.475(5)	11.278(1)	10.600(6)	111.91(1)	1050.9(1)	3.96	4.05	1.37
0.73(2)	9.453(5)	11.267(1)	10.566(6)	111.72(1)	1045.5(1)	3.51	3.68	1.67
0.82(2)	9.422(5)	11.265(1)	10.524(7)	111.47(1)	1039.5(2)	4.45	4.37	2.50

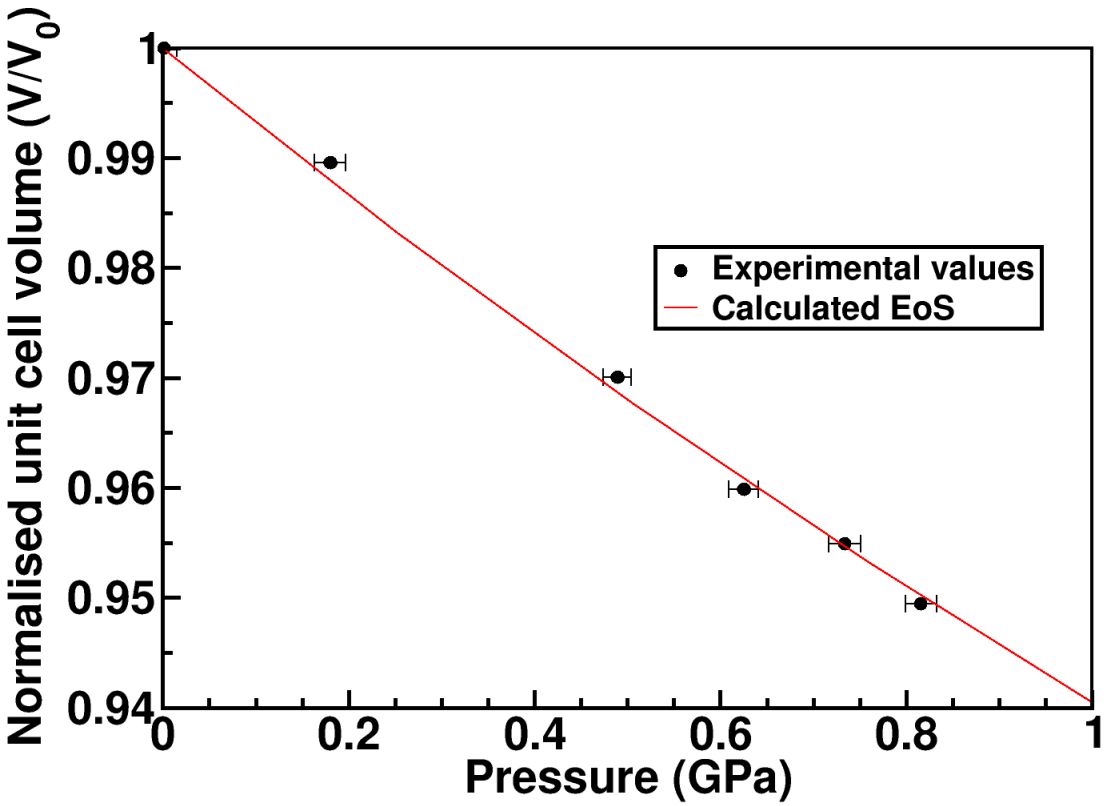

Figure 4.18: Second-order Birch-Murnaghan equation of state for NQ:DNP, with normalised experimental volume data, as a function of pressure.

The almost equal response of the *a*- and *c*-axes to hydrostatic compression can be rationalised by consideration of the arrangement of the layers in the structure. The herringbone-style layering (cf. Figure 4.5) is not parallel to a single axis, unlike the sheet-type layering seen in NQ:NP. Instead, the layers lie along the diagonals between the *b*- and *c*-axes. As the structure is compressed, the gaps between these layers preferentially reduce in size. Since the inter-layer spacing is primarily aligned with the *a*- and *c*-axes, that these axes will decrease in length more rapidly than the *b*-axis when pressure is applied.

The principal axis compressibilities for the system were also calculated using PASCal [13]. How these relate to the crystallographic axes is indicated in Table 4.7. Compressibility values for each axis are also given in the same table.

Table 4.7: The relation between principal axis compressibilities and the crystallographic axes, with each crystallographic axis' contribution being represented on a scale from -1 to 1. Associated compressibility values for each principal axis, as calculated by PASCal, are also given.

Principal axis	a component	b component	c component	Compressibility (TPa^{-1})
X_1	-0.7034	0.0	0.7108	49.133(4.970)
X_2	0.0	-1.0	0.0	1.893(18.670)
X_3	0.764	0.0	0.646	6.473(1.652)

Only three intermolecular hydrogen bonding interactions are present in the NQ:DNP system. Of these three interactions, only one contact changes in length by any appreciable amount over the studied pressure range prior to the phase transition - the O7...D27 contact, shown in Figure 4.19, which decreases by 0.148 Å (up to 0.816 GPa) from 2.424(17) to 2.276(20) Å. This contact is between an oxygen on a nitro group on DNP, and a deuterium on the amino group of an adjacent NQ molecule. The other two contacts - O1...D15 and O8...D26 - only change by 0.027 and 0.002 Å , respectively. O1-D15 represents an interaction between adjacent DNP molecules - the deuterium on one interacting with the pyridone oxygen on another; while O8...D26 represents another DNP-nitro to NQ-amino interaction.

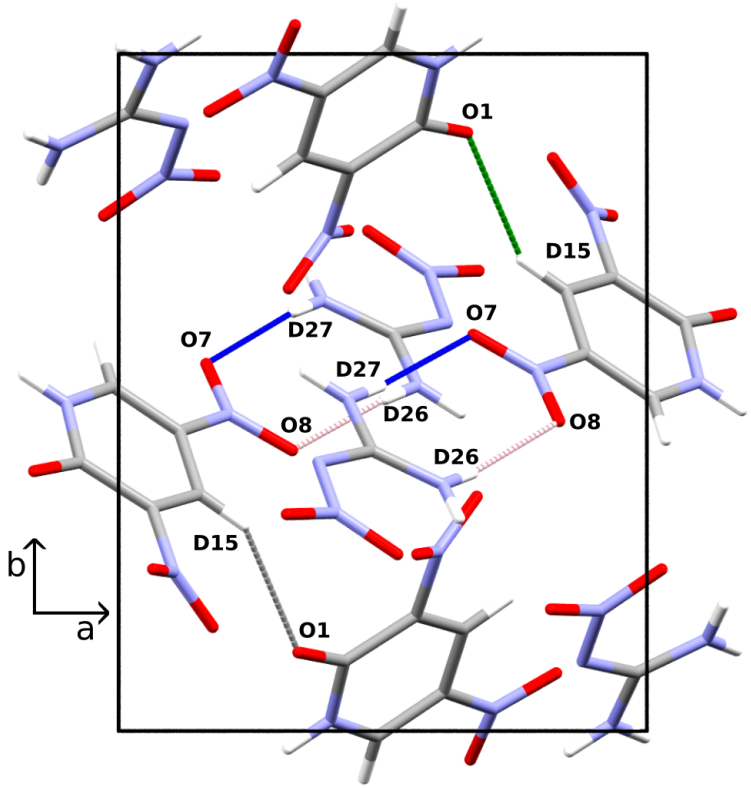

Figure 4.19: The three intermolecular hydrogen bonding interactions in NQ:DNP, viewed along the *c*-axis. (c.f. Figure 4.4). The most-compressible contact, O7...D27 is highlighted in blue; with the other two contacts, O1...D15 and O8...D26, in pink and grey respectively.

Interestingly, the O7...D27 and O8...D26 contacts are parallel to each other, and exist between the same two molecules - involving alternate oxygens on the DNP nitro group, and different amino groups on the adjacent NQ molecule. However, while O7...D27 decreases over the studied pressure range, O8...D26 essentially does not. This suggests that with increasing pressure the molecules will begin to rotate with respect to each other, pushing the O7 and D27 atoms closer together, while maintaining the distance between O8 and D26. It is possible the individual amino or nitro groups (or rather, their N-D or N-O bonds) could rotate as opposed to the entire molecules, but investigating this would require removing the rigid bodies from the refinements and employing a more complex system of individual constraints and restraints.

Above 1.22 GPa

When the pressure exerted on the sample reached 0.9 GPa, NQ:DNP appeared to undergo a rather sluggish phase transition. This transition was fully completed by 1.22 GPa. The transition can be clearly seen by a change in the diffraction pattern, as shown previously in Figure 4.16.

The structure of this high-pressure form has thus far escaped elucidation. Attempts have been made to index the high-pressure pattern using DICVOL06 [18], DASH [19], Fox [20], McMaille [21], and GSAS-

II. All methods produced numerous different combinations of lattice parameters with a wide variety of magnitudes. The only common factor to all the results was the prevalence of a monoclinic crystal system. The overall average unit-cell volume was approximately 2500 Å^3. None of the resulting cells from any indexing method gave a chemically-sensible result when subjected to simulated annealing (using DASH or GSAS-II) or charge flipping methods (using GSAS-II).

Next steps would be to try and acquire some X-ray data of the high-pressure phase in a synchrotron experiment. Attempting an indexing with this X-ray data may narrow down the potential volume range (which spans from $\sim$ 700 Å^3 to 5000 Å^3 in neutron indexing attempts), and potentially identify a space group. This could then be used to limit the range of indexing for the neutron data, which could itself be used to narrow down the actual structural elements - the neutron data in theory being more suited for determination of atomic positions. Given the increase in beta angle with increasing pressure, one potential structure for the high-pressure phase is that the two layers slide past each other, forming a potentially larger or smaller unit-cell depending on the extent of this slide motion. Further future steps and directions are discussed in Chapter 6.

4.3 References

[1] J. Thiele, *Justus Liebig's Annalen der Chemie*, 1892, **270(1)**, 1–63.

[2] T. Gibbs and A. Popolato, *LASL Explosive Property Data*, University of California Press, 1980.

[3] P. L. Coster, "Unpublished internal work", , 2013.

[4] R. Murmann, R. Glaser and C. L. Barnes, *Journal of Chemical Crystallography*, 2005, **35(4)**, 317–325.

[5] O. V. Dolomanov, L. J. Bourhis, R. J. Gildea, J. A. Howard and H. Puschmann, *Journal of Applied Crystallography*, 2009, **42(2)**, 339–341.

[6] G. Sheldrick, *Acta Crystallographica Section A*, 2008, **64**, 112–122.

[7] O. Arnold, *Nuclear Instruments and Methods in Physics A*, 2014, **764**, 156–166.

[8] C. L. Bull, N. P. Funnell, M. G. Tucker, S. Hull, D. Francis and W. G. Marshall, *High Pressure Research*, 2016, **36**, 493–511.

[9] A. C. Larson and R. B. Von Dreele, *General Structure Analysis System. LANSCE, MS-H805, Los Alamos, New Mexico*, 1994.

[10] B. H. Toby, *Journal of applied crystallography*, 2001, **34(2)**, 210–213.

[11] B. H. Toby and R. B. Von Dreele, *Journal of Applied Crystallography*, 2013, **46(2)**, 544–549.

[12] R. J. Angel, M. Alvaro and J. Gonzalez-Platas, *Zeitschrift für Kristallographie-Crystalline Materials*, 2014, **229(5)**, 405–419.

[13] M. Cliffe and A. Goodwin, *Journal of Applied Crystallography*, 2012, **45**, 1321–1329.

[14] E. Garman, *Current Opinion in Structural Biology*, 2003, **13**, 545–551.

[15] C. Nave and M. Hill, *Journal of Synchrotron Radiation*, 2005, **12**, 299–303.

[16] D. Guard-Friar, C.-H. Chen and A. S. Engle, *Journal of Physical Chemistry*, 1985, **89**, 1810–1813.

[17] S. Vaidya and G. Kennedy, *Journal of Chemical Physics*, 1971, **55**, 587.

[18] A. Boultif and D. Louër, *Journal of Applied Crystallography*, 1991, **24(6)**, 987–993.

[19] W. I. David, K. Shankland, J. van de Streek, E. Pidcock, W. S. Motherwell and J. C. Cole, *Journal of applied crystallography*, 2006, **39(6)**, 910–915.

[20] V. Favre-Nicolin and R. Černỳ, *Journal of Applied Crystallography*, 2002, **35(6)**, 734–743.

[21] A. LeBail, *Powder Diffraction*, 2004, **19(3)**, 249–254.

Chapter 5

In situ study of Resonant Acoustic Mixing

As described in Chapter 2, Resonant Acoustic Mixing (RAM) is a low-frequency acoustic agitation technology, designed to offer various processing capabilities for a range of materials. While various studies have been reported that explore the applications of RAM technology and how it can make improvements to existing supply chains and manufacturing methods within the energetic materials industry, few investigations have been conducted into the RAM process itself. Beyond basic information given in a technical white paper by ResoDyn Industries describing microscopic mixing zones [1], nothing is known about how specific processes such as co-crystallisation occur within the RAM environment.

Initial experiments were performed in 2014-15 by the author as part of an MSc dissertation, exploring how mixing capabilities varied with disparities in particle size [2]. These showed (from SEM and electron diffraction analysis) that mixing on the microscopic level between metal powders was enhanced when the components were of similar particle size. As the particle sizes became more disparate, the mixing became less uniform on the microscopic level [3].

The first *in situ* powder diffraction study of co-crystallisation under RAM conditions was undertaken in 2016 at the European Synchrotron Radiation Facility (ESRF). A LabRAM Mixer was mounted on the ID31 instrument, and synchrotron X-rays used to study the co-crystallisation of carbamazepine and nicotinamide over periods of up to 15 minutes [4], showing that through Rietveld refinement of each X-ray 'snapshot', the progression of the reaction could be followed through observing changes in the diffraction pattern and refining phase fractions appropriately.

However, synchrotron radiation is not ideal in all cases. Certain energetic materials (such as CL-20) can decompose if exposed to intense X-ray beams, even over short periods of the order of minutes. Moreover, to maintain an efficient use of limited beamtime, it is less desirable to study chemical processes that have longer timescales *in situ* using a synchrotron. For these reasons, it was proposed to investigate whether neutron powder diffraction was an experimental technique that could be used for *in situ* monitoring of the RAM process. This could also give the added advantage of providing a new sample environment at the ISIS Neutron Source for the study of samples under high G-force conditions using neutron powder diffraction.

A number of instruments at the ISIS Neutron Source were investigated for their suitability to "host" a RAM

mixer for this proof-of-concept study. The PEARL instrument was chosen on account of sufficient space on the instrument to accommodate a suitable d-spacing range, resolution, and high flux for the proposed diffraction experiments.

5.1 Experimental

Adaptation of the RAM mixer for the neutron instrument

Having identified the most appropriate instrument, it became apparent that significant modifications were required to be made to the standard RAM mixer in order to enable it to operate in the PEARL sample environment. The main hurdle in adapting the RAM for use on PEARL was the fact that the mixer would need to be loaded upside-down into the PEARL instrument tank. This was due to the arrangement of the detectors on PEARL; since they are arranged on the bottom half of the instrument, the mixer itself presents an obstacle to any diffracted neutrons reaching the detectors if it were positioned normally.

Coincidentally, the diameter of the LabRAM mixer is quite similar to that of the opening in a standard vacuum tank employed on PEARL. It was decided that the optimum configuration would be to allow the mixer to rest on the opening of the vacuum tank, and extend the sample environment downwards and into the neutron beam, as shown diagramatically in Figure 5.1.

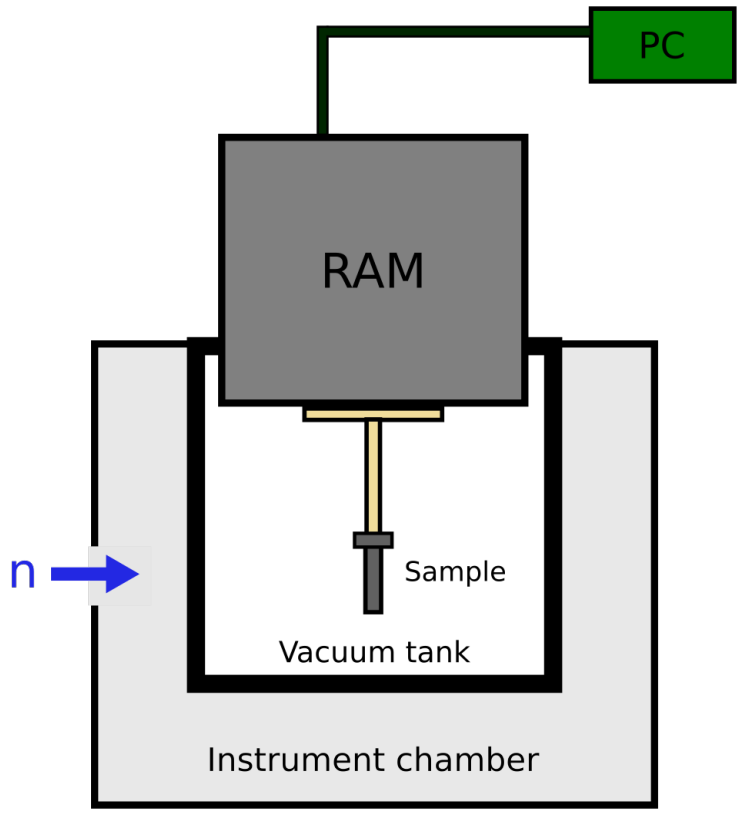

Figure 5.1: Schematic showing the RAM mixer mounted on the PEARL instrument.

After manually inverting the mixer and performing a test to confirm that the mixer could still function in an inverted arrangement, a metal adapter ring was designed to allow the mixer to rest on the opening of the vacuum tank while in operation. This fitted into the lip of the mixer, also serving the function of activating the mixer's hardware interlock button, enabling the mixer to function without its usual perspex hood.

Next, a new sample holder had to be developed with three criteria: (i) be able to support a standard vanadium can sample container; (ii) be able to provide the necessary vertical displacement to place the sample material in the neutron beam; and (iii) be transparent enough to neutrons so as not to swamp any sample diffraction with diffraction from the sample holder. To that end, a new sample holder was designed - this was modelled on the existing "candlestick" holders used by ISIS instruments for vanadium cans. The new sample holder was designed to screw into the existing mounting holes on the RAM's baseplate, while providing enough length to place any attached sample within the neutron beam of the instrument. The sample holder was primarily made from PEEK™, with the ability to screw a vanadium can into an opening at the top. As most vanadium cans at the ISIS Neutron Source share commonly-sized screw holes and threads, this would allow a variety of can sizes to be used with the mixer if needed. This new sample holder is shown in Figure 5.2.

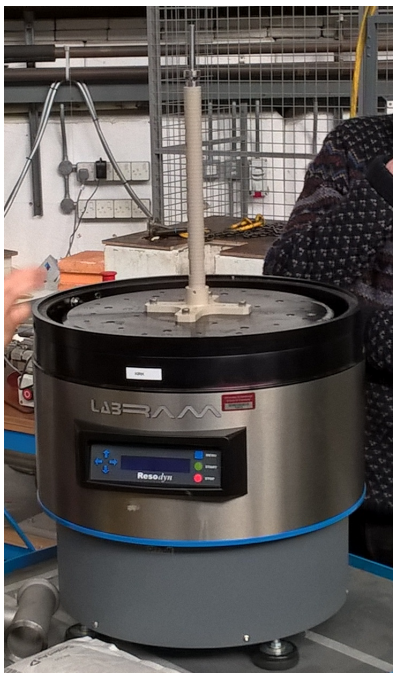

Figure 5.2: The new sample holder, designed to allow samples to extend into the neutron beam.

With these modifications completed, the mixer was now able to be placed into the instrument using the standard PEARL lifting and craning apparatus. By attaching lifting tackle to the requisite holes on the PEARL vacuum tank, the mixer could be lifted and lowered into the instrument without the requirement for a dedicated mounting frame, as shown in Figure 5.3.

Figure 5.3: Lowering of the adapted RAM mixer into the PEARL instrument.

***In situ* study of urea:oxalic acid**

This study focused on the co-crystallisation process between urea and oxalic acid, which forms 1:1 and 2:1 co-crystals of the two materials. Previous *ex situ* diffraction work performed at Edinburgh by Jessica Cooney (with guidance from the author)[2] showed that the RAM mixer can, in a solvent-drop-assisted reaction, produce large quantities of the 2:1 U:OXA co-crystal on a slow enough timescale ($\sim$ 1 hour) for neutron diffraction to track.

Stoichiometric quantities of lightly-ground urea-d_4 and oxalic acid-d_2, in a 2:1 molar ratio (0.8 g and 0.5 g respectively), were combined in a standard vanadium can of diameter 8 mm. The can was then attached to the sample holder in the upright position. The RAM mixer was subsequently inverted, and lowered into the PEARL instrument tank. Following a small amount of instrument calibration, the mixer was switched on at an acceleration setting of 40 G for one hour.

[2]Performed by Ms Cooney as part of an internal undergraduate project - not currently published.

Neutron diffraction data were collected in five-minute blocks (12.5 μA per block). Data were collected over a d-spacing range of 1 - 4 Å in each experiment. The region of less than 1 Å was excluded, on account of the very many overlapping low-intensity Bragg reflections in this region hindering subsequent Rietveld refinements.

As with the high-pressure experiments performed on the same instrument, the in-house Mantid software package was used to normalise the collected data. This also applied attenuation corrections from the instrument environment as appropriate [5, 6]. Phase fractions were obtained for each data block through Rietveld refinement, performed using GSAS with EXPGUI [7, 8]. Existing crystal structures of urea, oxalic acid and the co-crystal were used as starting points for refinements [9, 10, 11].

Rietveld refinements proceeded by first refining the background of the pattern using a shifted Chebyschev function with 12-16 terms in the background function. The lattice parameters were then allowed to refine with high damping applied, along with the component phase fractions. Finally the sigma-1 and gamma-1 profile functions of the pattern were allowed to refine until the most optimally-achievable R-factors and chi-square were achieved.

A second experiment was performed with a larger vanadium can of diameter 16 mm. The quantities of reagents were increased to compensate for the larger sample volume, while the RAM setup remained otherwise the same, i.e. operating at the same mixer acceleration over the same timescale. Data collection and analysis were performed in the same manner as in the first experiment.

In situ study of glycine:oxalic acid

The second study focused on a similar co-crystallisation process, this time between glycine and oxalic acid. Two potential products result from this reaction - a 2:1 co-crystal of glycine and oxalic acid (2G:OXA); and a 1:1 co-crystal of glycine and oxalic acid (1G:OXA). *Ex situ* diffraction work performed at Edinburgh by Adam Michalchuk in advance of the synchrotron experiments showed that these two materials also co-crystallised in a Resonant Acoustic Mixing environment on a slow enough timescale to be appropriate for neutron powder diffraction analysis.

In a similar manner to the aforementioned urea:oxalic acid experiment, stoichiometric quantities of glycine-d_5 and oxalic acid-d_2 were combined in a standard vanadium can of diameter 12 mm. This was sealed and attached to the sample holder, with the RAM in its normal upright position. The mixer was then inverted and inserted into the instrument tank. Following initial calibrations, the mixer was switched on at a set acceleration of 50 G for one hour.

As before, neutron data were collected in five-minute blocks over a d-spacing range of 1 - 4 Å, and normalised

/ corrected using Mantid. Phase fractions for each block were determined through Rietveld refinement, again using GSAS with EXPGUI. Existing crystal structures of glycine, oxalic acid and the co-crystals were used as starting points for refinements [10, 12, 13, 14], using the same Rietveld refinement procedure as for the urea:oxalic acid experiments. An example fit is shown in Figure 5.4.

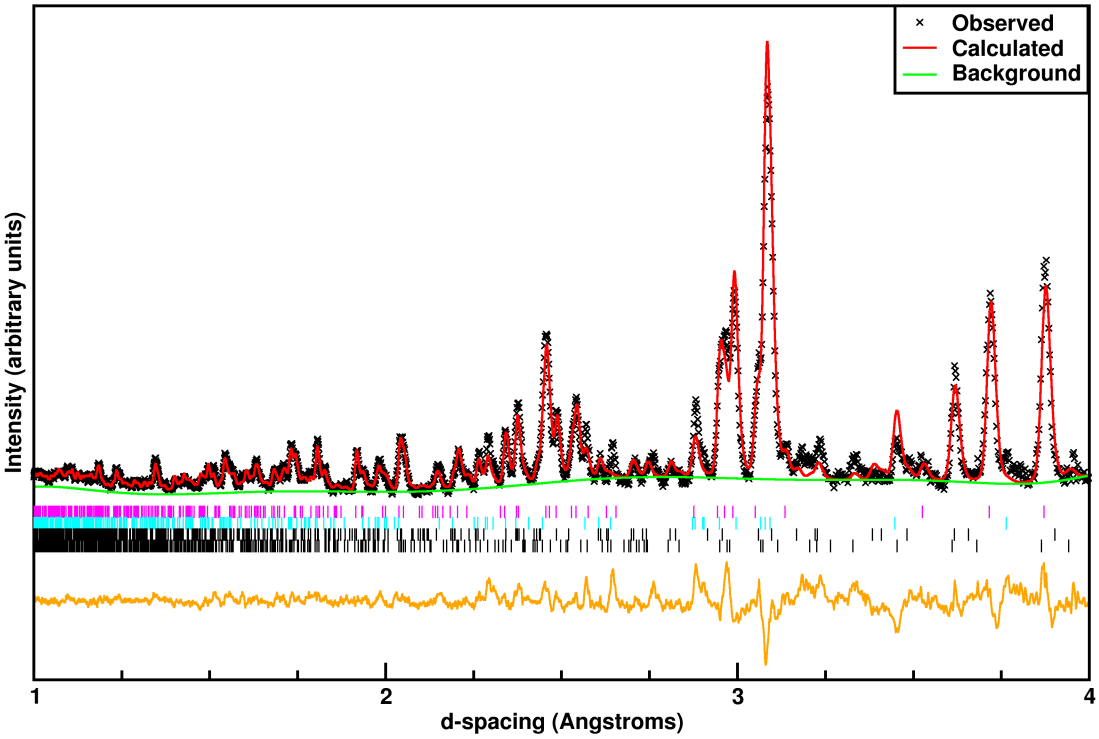

Figure 5.4: Example Rietveld refinement of G:OXA, from 10 minutes after the start of mixing. The Rietveld refinement model is denoted in red, with black crosses representing experimental data points. The orange line denotes the difference between the model and experimental data. The tickmarks, from top to bottom, show Bragg reflections from urea; oxalic acid; the 2G:OXA product, and the 1G:OXA product respectively.

A second experiment was performed using an identical vanadium can and the same quantities of reagents, but with the mixer operating at the lower acceleration setting of 30 G. Data collection and analysis were handled in the same manner as for the 50 G experiment.

Deuteration of individual co-formers

Two of the three co-formers used in this experiment were deuterated using a combination of reflux and recrystallisation.

Materials utilised in preparing oxalic acid-d_2 and urea-d_4 were as follows. Oxalic acid dihydrate [$(CO_2H)_2.2H_2O$, "OAD", purchased from Sigma-Aldrich]; urea (CH_4N_2O, purchased from Acros Organics); and deuterium oxide (D_2O, 99.9 %, purchased from Sigma-Aldrich).

A quantity of either urea or OAD was dissolved in a 100 ml round-bottomed flask using the minimum

possible amount of D_2O ($\sim$ 50 ml). The flask was then heated (with a condenser) to $\sim$ 80 °C and allowed to stir until all of the solid material had dissolved.

Once the co-former had fully dissolved, the flask was left to stir under heat for three hours. Following this, the mixture was allowed to cool to room temperature (with the flask sealed to reduce exposure to atmospheric moisture), and the white co-former material began to precipitate out. The respective urea or oxalic acid solid was removed by vacuum filtration. The recovered urea was dried overnight in a vacuum desiccator, while the oxalic acid was only lightly dried before being stored (to prevent dehydration and conversion to anhydrous oxalic acid). Deuterated glycine (glycine-d_5) was purchased from Sigma-Aldrich.

5.2 Results and Discussion

Urea:oxalic acid

For the first choice of can size (8 mm), the co-crystallisation of urea and oxalic acid was observed, but conversion was only partial. The progression of selected diffraction patterns over the course of the experiment is shown in Figure 5.5. The key characteristic peaks of urea were observed to decrease in intensity relative to other peaks in the pattern. However, from 40 minutes onwards, there were no further changes in the pattern. A plot of the phase fractions of urea, oxalic acid and the 2:1 U:OXA co-crystal, expressed in mole-percentages, is displayed in Figure 5.6, with values given in the accompanying Table 5.1.

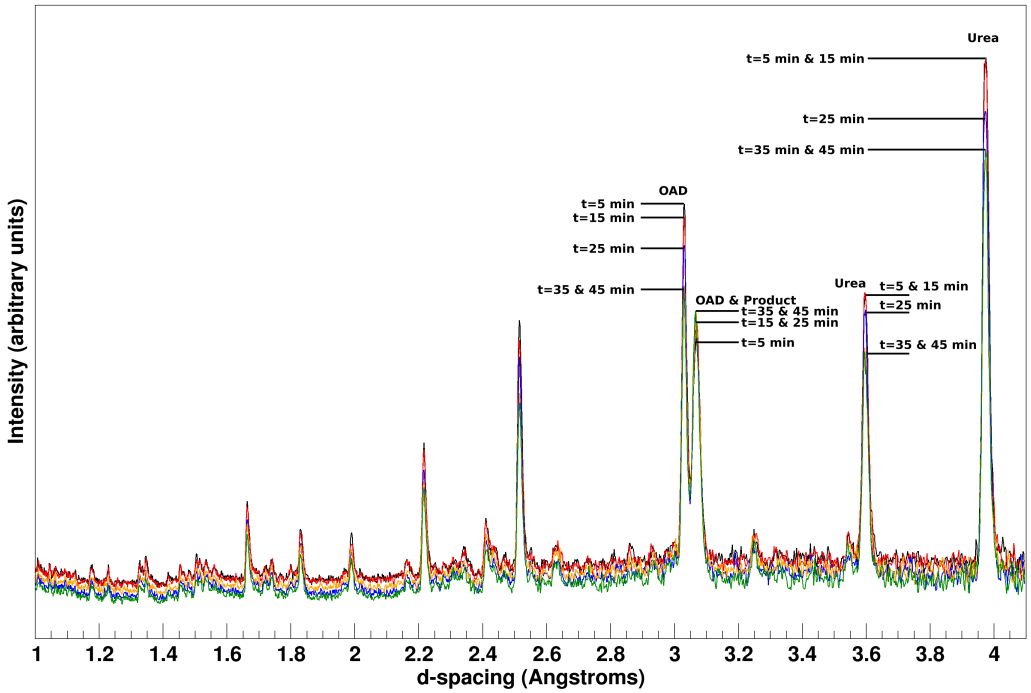

Figure 5.5: Selected diffraction patterns of the U:OXA reaction in the 8 mm can experiment. Time increments after the start of mixing are as designated on the graph - 5 min in black, 15 min in red, 25 min in blue, 35 min in orange, and 45 min in green. Key peaks are indicated. "OAD" refers to oxalic acid dihydrate starting material.

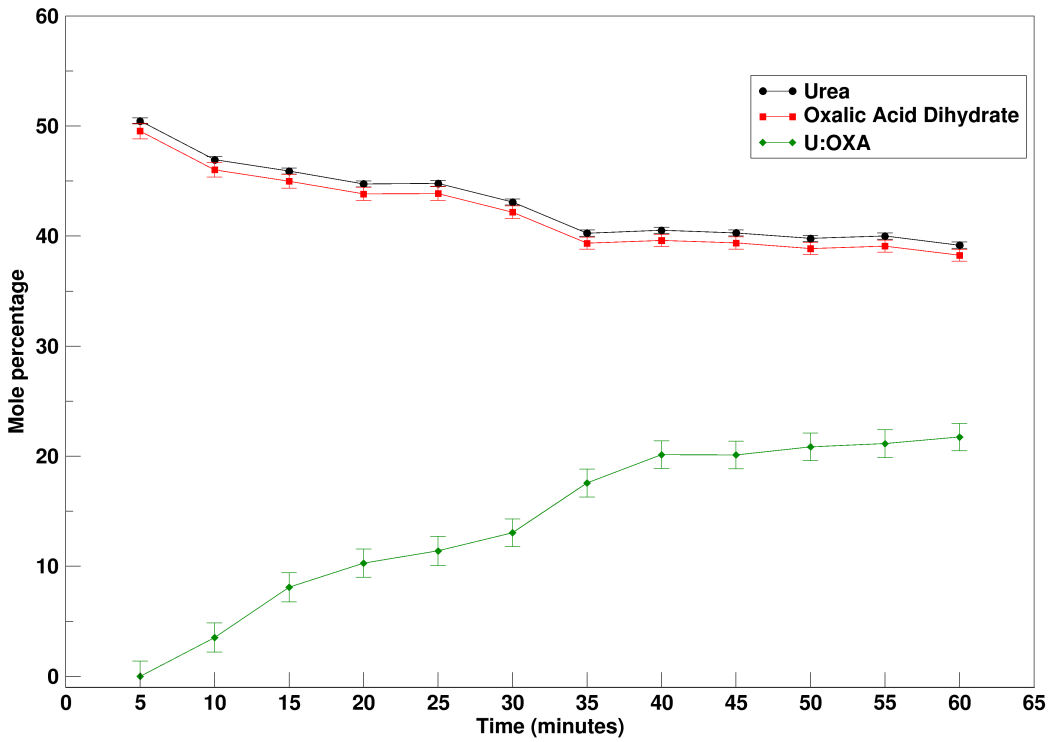

Figure 5.6: The phase fractions of the three components in the formation of 2:1 U:OXA, displayed as mole-percentages, for the experiment using an 8 mm vanadium can.

Table 5.1: Numerical values for mole percentages of the three components in the U:OXA process, as displayed in Figure 5.6.

Time (min)	Urea Mole%	OAD Mole%	U:OXA Mole%
5	50.5	49.5	0.0
10	46.9	46.0	3.5
15	45.9	45.0	8.1
20	44.7	43.8	10.3
25	44.8	43.9	11.4
30	43.1	42.2	13.1
35	40.3	39.4	17.6
40	40.5	39.6	20.1
45	40.3	39.4	20.1
50	39.8	38.9	20.9
55	40.0	39.1	21.1
60	39.2	38.3	21.7

For the first data point (5 minutes after start of mixing), the phase fractions of urea and oxalic acid were observed to be approximately 50 mol% each. As time progressed, these phase fractions began to reduce, and that of the 2:1 product began to increase. After approximately 40 minutes, the reaction appeared to stall, and the phase fractions of neither the reagents nor the products significantly changed until the end of the collection at 60 minutes.

There are several possible reasons why the reaction ceased to continue after 40 minutes. One explanation is that the reaction had failed to proceed to 100 % completion due to an equilibrium being reached. However, off-line tests and prior kinetic studies (performed by project student Jessica Cooney under guidance from the author) indicated a > 90 % conversion rate from the RAM process and therefore high yields of co-crystal product.

The second possibility is that the size of the vanadium can in the first experiment prohibited sufficient movement and mixing of the two components. When the experiment was repeated with a 16 mm vanadium can, no useable diffraction data were observed during the experiment - indicating there was likely too *much* freedom of movement for the sample material in this case and the volume of material that remained within the neutron beam was insufficient for significant intensity of scattering from the sample to occur. It is possible that a layer of U:OXA may have formed at the interface between urea and oxalic acid particles in

the sample, thereby preventing reaction.

A third possibility is that as the urea and oxalic acid dihydrate co-crystallise, the water of co-crystallisation is released. This is corroborated by the very damp appearance of the material removed from the vanadium can after the experiment. This release of water may have caused agglomeration of the mixture, and so in the relatively narrow 8 mm vanadium can this hindered efficient mixing.

These issues could be mitigated by performing more experiments to determine the optimum size of vanadium can, optimum amount of container headspace, and optimum packing of the urea and oxalic acid within the container, so that the reaction could proceed to full completion.

Glycine:oxalic acid

In the glycine:oxalic acid experiment, an intermediate can size (12 mm) was chosen in a pre-emptive attempt to mitigate the problems encountered in the U:OXA experiments.

With G:OXA, the experiment was again observed to proceed steadily until a certain point, at which any further conversion to product ceased. However, the manner in which this happened varied between the 30 G experiment and the 50 G experiment, according to analysis of the neutron data.

For the 30 G experiment, a progression plot of the diffraction data is shown in Figure 5.7. Phase fractions of each component (glycine, oxalic acid dihydrate, 1G:OXA, and 2G:OXA) are displayed graphically in Figure 5.8 as mole percentages, with numerical values given in Table 5.2.

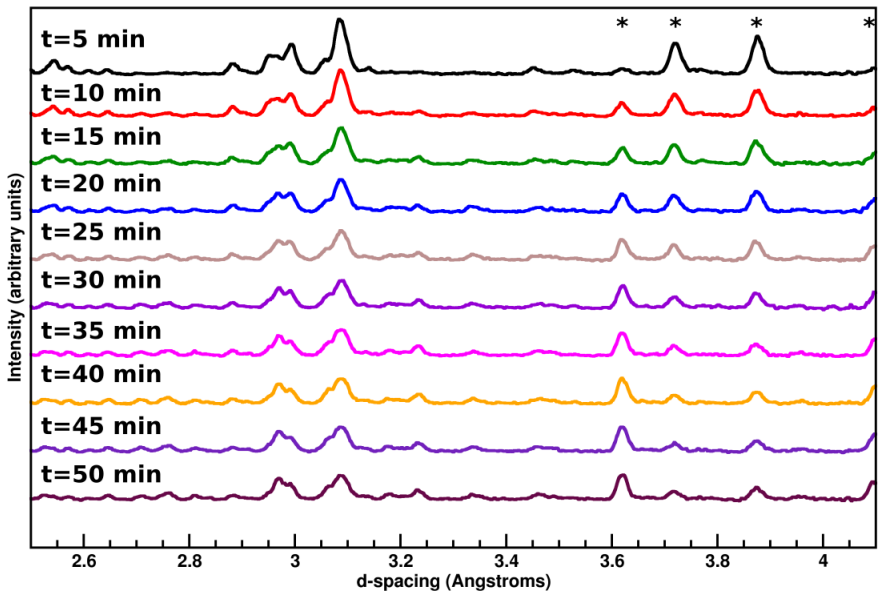

Figure 5.7: The diffraction patterns of the G:OXA reaction collected over each five-minute block at 30 G. The first pattern in the time sequence is at the top, progressing to the final pattern at the bottom in five-minute steps. The d-spacing range has been truncated to that containing the peaks with the most significant intensity. Key peaks have been indicated with asterisks.

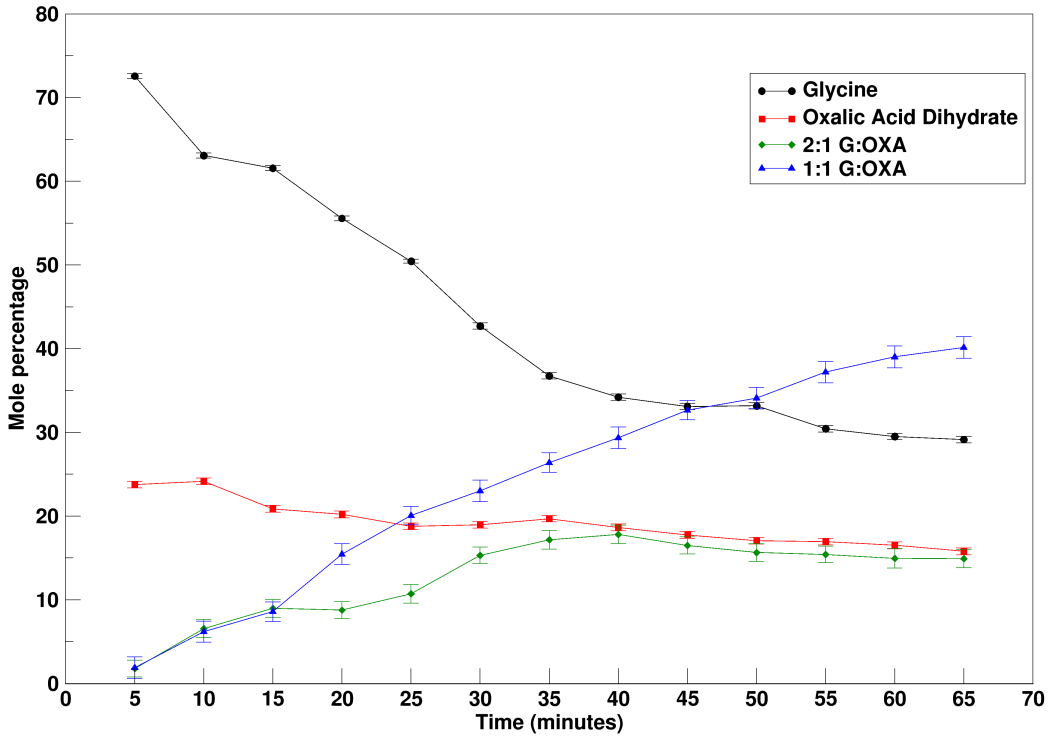

Figure 5.8: The phase fractions of the four components in the G:OXA process, displayed as mole-percentages, in the 30 G experiment.

Table 5.2: Numerical values for mole percentages of the three components in the G:OXA process at 30 G, as displayed in the previous graph.

Time (min)	G Mole%	OAD Mole%	2:1 G:OXA Mole%	1:1 G:OXA Mole%
5	72.6	23.8	1.8	1.9
10	63.1	24.2	6.6	6.2
15	61.6	20.9	9.0	8.6
20	55.6	20.2	8.8	15.5
25	50.5	18.8	10.7	20.1
30	42.7	19.0	15.3	23.00
35	36.8	19.7	17.2	26.4
40	34.2	18.6	17.8	29.4
45	33.1	17.7	16.5	32.7
50	33.2	17.1	15.7	34.1
55	30.4	16.9	15.4	37.2
60	29.5	16.5	15.0	39.0
65	29.1	15.8	14.9	40.2

In the case of the 50 G experiment, the progression of diffraction patterns and mole percentages are displayed

in Figures 5.9 and 5.10 respectively, with numerical values given in Table 5.3.

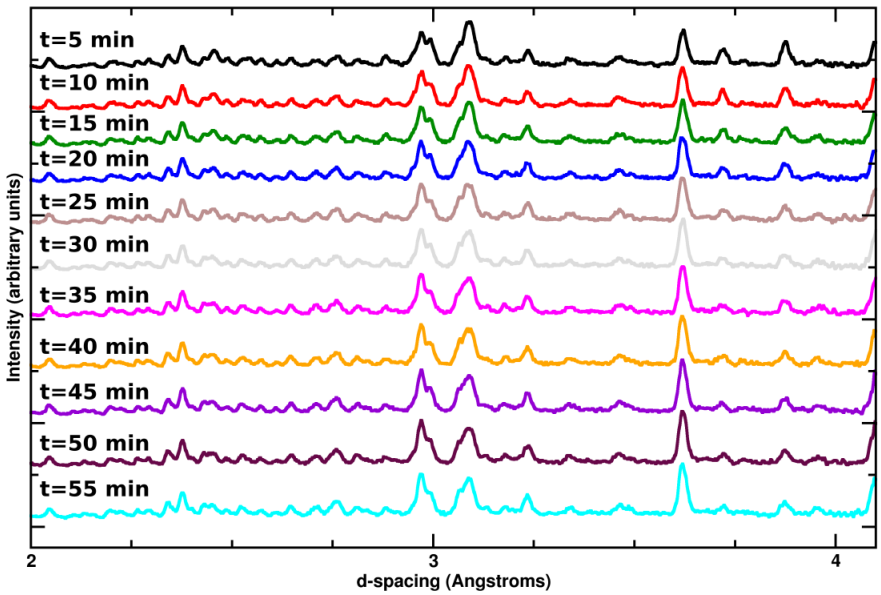

Figure 5.9: The diffraction patterns of the G:OXA reaction collected over each five-minute block at 50 G. The first pattern in the time sequence is at the top, progressing to the final pattern at the bottom in five-minute steps. As before, the d-spacing range has been truncated to the area with the most intense peaks.

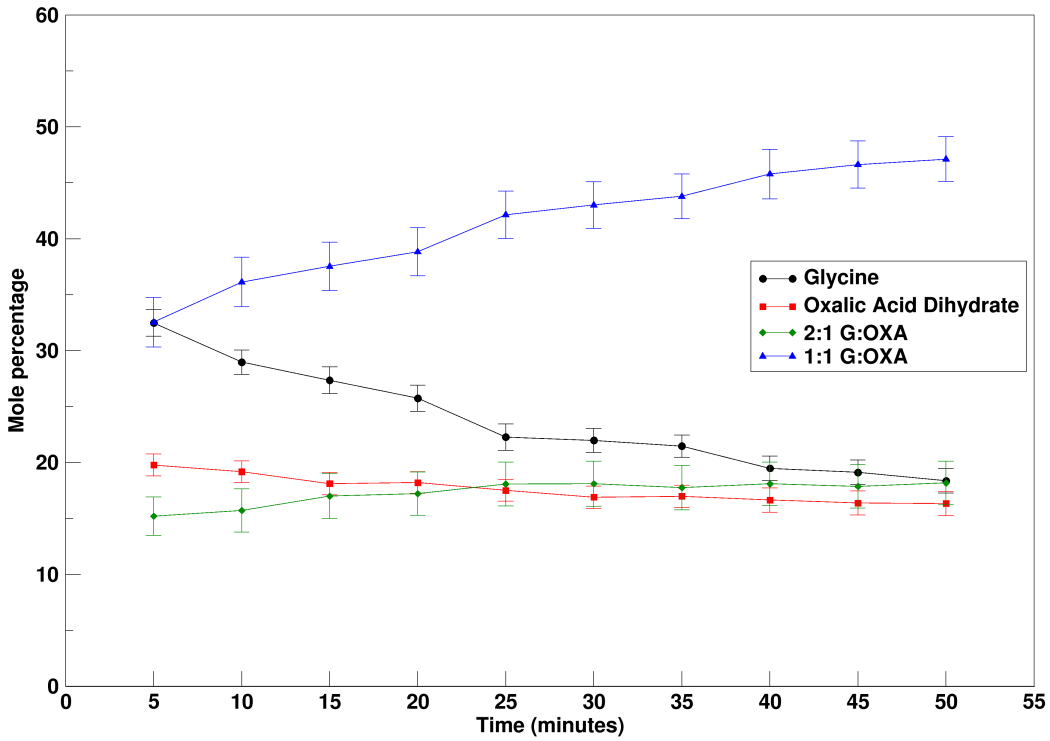

Figure 5.10: The phase fractions of the four components in the G:OXA process, displayed as mole-percentages, in the 50 G experiment.

Table 5.3: Numerical values for mole percentages of the three components in the G:OXA process at 50 G, as displayed in the previous graph.

Time (min)	G Mole%	OAD Mole%	2:1 Mole%	1:1 Mole%
5	32.5	19.8	15.2	32.5
10	29.0	19.2	15.7	36.1
15	27.4	18.1	17.0	37.5
20	25.8	18.2	17.2	38.8
25	22.3	17.5	18.1	42.1
30	22.0	16.9	18.1	43.0
35	21.5	17.0	17.8	43.8
40	19.5	16.7	18.1	45.8
45	19.1	16.4	17.9	46.6
50	18.4	16.3	18.2	47.1

In both the 30 and 50 G cases, the reaction followed similar behaviour to the U:OXA process and stalled after a period of time. This is again in contrast to observed behaviour in prior kinetic tests.

The reasons for this process being observed to halt after 40 - 50 minutes are presumed to be similar to those outlined with the U:OXA experiment. Either the size of the vanadium can does not permit enough movement of the sample, preventing full conversion from occurring. Alternatively the behaviour of the material within the can changes over the course of the experiment due to liberated water, inhibiting movement and hence mixing of the material.

As previously stated, these factors could be mitigated by investigating a greater array of vanadium can sizes and headspace amounts, or by paying closer attention to the packing arrangement of material within the can during loading.

The differences between the 30 and 50 G mole percentage plots are of interest. The 30 G plot appears to be as expected for this experiment. The percentages for urea and oxalic acid reduce as a function of time, while those of the 1:1 and 2:1 products increase with time, greater amounts of the 1:1 product being produced overall. However, in the 50 G plot, the 1:1 and glycine mole percentages start out as almost equal, before quickly diverging as time passes, i.e. the amount of the 1:1 co-crystal increases while glycine decreases. The plot then proceeded mostly as expected - 1:1 and 2:1 products increase in mole percentage (although the 2:1 product increased only marginally), while the percentages of glycine and oxalic acid decreased. There are several possible explanations for this discrepancy.

The first possible reason may be chemical in nature. It is difficult to ascertain what is happening between 0 and 5 minutes. The mole percentages plotted at five minutes represent an average of the neutron data collected between 0 and 5 minutes, rather than a snapshot of what the environment was like at exactly five minutes into the experiment. No "0 minutes" data suitable for refinement were collected within the time available for the experiment. Therefore, it is possible that between 0 and 5 minutes, the reaction rapidly proceeded to such an extent that a significant quantity of the 1:1 co-crystal is formed in those first few minutes, before the reaction process began to slow down or stall due to reasons already stated. However, this is unlikely as prior kinetic tests do not show such behaviour in the G:OXA reaction.

The second possible explanation arises from experimental practicalities. It takes time to load the mixer into the PEARL instrument. Equally it takes time to set up the instrument for collection, and to check the can is secure and its contents are successfully within the neutron beam path. This preparation can range from 15 minutes to 1 hour depending on various factors. Therefore, it is possible that during the time the sample was left idle in the instrument, that it began to react without any input from the RAM.

Offline tests in the laboratory indicated that glycine and oxalic acid dihydrate should not react together when simply left alone. There needs to be either a mechanochemical force, or a solvent, present to start forming G:OXA products. So in theory, the materials sitting in the vanadium can should not have reacted. However, if any water of crystallisation were released as a result of physical action during loading, or if the hygroscopic oxalic acid had absorbed atmospheric moisture during loading of the vanadium can, these could provide an interface to allow for conversion to products. Conversion of some material would cause the release of further water, increasing the size of the interface and accelerating the process. Therefore while the sample is idle awaiting measurement, this reaction could be occurring.

The last explanation is related to the data analysis. A significant flaw in this choice of chemical system is that oxalic acid, the 1:1 product and the 2:1 product all possess significant Bragg reflections in the d-spacing range of 3.6 to 4 Å. The potential translation of sample material during the RAM process, coupled with the slow collection times for neutron diffraction, mean that peak broadening is a significant possibility when diffraction data are only collected and averaged over five-minute increments. Therefore, there is scope for peaks from these three materials to overlap. This then increases the potential for error in the subsequent Rietveld refinements, as GSAS may incorrectly assign more intensity to one phase over another where overlaps and similar peak behaviours occur. So it could be argued that the errors on any weight percentages used to calculate mole percentages may be greater than indicated by the software.

It is difficult to say for certain which of these three possibilities is the root cause. Unless there is a significant block to the movement of material developing within five minutes, it is unlikely that a large rise in amount

of product would occur during the first five minutes, only to be then followed up by a slower increase. The third option - issues with the Rietveld refinement - is plausible, but equally the refinement software did not have issues with any peak broadening occurring in the 30 G sample. There is not a visually-significant difference between the two patterns in terms of broadening.

Therefore the second option - early conversion due to extended loading times with the risk of a cumulative release of water of crystallisation - appears the most likely. This can obviously be mitigated by making efficiencies in the loading process where possible to avoid extended dwell times prior to measurement.

This can be corroborated by looking at the mole percentages of the 50 G experiment. The amount of 1:1 product was observed to increase as the amount of glycine decreased. However, the mole percentages of oxalic acid dihydrate and 2:1 product remained steady with little observed decrease after 15 minutes. The glycine must have combined with oxalic acid to form the 1:1 product, however as the OAD mole percentage is not decreasing, this is not the source of the reacting oxalic acid. Therefore there must be either amorphous or dissolved oxalic acid present in the sample environment to provide a source of oxalic acid. Any dissolved or amorphous oxalic acid would not give any Bragg peaks, and so would be invisible in a neutron diffraction pattern. Any released water of crystallisation would provide a dissolution zone for oxalic acid, yielding the unexpected behaviour in mole percentages seen here.

Similar results were observed for the carbamazepine:nicotinamide (CBZ:NCT) experiment in a prior synchrotron X-ray study. In this experiment, the CBZ:NCT began to form almost immediately after the start of the mixing process, and continued to form steadily over ten minutes until reaching approximately 40 mole %, at which point the reaction appeared to stall. In this case, the physical behaviour of the CBZ:NCT co-crystal - being a more hard-packed and rigid material compared to the free-flowing powders of the co-formers - was believed to hinder further translation of the co-formers, preventing further reaction [4]. This corroborates the finding of this study that free movement of co-formers is essential for a co-crystallisation reaction to proceed in the RAM mixer.

While this work proves that the concept is possible regarding studying RAM *in situ* with neutron diffraction, future work is necessary to optimise the environment. Potential next steps in this regard are detailed in Chapter 6.

5.3 References

[1] ResoDyn Acoustic Mixers, 2010, URL http://www.resodynmixers.com/wp-content/uploads/2009/05/ram-technical-white-paper1.pdf.

[2] K. S. Hope, "Resonant Acoustic Mixing and its applications to energetic materials", Master's thesis, University of Edinburgh, 2015.

[3] K. S. Hope, H. J. Lloyd, D. W. Ward, A. A. Michalchuk and C. R. Pulham, *Proceedings of the 18th NTREM Seminar*, 2015, 134–143.

[4] A. Michalchuk, K. S. Hope, S. R. Kennedy, M. V. Blanco, E. Bolyreva and C. R. Pulham, *Chemical Communications*, 2018, **54**, 4033–4036.

[5] O. Arnold, *Nuclear Instruments and Methods in Physics A*, 2014, **764**, 156–166.

[6] C. L. Bull, N. P. Funnell, M. G. Tucker, S. Hull, D. Francis and W. G. Marshall, *High Pressure Research*, 2016, **36**, 493–511.

[7] A. C. Larson and R. B. Von Dreele, *General Structure Analysis System. LANSCE, MS-H805, Los Alamos, New Mexico*, 1994.

[8] B. H. Toby, *Journal of Applied Crystallography*, 2001, **34(2)**, 210–213.

[9] N. Sklar, M. Senko and B. Post, *Acta Crystallographica*, 1961, **14**, 716–720.

[10] L. Falvello, *CCDC Communication 1456330*, 2016.

[11] S. Harkema, J. Bats, A. Weyenberg and D. Fell, *Acta Crystallographica Section B*, 1972, **28**, 1646–1648.

[12] L. Power, K. Turner and F. Moore, *Acta Crystallographica Section B*, 1976, **32**, 11–16.

[13] R. Chitra and R. Choudhury, *Acta Crystallographica Section B*, 2007, **63**, 497–504.

[14] M. S. Nandhini, R. Krishnakumar and S. Natarajan, *Acta Crystallographica Section C*, 2001, **57**, 115–116.

Chapter 6

Conclusions and future directions

High-pressure studies of CL-20 co-crystals

Two co-crystals of CL-20 and one CL-20 solvate have been studied under high-pressure conditions using neutron powder diffraction.

CL-20:HMX was studied up to 3.5 GPa, and found to compress in an unusually isotropic manner, with roughly similar compression rates and behaviour for all three crystallographic axes. No phase transitions were observed across this pressure range, evidenced by a lack of significant changes in the collected diffraction patterns. Based on analysis of phase fractions, no evidence was observed for any dissociation of the co-crystal into its components.

CL-20:TNT was observed to compress primarily along the inter-layer spacing (b-axis) up to 4.1 GPa, at which point an initiation event occurred. No phase separations or polymorphic transitions were observed in the diffraction data up to this point.

The orthorhombic polymorph of CL-20:HP was found to compress relatively isotropically along all three crystallographic axes up to 5.7 GPa. As with the other two systems, no phase separations or polymorphic transitions were observed across this pressure range; indicating the solvate remains stable up to this pressure.

In terms of future work, one obvious route is to explore even higher pressures with CL-20:HMX and CL-20:HP, to see if any polymorphism is evident in these materials or if they phase-separate under even more extreme conditions. The effects of temperature at elevated pressures could also be investigated to explore more fully the phase diagrams of these co-crystals.

For CL-20:TNT specifically, the pressure region around the initiation event could be explored with a further diffraction experiment. With slower variation in applied load and therefore pressure, it could be determined whether a polymorphic transition precipitates the initiation, or whether the initiation is simply the result of an increase in pressure, or whether the rate at which the pressure is increased plays a role.

The monoclinic polymorph of CL-20:HP is also open to investigation, having not been covered in this work. If large enough (pure) quantities of the monoclinic polymorph can be produced and isolated, a high-pressure diffraction experiment could be conducted to observe the effects of pressure on the structure of this polymorph, in comparison to the orthorhombic polymorph.

CL-20 is susceptible to degradation in the presence of intense X-rays such as those produced by modern synchrotron sources. However, if carried out using laboratory-bsaed diffractometers, a complementary high-pressure X-ray diffraction study may highlight whether the deuteration of co-formers (as in the neutron experiment) has an effect on the observed behaviour of these materials. For example, using non-deuterated TNT may change the initiation pressure of CL-20:TNT.

As mentioned in Chapter 3, standardised impact sensitivity data only exists for CL-20:HMX. Collection of impact sensitivity data for CL-20:TNT and CL-20:HP using a BAM fallhammer (see Chapter 1) could allow comparison of the compressibilities of these materials (and their co-formers) with impact sensitivity, to determine if any correlation may exist between sensitivity and compressibility.

CL-20 is of course not the only explosive in existence, nor is it the only explosive which forms co-crystals. The same research methodology in this thesis could be extended to energetic co-crystals of other explosives or propellants entirely, such as other co-crystals of HMX or TNT.

High-pressure studies of NQ co-crystals

Two co-crystals of nitroguanidine, each with a non-energetic co-former, have been compressed and studied using high-pressure neutron powder diffraction. Both were found to compress most significantly perpendicular to the co-crystal layers.

NQ:NP was studied up to 4.8 GPa. This co-crystal did not undergo any phase transitions or separations over this pressure range. This stands in stark contrast to an earlier synchrotron X-ray diffraction study that indicated two phase transitions in this material, one of which occurs during the range covered by this neutron experiment. The lack of this transition in the neutron experiment may indicate the presence of a deuterium isotope effect in the polymorphic behaviour of this co-crystal, or a reaction to intense synchrotron X-rays.

NQ:DNP was studied up to 4.5 GPa. One phase transition was observed between 0.9 and 1.2 GPa, as evidenced by a distinct change in the collected diffraction patterns with increasing pressure. However, the structure of the high-pressure polymorph has not yet been elucidated, beyond being identified as having a monoclinic unit cell. Determination of the strucutre of this high-pressure polymorph is a clear route for future work. This could be done either through further attempts to solve the structure from the neutron powder data; or by performing a synchrotron X-ray study to gain data over a wider d-spacing range, potentially simplifying any indexing process.

Repeating the NQ:DNP experiment with slower and smaller load steps would also allow for closer observation of this phase transition and better identification of the boundaries of the transition range. This may allow for

better prediction of the resulting high-pressure structure, by carefully following changes in atomic positions in the ambient-pressure polymorph leading up to the transition.

For NQ:NP, a synchrotron X-ray study could be performed with both deuterated and un-deuterated co-formers. If the same phase behaviour occurs as in the neutron experiment, this would point to a significant deuterium isotope effect in the structure of this material. The effects of deuterium on co-crystal structures in general could itself make an interesting study leading on from this. Alternatively, if the phase transition occurs in both ^{1}H and ^{2}H-containing samples, this would point to an X-ray-induced process.

In situ study of Resonant Acoustic Mixing

The first *in situ* neutron powder diffraction study involving a Resonant Acoustic Mixer has been performed. This proof-of-concept project has shown that not only is it possible to observe a Resonant Acoustic Mixing sample environment by neutron diffraction, but that the progress of an experiment within this environment can be followed using neutron diffraction on relatively small timescales.

Urea:oxalic acid and glycine:oxalic acid co-crystallisations using the RAM technique were both successfully followed using neutron diffraction. Both were observed to stall after a period of time, suggesting the RAM co-crystallisation process is highly dependent on the free movement of material within the sample container. Future experiments could take one of two routes - varying the chemical system, or changing physical parameters.

Study of chemical systems that co-crystallise over slower timescales than U:OXA and G:OXA would allow more information to be potentially revealed in the five-minute data blocks, as any very rapid changes will be 'averaged out' as a result of the data collection process and may not be visible in the resulting diffraction patern. As for physical parameters, a range of vanadium can diameters and material packing arrangements should be investigated to determine the optimum size and packing process for good material movement, although this will be dependent on the nature of the materials being studied.

The effect of increasing or decreasing G-force on the co-crystallisation process could also be investigated; and the *in situ* monitoring environment could also be used to study other RAM-based processes beyond co-crystallisation, such as particle coating.

General conclusions

This thesis marks the first published studies of energetic co-crystals under high-pressure conditions; and also marks the first *in situ* neutron diffraction experiment involving Resonant Acoustic Mixing.

In terms of how this fits in to the hunt for safer explosives and propellants - this research by itself does not

outrightly determine whether any of the materials studied can be a safer choice of explosive or propellant, and will not instantly solve the issue of sensitivity overnight - but it is an iterative step on this road. This research shows that the study of complex multi-component explosive materials under pressure is possible, and future experiments can identify whether there are any links between the behaviour of these co-crystal materials and any sensitivity behaviour they may possess.

As the co-crystal experiments and RAM work are both novel fields and very novel studies, there is inevitable scope for future expansion. Given the complexities involved in solving complex organic structures from neutron powder diffraction data, and in observing such a fluid technique as RAM using a relatively slow analytical method as neutron diffraction, fruitful results in these endeavours will likely take longer than is possible in one doctoral project. But continued pursuit of these goals could yield new information on isotope effects in co-crystals, they could open up new insights into mechanochemical co-crystallisation, and they could ultimately help inform any future projects in crystal structure prediction.

Appendix A

Conferences and Courses Attended

Year 1

- Oxford Neutron School, Oxford, UK (September 2015)
- ISIS Neutron Source Student Meeting, Abingdon, UK (October 2015)
- New Trends in Research of Energetic Materials, Pardubice, Czech Republic (April 2016)
- ISIS Neutron Source User Meeting, Coventry, UK (July 2016)

Year 2

- European High Pressure Research Group, Bayreuth, Germany (September 2016)
- ISIS Deuteration Facility and DEUNET Meeting, Abingdon, Oxford (May 2017)
- ISIS Neutron Source User Meeting, Coventry, UK (July 2017)

Year 3

- 1-day teaching placement at Trinity Academy, Edinburgh, UK (June 2018)

Appendix B

Acknowledgements

The work published in this thesis was funded by an ISIS Facility Development Scholarship, jointly provided by the University of Edinburgh and the ISIS Neutron Source. Additional assistance has been received from The Falcon Project, the US Army, and the Weapons Science Technology Centre (WSTC) of the UK Ministry of Defence. Other experimental assistance has been acknowledged in the text of this thesis where appropriate.

Thus concludes the compulsory acknowledgements. Now for the rest.

So... where do we begin with this. After all, this is the one part of the thesis where I can actually be myself and theoretically ramble on about anything imaginable. We could use this space wisely and have a thorough discussion around how the air-conditioning grille on the British Rail Class 365 "Networker" Electric Multiple Unit makes it look like a very happy train. Seriously, go look it up, it's magnificent.

Alas, no. Much as I would like to take the line of P. Simon *et al* (1966) and claim that I am an island... no human is an island, and no thesis is a solitary rock. There are some people who very much deserve to be thanked, or at least have their existence acknowledged, because the preceding pages wouldn't exist if they weren't there. Unfortunately because I'm going to make a stubborn attempt to cover as many people as possible, this is going to sound one of those stupidly rambling and self-indulgent awards speeches you hear on television, so I'll apologise in advance. Pretend I'm wearing a tuxedo - it'll liven things up a little.

Let's get the work ones out of the way first. The research in this thesis would not have been completed without the supervision, guidance, support and assistance of Professor Colin Pulham, Dr Craig Bull and Professor Carole Morrison. All continually pushed me to produce the highest standard of research and analysis, and hopefully the content of this glorified paperweight reflects that to some extent. At the very least, I have now been thoroughly educated in the mission-critical need to hyphenate-all-sorts-of-possible-word-combinations and to capitalise every occurrence of 'x-ray' in existence (except this one, just to be annoying!). More seriously, I wouldn't even have started this thesis at all if Colin hadn't taken a daring chance on hiring a then-failing undergraduate to do an MSc back in 2014. I hope that gamble didn't turn out to be *entirely* useless for you.

I wouldn't be able to escape this thesis without mentioning the rest of the Pulham group and office 82 past

and present - Rowan, Hayleigh, Emily, Dan, Nisa, Akachai, Lisette, Fraser, Adam, Sumit, Stuart, Ellie, Fi and Rebecca. While at times we've probably very much annoyed each other, there have also been various points over the last four or five years where I have been vaguely glad of your company and... I was going to say "warmth", but I can't type that with a straight face. Either way, you know what I mean, you know what I'm trying to say, and you know I'd never write any kind of heartwarming sentiment anywhere you could actually see it. Thanks for helping keep me relatively sane... for the most part.

Special thanks have to go to the Inorganic teaching lab technicians, Jen, Craig and Donald; to Dr Murray Low and Dr Peter Kirsop; and to every one of the undergraduates that I've taught or supervised throughout my PhD. Although my ever-grumpy and sarcastic attitude may hide it, teaching and demonstrating has been the one part of my PhD that I've consistently enjoyed and that has kept me coming back into this place day after day when everything else was at its bleakest. I may have spent a lot of my teaching activities flying by the seat of my pants in terms of preparation and knowledge, but they've never been anything but fun, and I will miss teaching the most out of everything in this department.

Thanks also have to go to the various support staff in the department who've helped everything function smoothly in the background and helped me push through the various bureaucratic processes and barriers that any kind of job anywhere in the world manages to throw up, or helped fix various issues when they arose, or just generally been decent people to have a conversation with in the middle of a long day - Tim, Mark, Simon, Isobel, Davy, Paul, Moira, Jim, Carolyn, Sharon and Denise. I don't know how frequently you all get a shout-out in these sorts of documents, but it's probably not often enough.

Now I'm going to take the rest of this section to mention various people outside of work. After all, work has taken enough these past four years. So here are some people from other parts of life whose silent contribution has never ever had a mention, who all very much well deserve one, and who are unlikely to ever read this anyway. This document very much wouldn't be here without their presence. Go make a cup of tea or something, it'll be over soon.

Firstly, the St Andrews First Aid corps. In an ideal world I would thank all of the first-aiders and cadets under my command and even more beyond, but this is a thesis, not a roll call, and given that there would be close to a hundred people we'd seriously struggle for space. But I do have to give specific mentions to Cathy, Joe, Willie, Brenda, Jeannie, Dawn, Mike, Sofia, and my long-suffering deputy - Alister. You may not ever know it and I'm very good at hiding it, but you've all kept me going at this, at times when my confidence in myself was at its absolute lowest. You've taught me that I have many more skills and abilities with people and leadership than those needed to produce this thesis or that I ever get the chance to use in academia, and that I'm occasionally good at them when I need to be. Without the renewed self-confidence

that you've given me at various points, I would have abandoned this doctorate a long time ago. Don't vote me out of office just yet.

Next, Save the Children. While I would probably need a second volume to list all two-hundred and fifty-seven volunteers that I worked with over the course of the five years I managed one of their shops, I would like to single out Ian and Val for their friendship and wonderfully cynical outlook on reality. My experience managing in this shop shaped my mindset and people skills in more ways than any titles or post-nominal letters ever will.

Thirdly, I would like to acknowledge the existence of the band Genesis, known for many hits such as "Land of Confusion" and "I Can't Dance". There's no real reason for this - I just find the idea of Genesis getting a mention in an otherwise-serious academic document to be hilarious.

I'd also like to acknowledge two friends. My former flatmate Peter and my childhood friend Jamie. Both have reminded me at various points that there is a life outside of work, and that there is still humanity outside of the uncaring world of academia. Both have thankfully refused to allow me to disappear out of their lives when I've been at my most withdrawn. I'd also like to acknowledge *one* of my ex-girlfriends - the good one, who taught me that I'm not as robotic as I think, and that I'm occasionally capable of being positive in life. I'll let you fight amongst yourselves to decide which one of you that is.

On a more serious note, sincere thanks have to go to my GP Dr Alison Stewart, and to the Crossreach counselling service. I'm not going to mince words - many parts of the past four or five years from across life have taken my mental and physical health beyond red lines and into dangerous territory on several occasions. No human should have to experience that, no events or culture should foment such a state in someone, and I honestly wouldn't be typing this right now without either of these to rebuild me again. They have the technology.

I also wouldn't be allowed to escape this thesis without bringing the family into it - my parents Janice and Michael, my aunt Roberta, uncle Simon, and cousin Lauren. Being the first person in the family to go to university (never mind do a PhD) generates its own unique pressures and expectations. But for the most part they've managed to keep their 'eagerness' in check, and have all attempted at various points to keep me focused on reality and on finishing this thesis at the times when I most wanted to throw the world of academia in the bin and run away to eke out a living as the world's creepiest bartender or something.

I couldn't write any acknowledgements section without thanking my late grandmother. Although worsening dementia over the years meant she probably never knew it, she provided a human voice to talk to every weekend, she never judged, she kept me grounded in reality, and was continually optimistic and upbeat in

the moments when I was at my darkest. A happy voice like that at the end of the phone was something I very much needed to get through a lot of what you've been reading.

The last acknowledgement and final word in this thesis has to go to arguably the most important person of all in the making of this - my grandfather. Most of who I am as a person today was shaped by his personality, and you probably have his influence to thank for the amount of 'unparliamentary language' I had to remove from the first draft of this section. Although he didn't live to see the end result of this intensive journey through an undergraduate degree, a postgraduate masters, and now a doctorate; it's very likely that I would not have started any of it, all those years ago, if not for his unwavering support, and his uncompromising attitude toward the universe. As I now move on to do something else with my life, I'm still following his advice of 'illegitimi non carborundum'.

Carry on.